Vera C. Rubin Observatory
Systems Engineering

An Interim Report on the ComCam On-Sky Campaign

On behalf of Rubin Observatory Project

SITCOMTN-149

Latest Revision: 2025-01-14

DRAFT

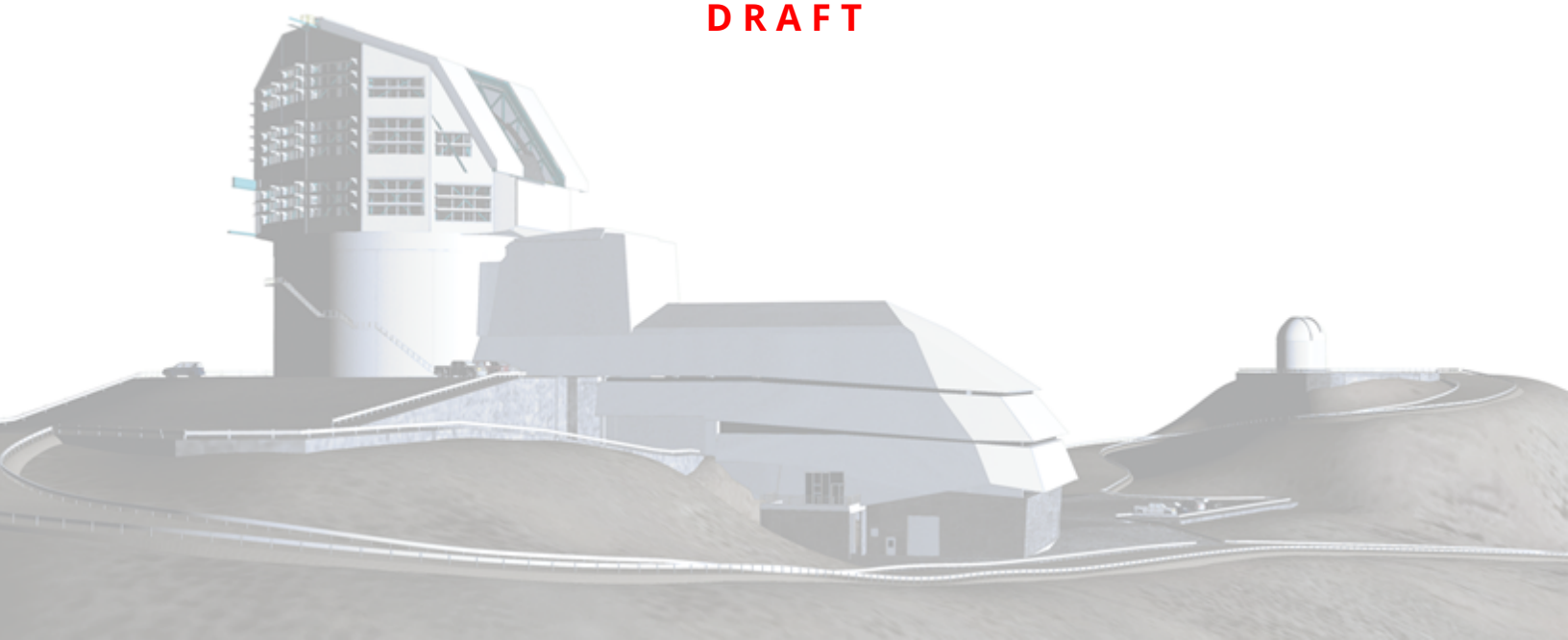

Abstract

From 24 October to 11 December 2024, the Vera C. Rubin Observatory conducted on an on-sky campaign using the engineering Commissioning Camera (ComCam) to test the end-to-end functionality of hardware and software, as well as operational procedures. This interim report provides a preliminary technical overview of our understanding of the integrated system performance based tests and analyses conducted during the ComCam on-sky campaign. The objectives are to synthesize what we have learned about the system in a timely way to inform on-going commissioning efforts, and to inform the Rubin science community on the progress of the ComCam on-sky campaign. The report is organized into sections to describe major activities during the campaign, as well as multiple aspects of the demonstrated system and science performance. All of the results presented here are to be understood as work in progress using engineering data and the initial versions of the data processing pipelines; the report is a living document that will be updated as analyses are refined.

Change Record

Version	Date	Description	Owner name
v0.0	2025-01-14	Initial release version.	Editors: Robert Lupton and Keith Bechtol

Document source location: `https://github.com/lsst-sitcom/sitcomtn-149`

Contents

An Interim Report on the ComCam On-Sky Campaign

1 Introduction

The Vera C. Rubin Observatory on-sky commissioning campaign using the Commissioning Camera (ComCam) began on 24 October 2024 and ended on 11 December 2024. This interim report provides a concise summary of our understanding of the integrated system performance based tests and analyses conducted during the ComCam on-sky campaign. The emphasis is distilling and communicating what we have learned about the system. The report is organized into sections to describe major activities during the campaign, as well as multiple aspects of the demonstrated system and science performance.

Warning: Preliminary Results

All of the results presented here are to be understood as work in progress using engineering data and the initial versions of the data processing pipelines. It is expected at this stage, in the middle of on-sky commissioning, that much of the discussion will concern open questions, issues, and anomalies that are actively being worked by the team. Additional documentation will be provided as our understanding of the demonstrated performance of the as-built system progresses.

1.1 Charge

Charge Development Historical Note

The initial version of the charge developed in November 2024 is provided below for reference.

We identify the following high-level goals for the interim report:

- **Rehearse workflows for collaboratively developing documentation** to describe our current understanding of the integrated system performance, e.g., to support the development of planned Construction Papers and release documentation to support the

Early Science Program [RTN-011]. This report represents an opportunity to collectively exercise the practical aspects of developing documentation in compliance with the policies and guidelines for information sharing during commissioning [SITCOMTN-076].

- **Synthesize the new knowledge** gained from the ComCam on-sky commissioning campaign to inform the optimization of activities between the conclusion of the ComCam campaign and the start of the on-sky campaign with the LSST Camera (LSSTCam).
- **Inform the Rubin Science Community** on the progress of the on-sky commissioning campaign using ComCam.

Other planned systems engineering activities will specifically address system-level verification ([LSE-29] and [LSE-30]) using tests and analysis from the ComCam campaign. While the analyses in this report will likely overlap with the generation of verification artifacts for systems engineering, and system-level requirement specifications will serve as key performance benchmarks for interpreting the progress to date, formal acceptance testing is not an explicit goal of this report.

The groups within the Rubin Observatory project working on each of the activities and performance analyses are charged with contributing to the relevant sections of the report. The anticipated level of detail for the sections ranges from a paragraph up to a page or two of text, depending on the current state of understanding, with **quantitative performance** expressed as summary statistics, tables, and/or figures. The objective for this document is to **summarize the state of knowledge of the system**, rather than how we got there or "lessons learned". The sections refer to additional supporting documentation, e.g., analysis notebooks, other technotes with further detail, as needed. Given the timelines for commissioning various aspects of the system, it is natural that some sections will have more detail than others.

The anticipated milestones for developing this interim report are as follows:

- 18 Nov 2024: Define charge
- 4 Dec 2024: First drafts of report sections made available for internal review
- 18 Dec 2024: Revised drafts of report sections made available for internal review; editing for consistency and coherency throughout the report

- 14 Jan 2025: Initial version of report is released
- Mid-March 2025: Updated version of report is released based on further iterations of data processing and analysis (planned)

Warning: On-sky Pixel Image Embargo

All pixel images and representations of pixel images of any size field of view, including individual visit images, coadd images, and difference images based on ComCam commissioning on-sky observations must be kept internal to the Rubin Observatory Project team, and in particular, cannot be included in this report. Embargoed pixel images can only be referenced as authenticated links; unfortunately this means that there will be some links which cannot be followed by readers who are not members of the Rubin commissioning team. See [SITCOMTN-076] for details.

2 Executive Summary

The Vera C. Rubin Observatory project team has completed a first series of on-sky engineering tests demonstrating the end-to-end functionality of the Simonyi Survey Telescope's hardware and software systems using an engineering test camera, the Commissioning Camera (ComCam).

Versioning Note

This interim report provides a preliminary technical overview of the ComCam on-sky campaign based on analyses through early January 2025.

2.1 Commissioning Camera (ComCam)

ComCam mass distribution, physical envelope, and interfaces designed to match LSSTCam. ComCam focal plane has single raft with 3 × 3 mosaic of (4K × 4K) ITL science sensors (144 Mpix total). For comparison, LSSTCam comprises 21 rafts with both ITL and e2v sensors (total of 189 science sensors; 3.2 Gpix) + 4 dedicated corner rafts for guiding and wavefront estimation. Because ComCam has no dedicated corner rafts, it was necessary to piston the entire ComCam focal plane in order to acquire intra- and extra-focal images of the pupil ("donuts") for AOS commissioning. Same plate scale as LSSTCam (0.2 arcsec / pixel). The field of view is 40 arcmin × 40 arcmin. ComCam filter exchanger holds 3 physical filters at a time.

2.2 Accomplishments

The primary goals of the campaign were to use ComCam to

1. learn how to more efficiently commission the LSST Camera (LSSTCam) on sky
2. optically align the telescope and verify capability to deliver acceptable image quality for the smaller ComCam field of view

The ComCam on-sky campaign accomplished the primary goals, and much more:

- **The telescope delivers crisp images.** The median delivered image quality during the campaign for commanded in-focus images, quantified in terms of the PSF FWHM, was ~ 1.1 arcseconds. The best images have delivered PSF FWHM ~ 0.65 arcseconds. Multiple analysis approaches suggest that Rubin Observatory is already capable of achieving a system contrbution to the delivered image quality of ~ 0.4 arcseconds (i.e., accounting for the atmosphere seeing contribution), even with several of the Observatory environmental controls not yet fully in place.
- **The team validated and further refined the AOS open loop system, and demonstrated the AOS closed loop system functionality with a variety of configurations and environmental conditions.**
  - Telescope focused and coarsely aligned at start of each night using laser tracker, then fine-tuned using wavefront sensing

  - Using almost all degrees of freedom
  - multiple wavefront estimation algorithms
  - tested range of stellar densities
  - AOS in LSST Wide-Fast-Deep survey emulation mode

- **Scheduler driving on-sky operations, including with the Feature Based Scheduler**
- **The system can efficiently acquire visits at a given target field.** The median time between successive visits for short translational dithers on the angular scale of the ComCam field of view was reduced to less than 3 seconds by the end of the campaign[1], enabling sustained rates of more than 90 individual 30-second visits per hour on a given target field, including occasional filter changes and rotational dithers.
- **ComCam instrument was reliable and effective.**
- **Telescope tracking and boresight stability have been superb.** Analysis of telescope mount encoder data finds a median contribution to the delivered image quality PSF FWHM from tracking jitter of less than 0.01 arcseconds.
- **System optical throughput consistent with a priori expectations.** Measured and predicted counts from per-visit synthetic photometry for the spectrophotometric standard star C26202 are consistent for all bands at the $\sim 5\%$ level. Comparison to reference catalogs (e.g., from the Dark Energy Survey) shows a tight locus with respect to stellar colors, enabling empirical validation of the color terms for the Rubin Observatory passbands.
- **Data transfer and downstream image analysis software working well.**
  - Quicklook campaign at summit supporting nighttime operations
  - Prompt processing and data release processing campaigns at USDF; running at USDF within a few minutes; Generating (but not publishing) alerts; Finding asteroids; Real-bogus classifier running in alert production pipeline; Minimal impact due to cosmic rays
- **The internal astrometric and photometric calibration are on track to meet design requirements.**
  - Stellar astrometric repeatability below 10 mas using only single-frame calibration (i.e., before running global astrometric solution with the gbdes algorithm)

[1] Because of the ComCam's small field, this intervisit time is consistent with the *c.* 7s expected for LSSTCam.

  - Photometric repeatability for bright stars at level consistent with the statistical Poisson noise photometric errors, with contribution from calibration errors at few mmag level

- **Collimated Beam Projector can co-point with telescope and acquire wavelength scans.**
- **Demonstrated stuttered imaging and guider mode imaging to evaluate high-frequency contributions to delivered image quality (1-100 Hz).**
- **Exercised end-to-end workflows for test planning, execution, and associated data processing and analysis during 7 weeks of continuous operations.**
  - Several hundred team members directly contributed to the ComCam on-sky campaign, supporting continuous 24-hour cycles of daytime and nighttime testing at the summit, observatory operations from the Base Facility in La Serena Chile, data processing campaigns at the US Data Facility at SLAC National Accelerator Laboratory, and data analysis from locations around the world. The successes of the ComCam on-sky campaign were made possible by years of preparatory work by the extended Rubin Observatory team.
  - More than 50 team members worked summit shifts for on-sky testing, and multiple new observing staff were onboarded during the campaign.
  - The ComCam on-sky campaign required parallel logistics support and coordination for ongoing summit engineering and LSSTCam reverification at the summit.
  - The team is incorporating lessons learned from the ComCam on-sky campaign towards preparations for LSSTCam on-sky commissioning.
  - Team is strong.

2.3 Areas of Investigation and Further Development

At this stage, while system integration and commissioning is ongoing, it is to be expected that the team would be actively investigating multiple issues.

- **Interpreting stray and scattered light in ComCam observations.** Approximately 20% of ComCam pointings showed structured patterns of stray light along an edge and/or corner of the ComCam field of view, that are likely attributed to scattered light from

bright stars located slightly outside the ComCam field of view. Dedicated observations of bright stars were acquired to test the hypothesis that the structured scattered light arises from something related to the ComCam filters, rather than scattering from M2 baffles or another element that will be in place for LSSTCam. There is currently no evidence for structured scattered light when the ComCam filters are removed, although we expect some features from *c.* 15-20 degrees off axis as the light/windscreen baffle is not yet installed.

  - There remains a risk of structured stray light contamination arising from the M2 baffle. The concern arises because the black coating on the M2 baffle is anodization rather than a more reflection-suppressing coating such as Aeroglaze. There are ongoing modeling efforts and on-sky test planning to better understand the system, and potential stray light paths for LSSTCam.

- **Evaluating contributions to delivered image quality.** Multiple approaches are being pursued to evaluate the various contributions to the delivered image quality during the ComCam on-sky campaign, including the camera, static optics, dynamic optics, mount motion, observatory seeing, and the atmosphere. Observatory environmental controls and monitoring equipment were not yet fully in place during the ComCam campaign.
  - Analysis of discrepancies between the estimated AOS residual based on wavefront sensing and measurements of the free atmospheric (*e.g.* DIMMs), and delivered image quality
  - Analysis of "stuttered"[2] and guider mode imaging. Preliminary analysis of the stuttered and guider mode imaging data shows strongly correlated common mode motion between stars across the ComCam field of view, suggesting that the delivered image quality during those observations was dominated by dome and/or mirror seeing contributions, or telescope motion.
  - AOS closed loop convergence optimization
  - M1M3 thermal contribution and control
  - Rubin Obs DIMM operations
  - Dome seeing monitor equipment installation and commissioning
  - Dome louvers + light and wind screen installation and commissioning
- **Commissioning calibration hardware.**

[2] data taken while using the CCD's parallel gates to generate a series of images of a star.

  - Initial commissioning of the Collimated Beam Projector (CBP) using the Simonyi Telescope and ComCam took place during the final weeks of the campaing. Analysis of CBP data from ComCam is ongoing. Initial analyses shows excesss transmission of red light in the ComCam g filter beyond 1100 nm, although the impact is not yet clear as the ComCam CCDs run *c.* 20C warmer than LSSTCam's.
  - Flat field screen and illumination system installation and commissioning is ongoing as of January 2025.

- **Increasing overall system reliability and efficiency.** Overall system reliability and efficiency, expressed, for example, in terms of the effective open shutter time fraction, increased throughout the ComCam on-sky campaign. This is an ongoing effort that will continue throughout on-sky commissioning with LSSTCam, and will be continuously monitored and optimized during LSST operations.

- **Improving camera hexapod rotator performance.** The camera hexapod rotator motion performance was sufficient for ComCam on-sky commissioning. The larger LSSTCam field of view requires more stringent performance over the range of telescope altitude and azimuth angles expected for LSST operations.

- **Increasing Simonyi telescope motion performance.** The telescope commanded velocity, acceleration, and jerk motion settings were increased during the ComCam on-sky campaign. The telescope is fixed at a horizon pointing orientation during the removal of ComCam and installation of LSSTCam. The ongoing effort to characterize and control inertial forces experienced by the optics with progressively increasing telescope motion settings will resume during the on-sky commissioning campaign with LSSTCam.

3 Observations

Roughly 16K total exposures were acquired during the ComCam on-sky campaign from 24 October 2024 to 11 December 2024. Tab. 1 summarizes the distribution of visits, disaggregated by `img_type`. The visits include more than 10K exposures for active optics system (AOS) commissiong (roughly one-third each of intra-focal, extra-focal, and in-focus images), more than 2K bias and dark calibration frames, and more than 2K visits for Science Pipelines commissioning.

img_type	Number of Visits	Notes
ACQ	5261	Includes in-focus visits for AOS commissioning
BIAS	1432	Bias frames for calibration
CWFS	5169	Curvature wavefront sensing for AOS commissioning
DARK	1153	Dark frames for calibration
ENGTEST	169	Includes CBP commissioning
FLAT	37	
FOCUS	534	Focus sequences
OBJECT	2144	Mostly visits for Science Pipelines commissioning
STUTTERED	61	Stuttered imaging

Table 1: Distribution of visits by image type (`img_type`) during the ComCam on-sky campaign.

3.1 Observations for Science Pipelines Commissioning

To maximize the utility of observations for Science Pipelines commissioning, the team acquired repeated observations distributed across multiple bands for a small set of fields across many nights to

- test the internal astrometric and photometric calibration across a range of observing conditions and assemble large statistics,
- provide routine opportunities for testing difference image analysis and Prompt Processing framework, and
- accumulate upwards of 200 visits per band to evaluate deep coadds at roughly LSST WFD 10-year equivalent integrated exposure.

Tab. 2 reports central pointing coordinates for seven target fields used for Science Pipelines commissioning during the ComCam on-sky campaign. The fields were selected to collectively span a range of stellar densities, overlap external reference datasets to enable a broad range of science verification and validation studies, and span the breadth of the four primary LSST science themes.

The ComCam filter exchanger holds three filters at a time. A typical observing epoch on a given target field consisted of 5-20 visits in each of the three loaded filters. Nearly all of the visits for Science Pipelines commissioning used a single 30-second exposure, rather than 2 × 15-second "snap" exposures.

Target	RA	Declination
	deg	*deg*
47 Tuc Globular Cluster (47 Tuc)	6.02	-72.08
Low Ecliptic Latitude Field (Rubin SV 38 7)	37.86	6.98
Fornax Dwarf Spheroidal Galaxy (Fornax dSph)	40.00	-34.45
Extended Chandra Deep Field South (ECDFS)	53.13	-28.10
Euclid Deep Field South (EDFS)	59.10	-48.73
Low Galactic Latitude Field (Rubin SV 95 -25)	95.00	-25.00
Seagull Nebula (Seagull)	106.23	-10.51

Table 2: Pointing centers for seven target fields observed for Science Pipelines commissioning during the ComCam on-sky campaign. ICRS coordinates are shared in units of decimal degrees.

Fig. 1 and Fig. 2 show the coverage of the seven target fields. Six of the fields used a pattern of random translational and rotational dithers within an 0.2 deg radius circle around the pointing center. The rotational dithers were typically applied at the time of filter changes for operational efficiency, with small rotatoral dithers (~ 1 deg) applied between individual visits.

For the low ecliptic latitude field, the team used an alternative dither pattern to maximize the coverage of Solar System Objects and to facilitate testing Solar System Object linking across multiple nights. The observations synthesized a 2×2 grid of ComCam pointings to cover a region roughly 1.3 deg $\times$ 1.3 deg (Fig. 2). The visits cycled between the four pointing centers in the grid, using small psuedo-random translational dithers to fill in chip gaps, with the goal of acquiring 3-4 visits at each pointing center in each band during in each observing epoch.

Tab. 3 provides a summary of the band coverage across the seven fields. Fig. 3 shows the resulting integrated depth, expressed in terms of the flux of an unresolved source that would be measured with signal-to-noise ratio $S/N = 5$, using the *r* band as an example.

Fig. 4 shows the distribution of science program observations by night (`day_obs`) during the ComCam on-sky campaign. There was a general trend towards increasing efficiency and time allocated for science program observations as the campaign progressed. Fig. 5 shows observations for the ECDFS field, which received the densest and most consistent temporal sampling of the seven target fields during the campaign.

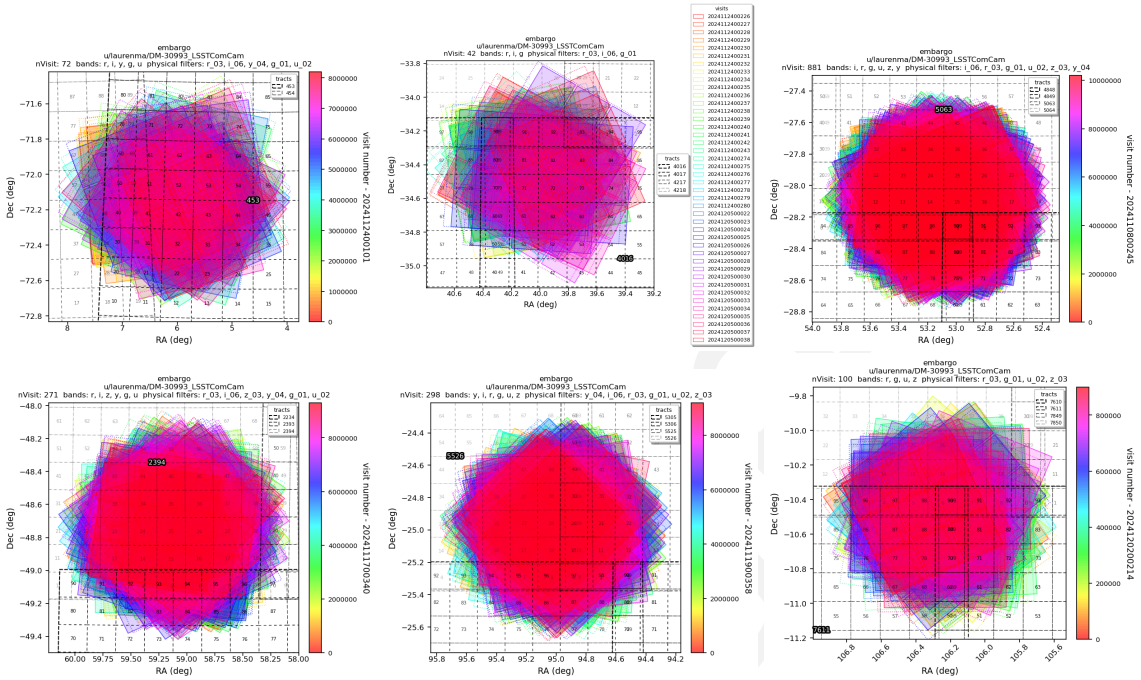

Figure 1: Sky coverage for six ComCam Deep Drilling Fields. First Row (left to right): 47 Tuc, Fornax dSph, ECDFS. Second Row (left to right): EDFS, RubinSV 95 -25, Seagull.

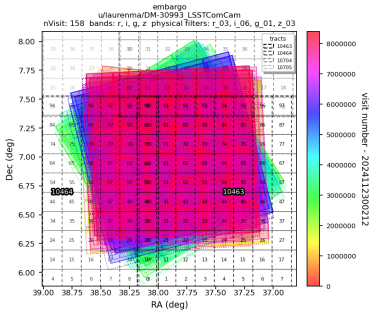

Figure 2: Sky coverage for Low Ecliptic Latitude Field (Rubin SV 38 7) during the ComCam on-sky campaign.

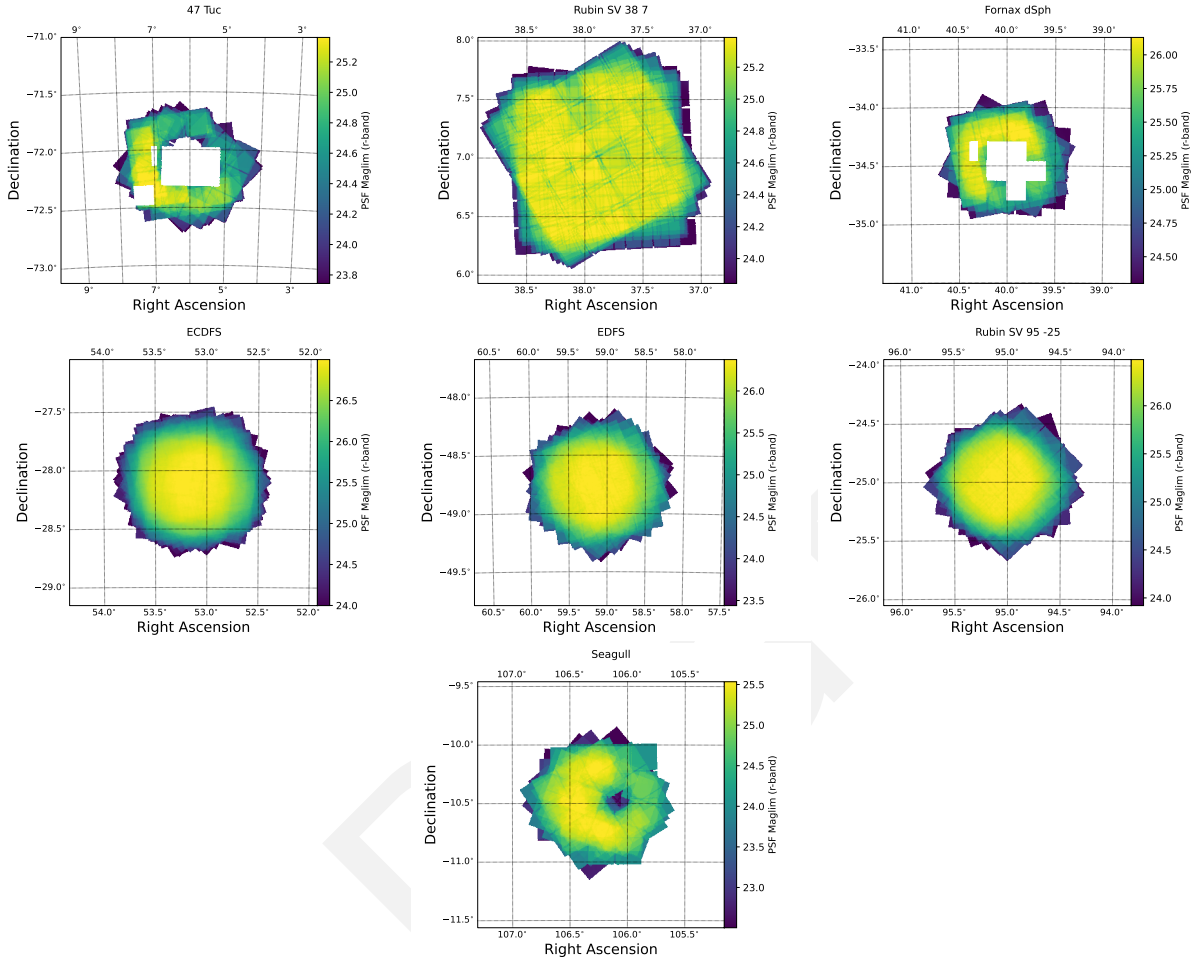

Figure 3: Cumulative imaging depth expressed in terms of the $S/N = 5$ limiting magnitude for unresolved sources for seven ComCam Deep Drilling Fields. First Row (left to right): 47 Tuc, Rubin SV 38 7, Fornax dSph. Second Row (left to right): ECDFS, EDFS, RubinSV 95 -25. Third Row: Seagull.

Target	**u**	**g**	**r**	**i**	**z**	**y**
47 Tuc	6	10	33	19	0	5
Rubin SV 38 7	0	44	55	57	27	0
Fornax dSph	0	5	26	13	0	0
ECDFS	53	230	257	177	177	30
EDFS ComCam	20	61	90	42	42	20
Rubin SV 95 -25	33	86	97	29	60	11
Seagull	10	37	49	3	13	0

Table 3: Band coverage for seven target fields observed for Science Pipelines commissioning during the ComCam on-sky campaign.

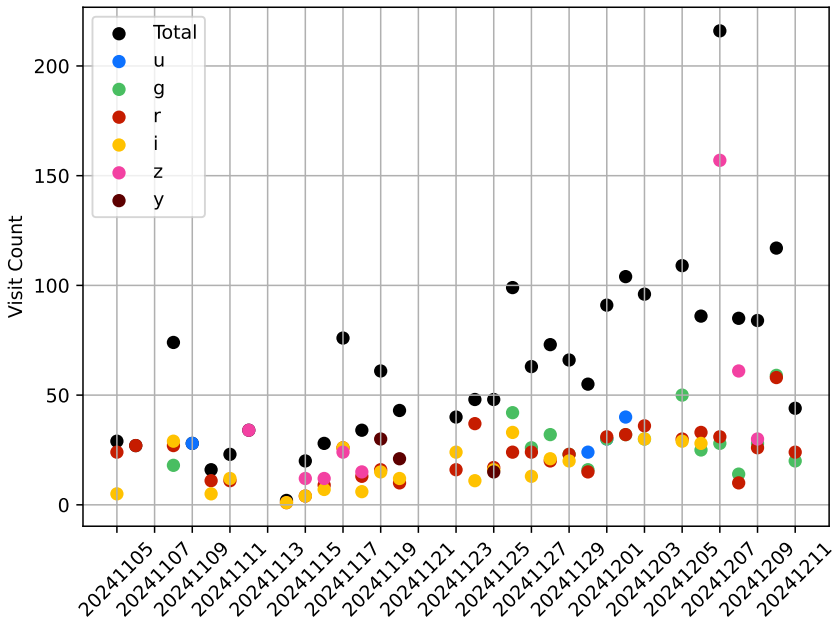

Figure 4: Distribution of Science Pipelines commissioning observations by day_obs during the ComCam on-sky campaign.

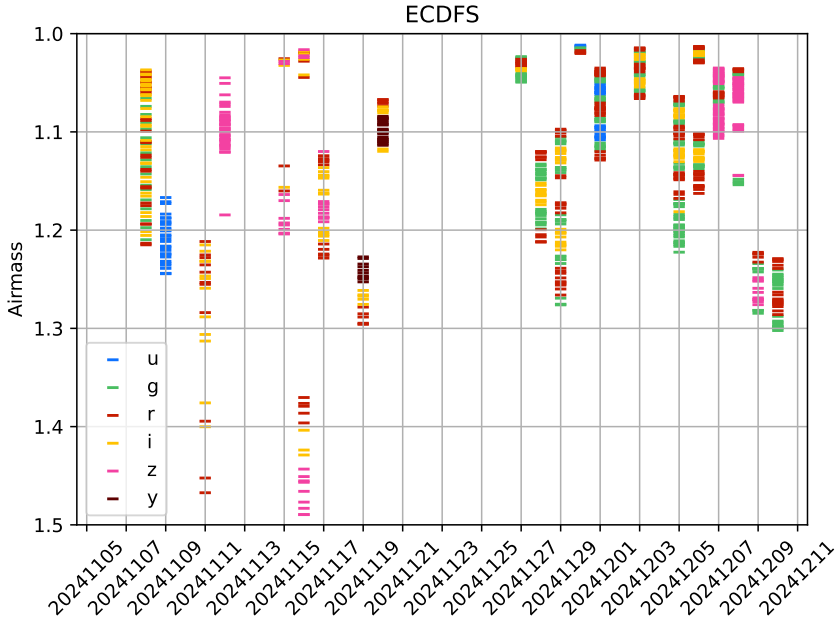

Figure 5: Distribution of Science Pipelines commissioning observations for the ECDFS field during the ComCam on-sky campaign.

4 System Performance Analysis

- M1M3 and M2 glass installed on the Simonyi Survey Telescope.
- Since then, we have been operating the telescope with limited velocity, acceleration, and jerk limits following the performances defined in TMA Motion Settings.
- For each configuration, defined in terms of a percentage of the maximum velocity, acceleration, and jerk, we ran multiple gateway tests.
- The gateway tests are described in the Sec. 4.1 below.

4.1 Gateway Tests

We started the ComCam on Sky test campaign using Simonyi Telescope with limited performance, described as a percentage of the maximum velocity, acceleration, and jerk limits. The performance is defined in TMA Motion Settings Confluence page.

Before we can increase the telescope performance, we need to perform a set of tests that ensure that the system will respond safely to the new velocity, acceleration, and jerk. These tests are called gateway tests. Here is the list of all the tests.

- BLOCK-T227 Dynamic Tests at El = 34º short and long slews
- BLOCK-T294 Dynamic Tests at El = 70º short and long slews
- BLOCK-T231 TMA Azimuth Brake Test
- BLOCK-T240 TMA Elevation Brake Distance
- BLOCK-T241 M2 closed-loop break-out brake test during TMA slew

4.1.1 Long and short slews at different elevations

These tests ensure that the force balance systems on M1M3 and on M2 can protect the mirrors on different telescope positions and while slewing. As we increase velocity, acceleration, and jerk limits, both mirrors suffer higher inertial forces and the force actuators must counteract them.

The last set of data was collected on 2024-11-28. Fig. 6 shows the slews performed when collecting this data starting at higher elevations (70°) and then moving to lower elevations (34°).

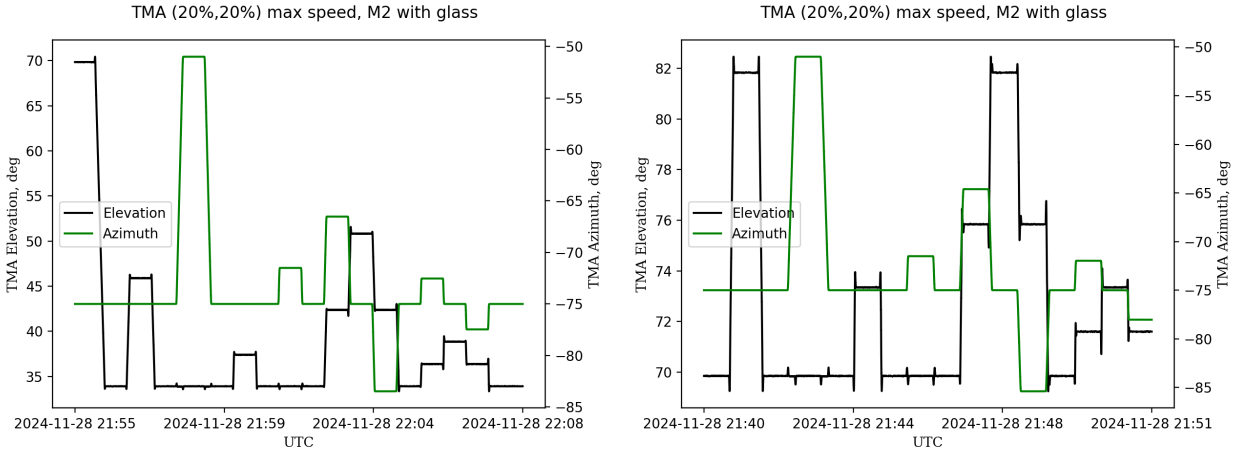

Figure 6: TMA Short and Long slews at El = 34° (left) and El = 70° (right).

For each of these slews, the force balance system on M1M3 should keep the forces measured on the hardpoints below an operational limit (15% of the breakaway limit, nominally 450 N). Figs. 7 and 8 show histograms with the number of slews that hit certain minima and maxima values for the hardpoint forces. The left histogram shows the minima reached on each slew. The right histogram shows the maxima reached on each slew. The red dashed lines show the fatigue limit (30% of the breakaway limit, nominally 900 N).

You can see a few slews with min/max reaching 800 N at low elevations. This is quite close to fatigue limits (900 N). However, these slews were performed without booster valves enabled. In addition, the big majority of the slews have measured forces below the operational limit. This gave us confidence that, from M1M3's perpective, we can use the 20% velocity, acceleration, and jerk for the rest of the campaign. Note that we ran a few test slews with booster valves enabled and loads were significantly reduced (<200N per HP) before we got faults in some of the actuators with bad valves (need data analysis).

Similarly, M2 has limits of the measured forces associated with its closed loop and its open loop. Figs. 9, 10, and 11 show the axial forces, the tangent forces, and the tangent force errors

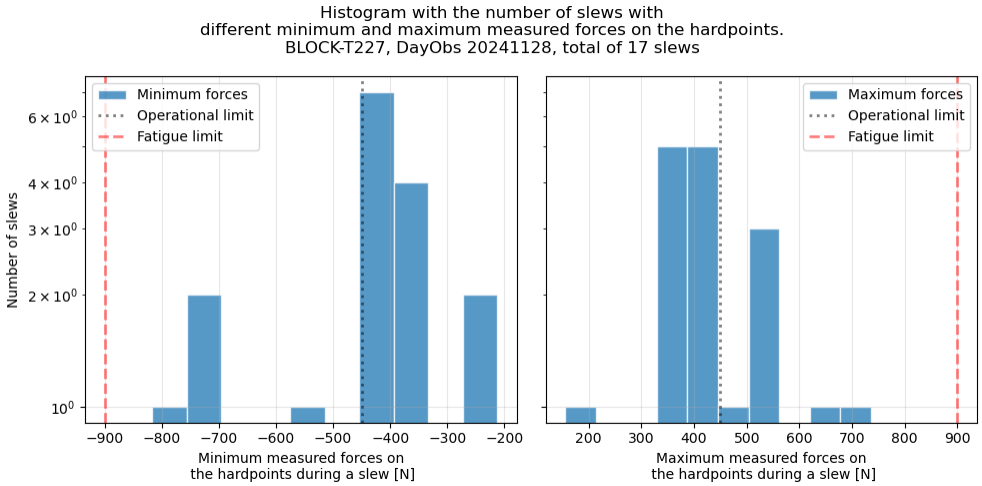

Figure 7: M1M3 hardpoint histograms min/max HP forces at low elevation.

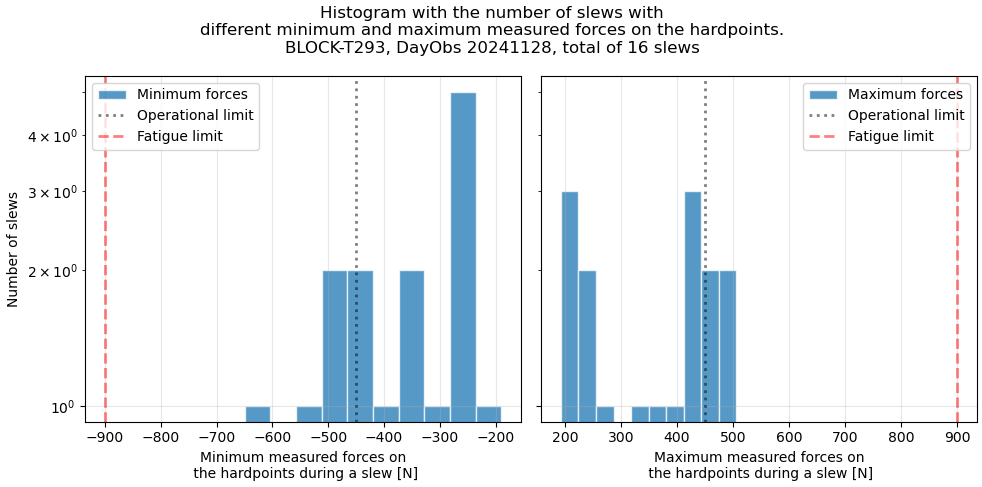

Figure 8: M1M3 hardpoint histograms min/max HP forces at high elevation.

for the slews performed at different elevations. We can see that, for every slew, all the forces are within the closed loop maximum forces limit. This means that, from M2's perpective, we are safe to operate the telescope with 20% velocity, acceleration, and jerk.

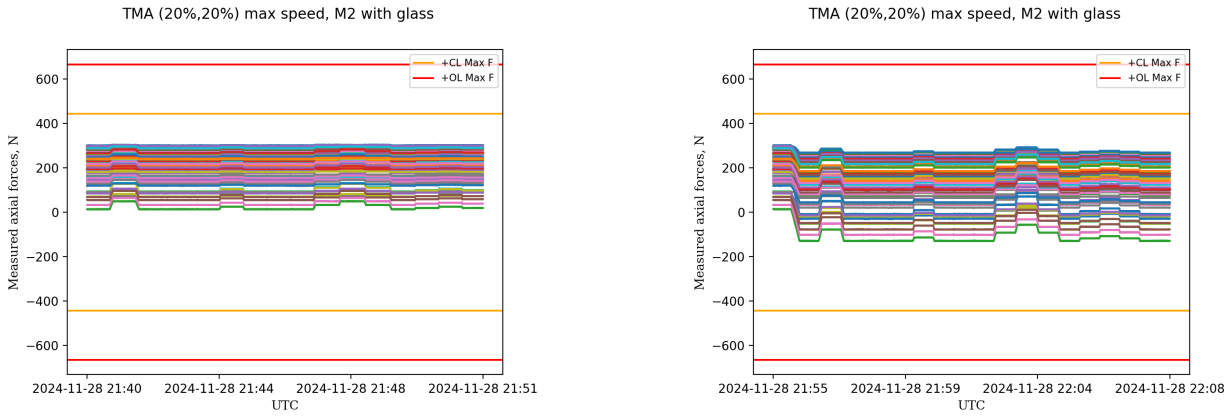

(a) M2 axial measured forces at low elevation.

(b) M2 axial measured forces at high elevation.

Figure 9: M2 axial measured forces during the slews at different elevations.

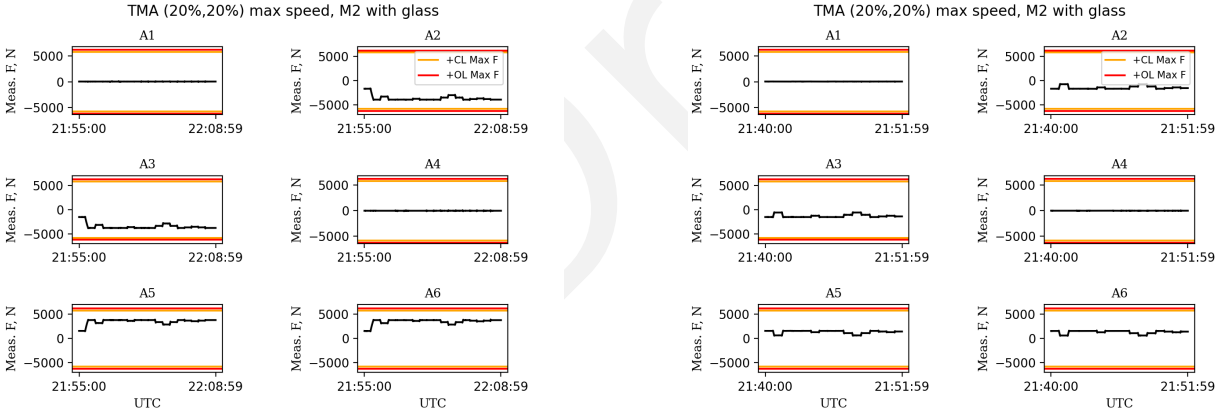

(a) M2 tangent force errors at low elevation.

(b) M2 tangent force errors at high elevation.

Figure 10: M2 measured tangent forces during the slews at different elevations.

4.1.2 M2 close-loop breakout tests

BLOCK-T241 M2 closed-loop break-out brake test during TMA slew is a test that ensures that M2 can survive an event where the telescope is slewing and, for whatever reason, the closed-loop system is disabled. In this case, the telescope will go to a fault and stop.

Figs. 12, 13, and 14 show the axial forces, the tangential forces, and the tangential force errors during an event where the closed-loop system is disabled. The plots show that both axial and

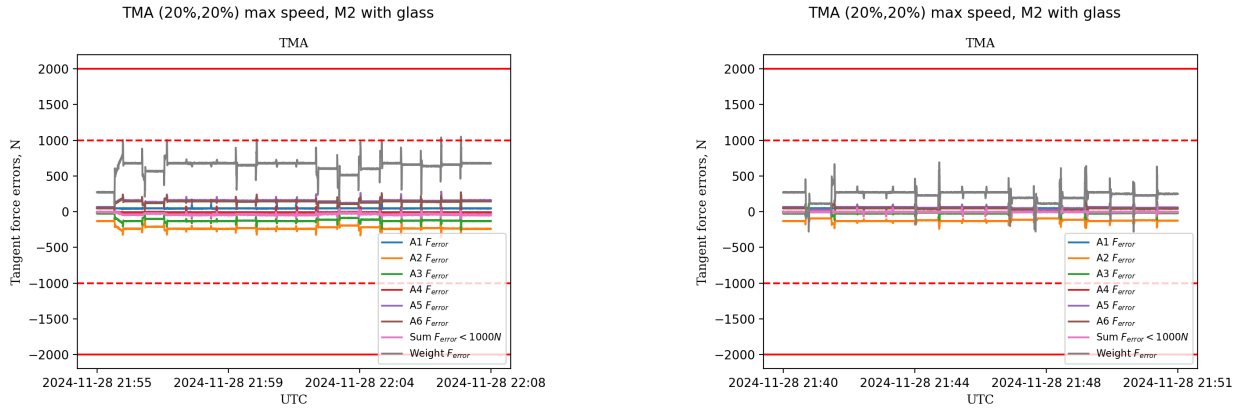

(a) M2 tangent force errors at low elevation.

(b) M2 tangent force errors at high elevation.

Figure 11: M2 tangent force errors during the slews at different elevations.

tangential forces are within the limits. Considering this tests, we can say that M2 is safe to operate with 20% velocity, acceleration, and jerk.

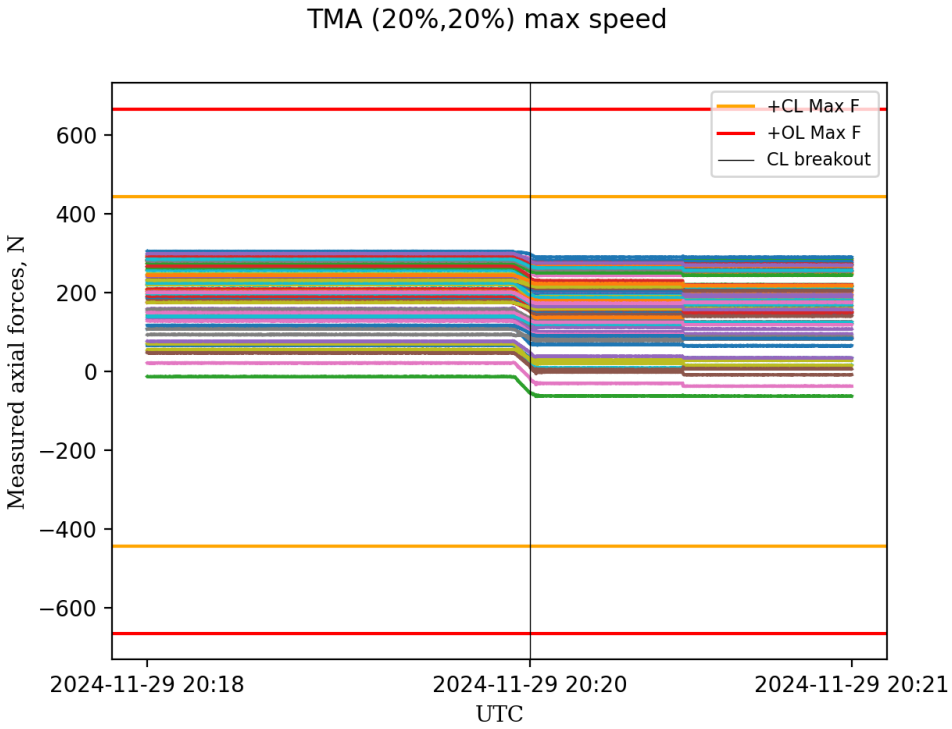

Figure 12: M2 axial measured forces during the closed-loop break-out test.

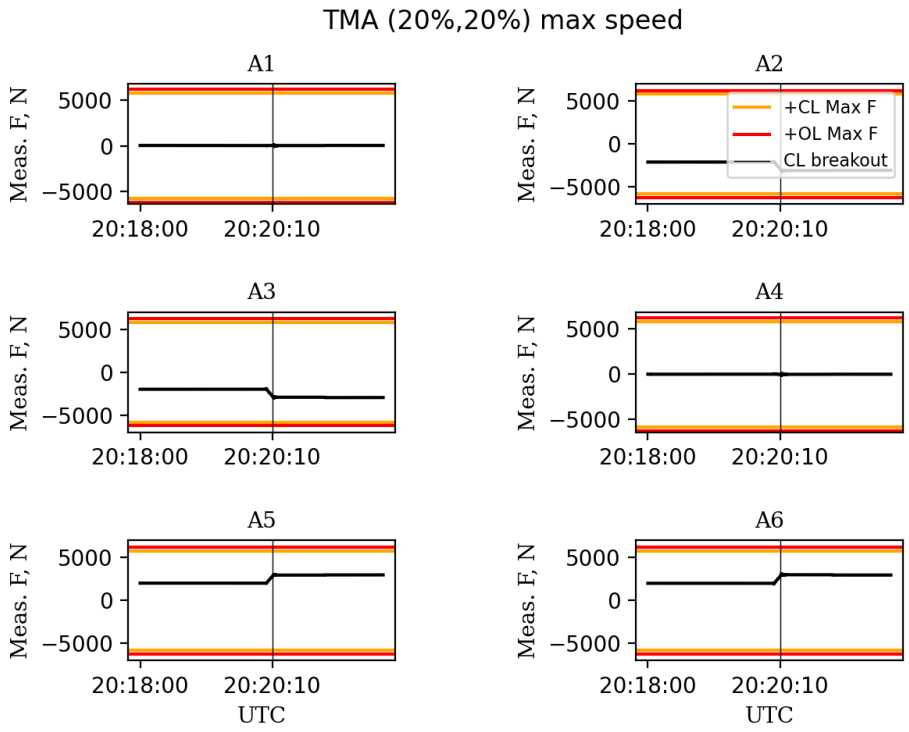

Figure 13: M2 tangential measured forces during the closed-loop break-out test.

4.1.3 TMA azimuth and elevation brake tests

The tests BLOCK-T231 TMA Azimuth Brake Test and BLOCK-T240 TMA Elevation Brake Distance are designed to ensure that the telescope will stop in case of an emergency. Accordingly to Fig. 15 the telescope travels 1.6 degrees in El (2.2 deg/s^2 peak deceleration) after the hard stop initiated. In Az, it travels 1.9 degrees (3.9 deg/s^2 peak deceleration) after hard stop initiated. Both without any mirror faults. These values seem reasonably low and confirm that the telescope would be safe in case of an emergency.

5 Active Optics System and Image Quality

5.1 Active Optics System Commissioning

AOS commissioning started on 2024-10-24 with the first ComCam images delivering a remarkable 1.7 arcsecond full-width half-maximum (FWHM) image quality. At the end of the

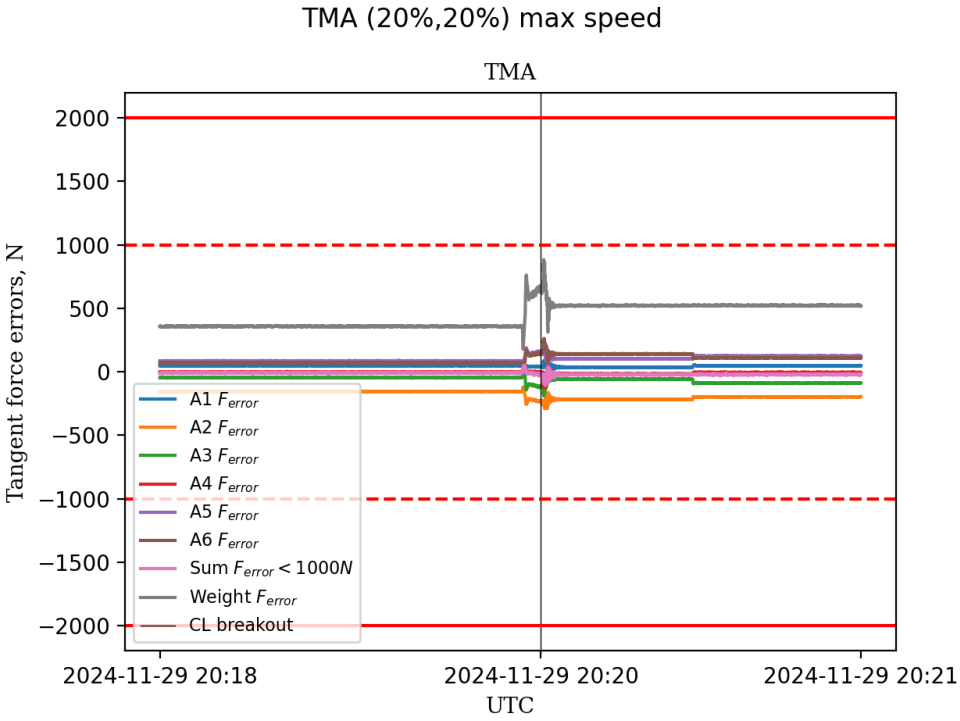

Figure 14: M2 tangential force errors during the closed-loop break-out test.

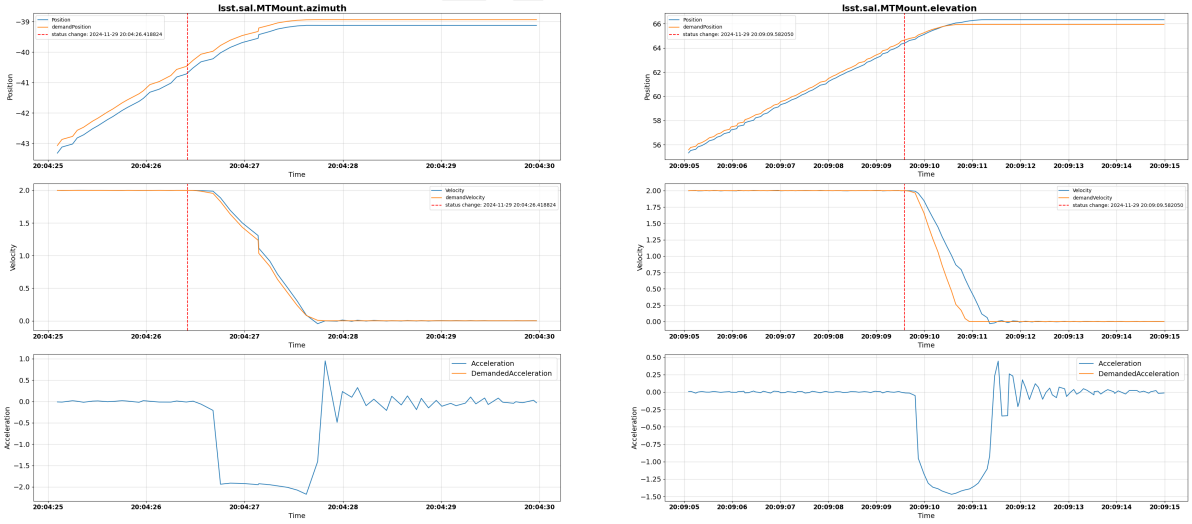

Figure 15: TMA Brake Test in Azimuth (left) and Elevation (right).

campaign we had shown that we could align the telescope optics, determine and correct for optical aberrations using the hexapods and bending modes for M2 and M1M3, and apply these corrections as a closed loop system. For some of the observations we met the image quality requirements of the LSST system (*i.e.* with the optical system delivering less than 0.4 arcseconds to the image quality budget) but there are still significant challenges in delivering seeing limited images consistently in all observing conditions.

Sub-arcsecond image quality was first achieved on the night of 2024-11-06, with a best image quality of 0.66 arcsecond FWHM (with a 0.1 arcsecond variation across the field achieved) on the night of 2024-11-12 in z. The AOS system was able to achieve closed-loop corrections using wavefront estimation across varying elevations and stellar densities. Closed-loop operations have been run autonomously by the observing specialists to show that the scripts and procedures are mature. Preparations are underway to prototype a fully autonomous survey-mode triplet-taking block before the conclusion of ComCam's on-sky operations.

While we have demonstrated that Rubin can achieve the optical performance requirements for the AOS system there are significant challenges in meeting the optical performance requirements consistently as a function of temperature and elevation. It is not currently clear which aspects of the optical system are limiting its performance but the AOS team is working to understand the source of high levels of defocus and some amount of astigmatism that are present in the Zernike measurements. The team is also working to improve the computational efficiency of the system, which currently takes 5 minutes to complete a closed-loop iteration.

The AOS algorithms appear robust for a range of source densities and image qualities. A number of failure modes of the AOS software are present and being investigated. These include failures in processing images through Rapid Analysis when donuts cannot be detected on all sensors, and difficulty in measuring the wavefront when the images are significantly defocused (e.g., when the intra or extra focal images appear in focus). The AOS team is working to improve the robustness of the system to monitor these and other failure modes.

Fig. 16 shows the FWHM delivered by the optical system (black line) as we correct the alignment and bending modes of the mirrors and camera over the nights 2024-11-25 to 2024-12-01. The FWHM is estimated from the Zernike amplitudes measured from out-of-focus donuts. The grey and blue lines are the 500nm and zenith corrected image qualities measured by the SOAR `RINGSS` seeing monitor and from the Rubin images respectively. The dashed green line

is the 0.25 arcseconds image quality requirement for the telescope optics. From these measurements the AOS system is shown to be capable of meeting the image quality requirements.

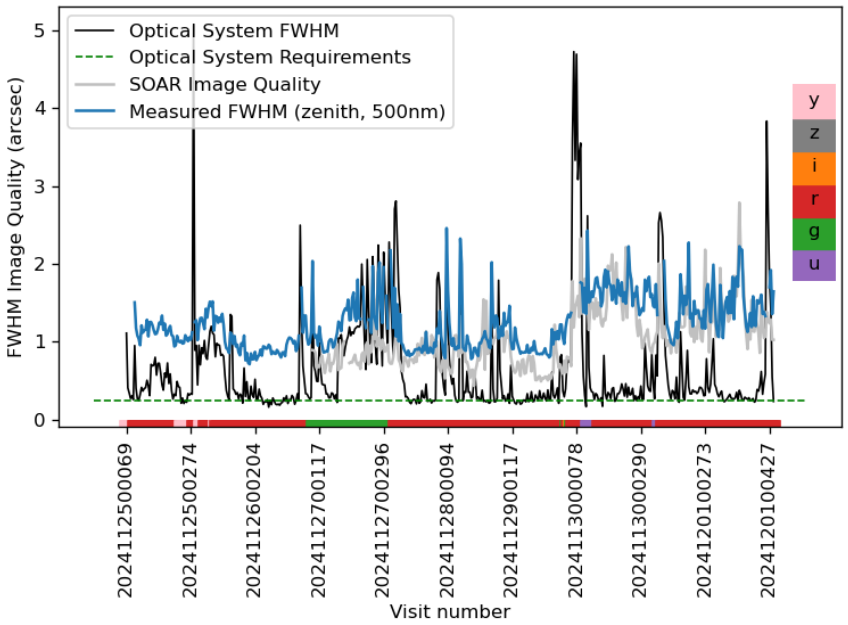

Figure 16: The FWHM delivered by Rubin (blue), the image quality from Rubin's optical system estimated from the AOS (black), and the image quality measured by SOAR (gray). The Rubin and SOAR measured FWHMs are corrected to 500nm and zenith.

5.1.1 Initial Alignment

Initial alignment of the AOS utilizes an updated laser tracker nominal frame based on a Final Element Analysis Model to ensure that the system is brought into focus prior to the start of observations. Combined with a measurement of the impact of gravity on the telescope, these refinements simplified the alignment process, demonstrating the value of accurate laser tracker data. Once we were able to get on-sky images using curvature wavefront sensing, we finalized the initial state of the hexapods position to ensure a well aligned system at the start of each night. Work is ongoing to understand the stability of the initial hexapod and bending mode positions across nights to determine how well we can predict the configuration of the AOS system at the start of each night.

5.1.2 Wavefront estimation

The wavefront estimator proved robust across diverse observing conditions of seeing, mount elevation and a few filters (r,i and y band) On dense fields such as 47 Tuc or NGC 253, the estimator provided accurate results for all sensors except the central one. Comparison of observed PSFs with simulations confirmed the accuracy of Rubin's ray-tracing software, `Batoid`.

Wavefront estimation and closed-loop convergence has been demonstrated using `TIE` and `Danish`. Other advancements include the implementation of sparse Zernikes, allowing selective inclusion of Zernike polynomial terms while minimizing cross-contamination of modes with identical azimuthal dependencies.

Despite delivering good optical quality, Zernike measurements indicate persistently high levels of defocus and some amount of astigmatism. We are continuing to investigate the source and impact of these measurements.

5.1.3 Closed Loop

Following resolution of initial issues with the AOS pipelines, closed-loop operations were achieved across varying elevations and filters (u, g, r, i, z, and y). Most optical modes were utilized, excluding the three highest-order modes on M2. Consistency in results across nights confirmed the need for further refinement of the LUT. In favorable seeing conditions, the system achieved sub-arcsecond image quality, with FWHM as low as 0.65 arcseconds.

The closed loop process still takes 5min often requiring 5 or more iterations. The best performance for the closed loop achieved convergence in two iterations but delivering this consistently has not been achieved and tuning the closed-loop gain and making further adjustments to improve computational efficiency remains a priority for the team.

5.1.4 LUT

The LUT underwent initial validation across elevations, azimuths, and rotator angles, leading to incremental improvements. While these updates enhanced performance, further refinements are needed to address second-order dependencies. Insights from ComCam data will inform these efforts, ensuring readiness for LSSTCam, which may present distinct challenges

due to its larger focal plane and optical system.

5.1.4.1 Next Steps

- Conduct step-by-step closed-loop validations for LSSTCam, validating signs and rotations for intentional perturbations.
- Collaborate with the Camera Team to anticipate and mitigate known camera tilts.
- Implement and validate tests tailored to LSSTCam's larger focal plane dimensions.
- Prepare RubinTV and donutViz for full-array LSSTCam mode and automate its execution for all triplet-taking sequences.
- Adapt MTAOS to run as a continuous background task, supporting survey-mode operations.
- Optimize the AOS pipeline for speed, including binning and ISR performance improvements.

5.2 Image Quality

The AOS team has delivered very impressive image quality, showing images with 0.68 arcsec FWHM. If we assume that sources of image degradation add in quadrature and we trust our estimates of atmospheric seeing, this is consistent with reaching the image quality error budget allocation of our full system of 0.400 arcsec.

The best image quality achieved so far is *c.* 0.65 arcsec, with a median of 1.1 arcsec during science visits; Tab. 4, Fig. 17, and Fig. 18.

We are in the process of quantifying the different sources of image degradation. The main ones we're focused on measuring are degradation due to the camera/instrument, static optics, dynamic optics, mount motion, and observatory seeing.

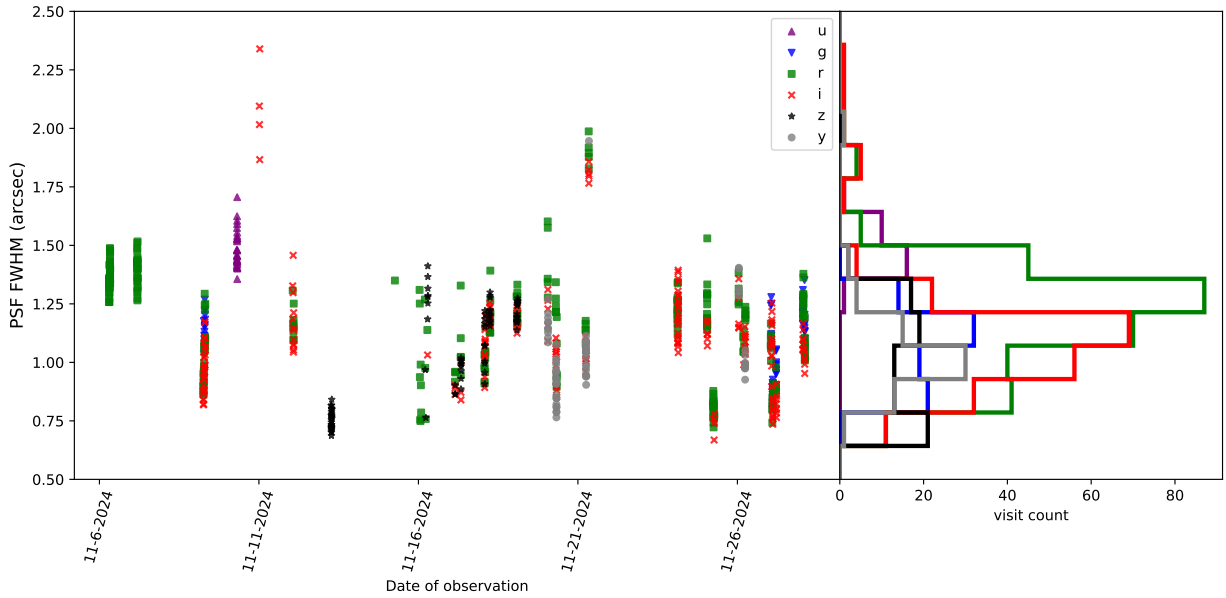

Figure 17: PSF FWHM as a function of the observed date. Data are from DRP from 2024-11-01 to 2024-11-28.

Band	**Number of Visits**	**Mean PSF FWHM**	**STD. DEV. PSF FWHM**
		arcsec	*arcsec*
All	775	1.12	0.23
u	28	1.49	0.08
g	86	1.07	0.14
r	307	1.18	0.22
i	203	1.09	0.24
z	85	1.01	0.21
y	66	1.04	0.18

Table 4: Summary of PSF FWHM performance. Data are from DRP from 2024-11-01 to 2024-11-28.

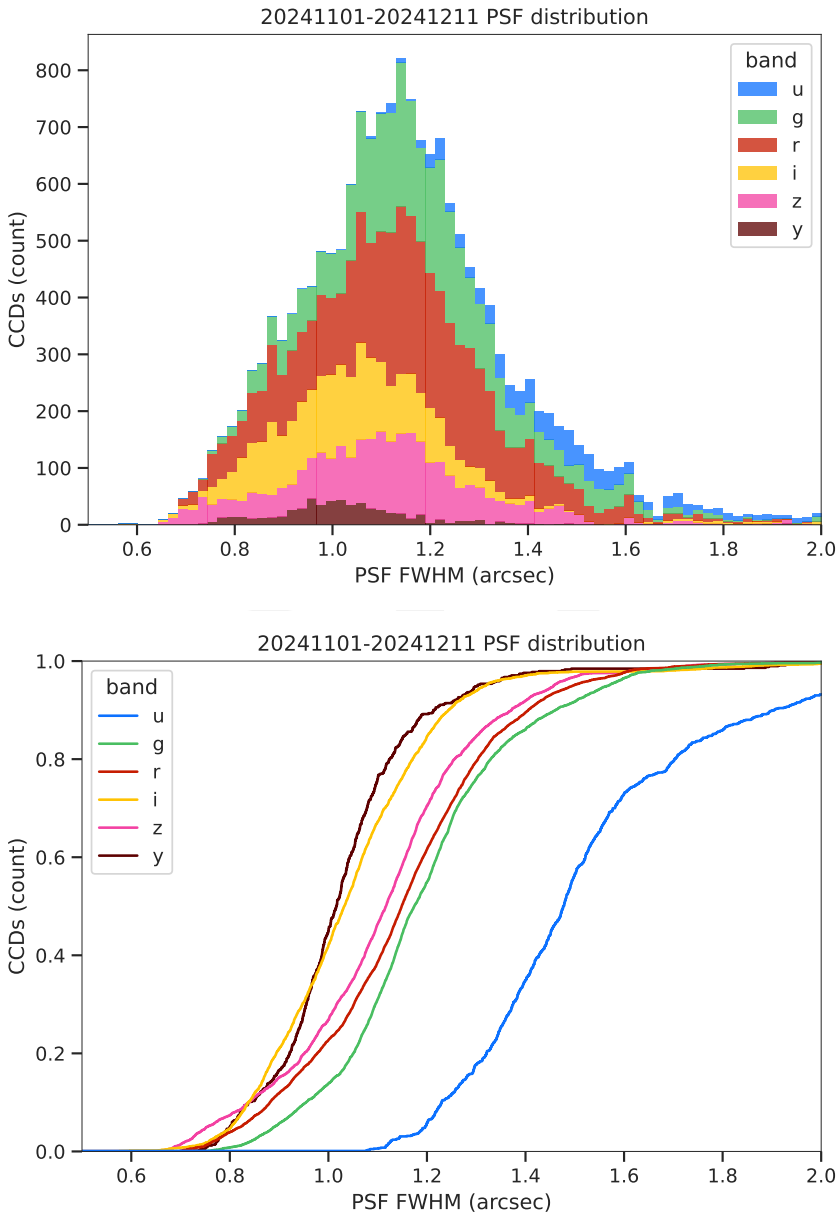

Figure 18: Distribution of PSF FWHM represented as a histogram (top) and cumulative distribution (bottom). Data are from DRP from 2024-11-01 to 2024-12-11.

5.2.1 Atmospheric Seeing

We do not currently have a working Rubin DIMM, although repairs are in progress. In the meantime, we have a livestream of data from the SOAR RINGSS.[3] We are working on getting direct access to current and historical data for RINGSS as well as the Gemini DIMM.

5.2.2 Static Optics

See Sec. 5.1 for more details on the performance of the static optics system.

5.2.3 Dynamic Optics

Dynamic optics contributions are caused by oscillations or motion of the mirrors, causing the quality of the optical alignment to change during an exposure. We have accelerometers in the mirror cell and on the top end but have not yet analyzed the data.

5.2.4 Observatory Seeing

The two main contributors to observatory seeing are dome seeing and mirror seeing. We do not have a direct dome seeing monitor but we do have a 3D sonic anemometer located in the dome that is taking data. We have looked at the correlation between the standard deviation of the sonic temperature, which should be a proxy for dome seeing due to thermal turbulence, and measured PSF FWHM in the science images (see Fig. 19). There is no obvious correlation, so we need more and better data, and to remove atmospheric seeing contributions, before these measurements are able to help analyze the delivered image quality.

5.2.5 Mount Motion

There are two main components to image degradation due to mount motion. The first component comes from drift due to tracking errors. As we have not yet completed a full pointing model at all azimuths and elevations, we have not quantified this component yet. The second component of mount motion image degradation is due to tracking jitter. We quantify this by computing the rms deviation of the mount position as measured by the encoders from the

[3] A next-generation DIMM developed by Andrei Tokovinin and Edison Bustos

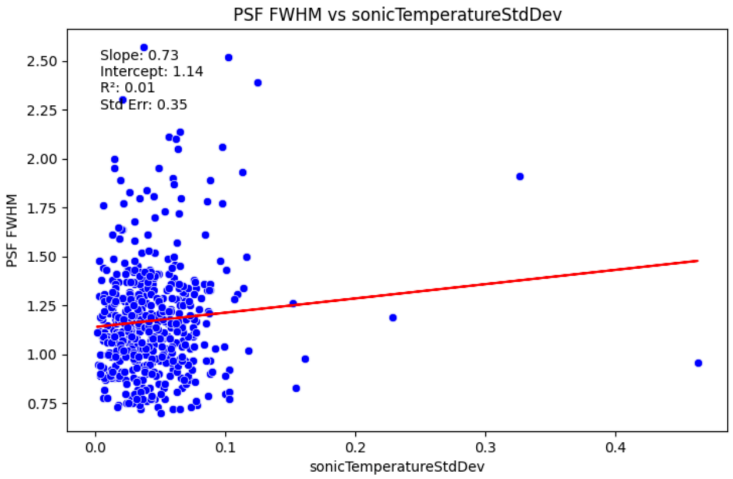

Figure 19: PSF FWHM versus the standard deviation of sonic temperature.

position sent by MTPtg. We computed the tracking jitter for all ComCam exposures through the 20th of November. From a total of 5311 images, the median image quality impact is 0.004 arcseconds, and 0.38% of images have an impact to image quality of above 0.05 arcseconds (see Figs. 20, 21, and 22). This is well below the budgeted mount jitter error of 0.069 arcsec.

5.2.6 PSF Modeling

Two different PSF models are currently used in the DM pipeline: PSFEx, which provides a fast preliminary PSF estimation, and Piff, used later in the pipeline for more accurate PSF modeling. During the initial data collection with ComCam and AOS testing, most in-focus star shapes exhibited doughnut-like patterns, reflecting residual optical aberrations that had not yet been corrected. This specific form of asymmetry posed challenges for PSF modeling and was not typical. Interestingly, Piff, despite being the more advanced model, struggled to handle the large, non-symmetric PSFs compared to PSFEx. Fig. 23 shows how we were able early in the observation to constrain the PSF.

However, as the AOS system improved image quality and produced more symmetric PSFs, we observed behavior more consistent with expectations for both PSFEx and Piff. Analysis of second-moment reconstructions shows that PSFEx has a systematic offset in size reconstruction compared to Piff, which aligns with observations from DES. Overall, Piff demonstrates better PSF reconstruction, as illustrated in Fig. 24. *Note added in proof: further analysis shows that Piff's relatively poor performance was due to an inconsistency between Piff's handling of the*

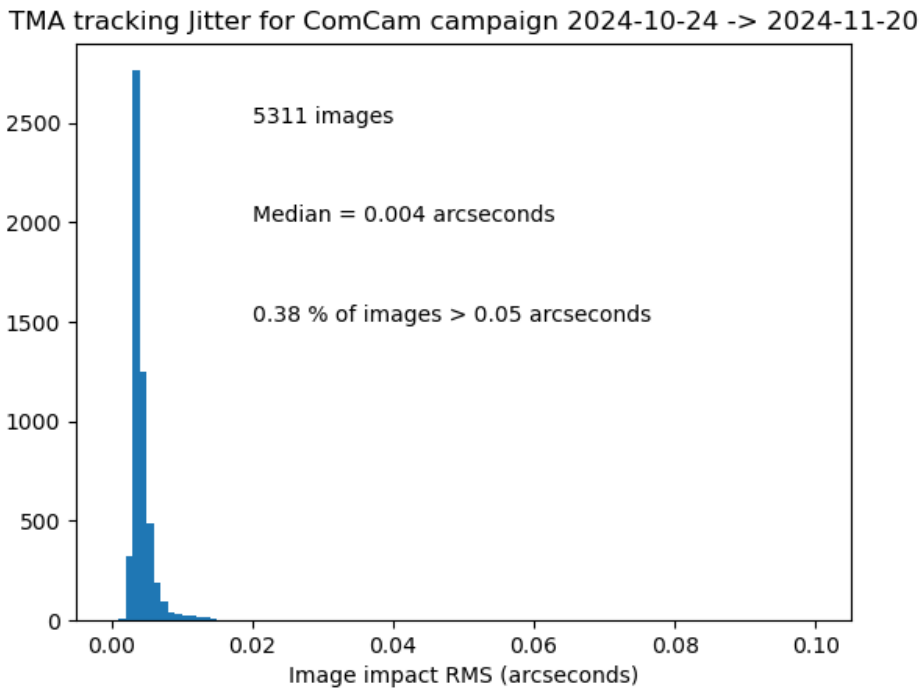

Figure 20: Total TMA tracking jitter for all exposures from October 24 to November 20.

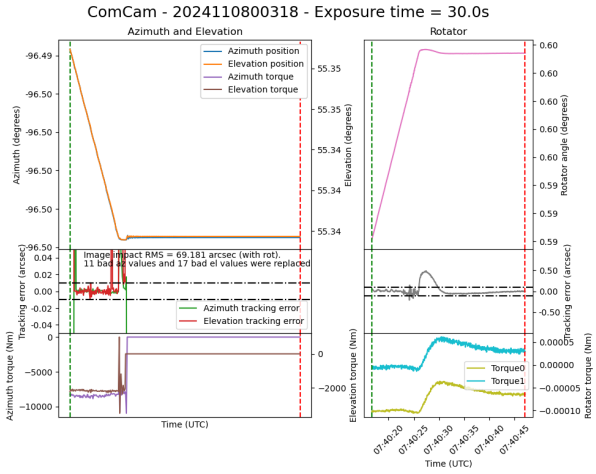

Figure 21: Exposure with an unusually large amount of mount motion image degradation.

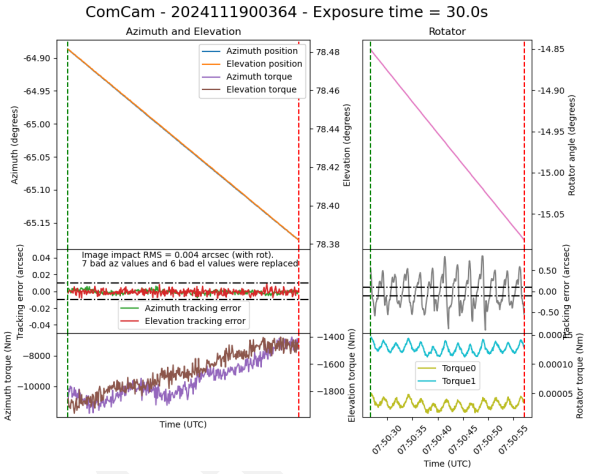

Figure 22: Exposure with a typical amount of mount jitter.

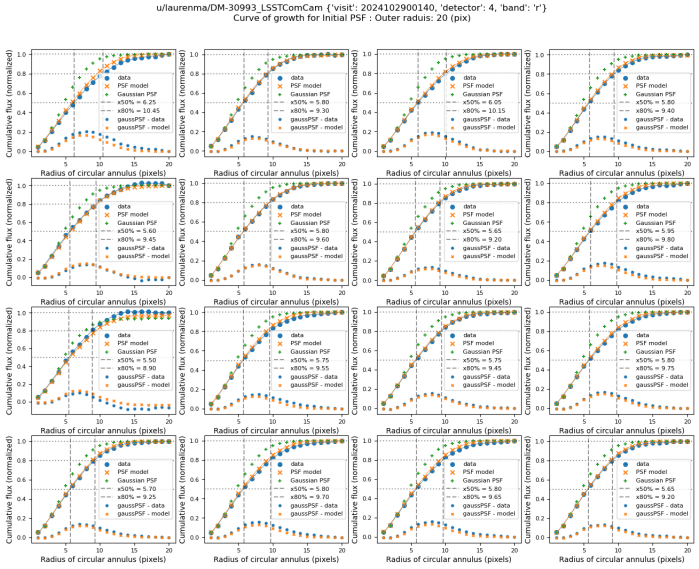

Figure 23: Growth curves of the PSF compared to its model (PSFex here) in the early data taken with ComCam.

centroid and the convention employed by the Rubin pipelines, and that in fact Piff is able to outperform PSFEx on these data.

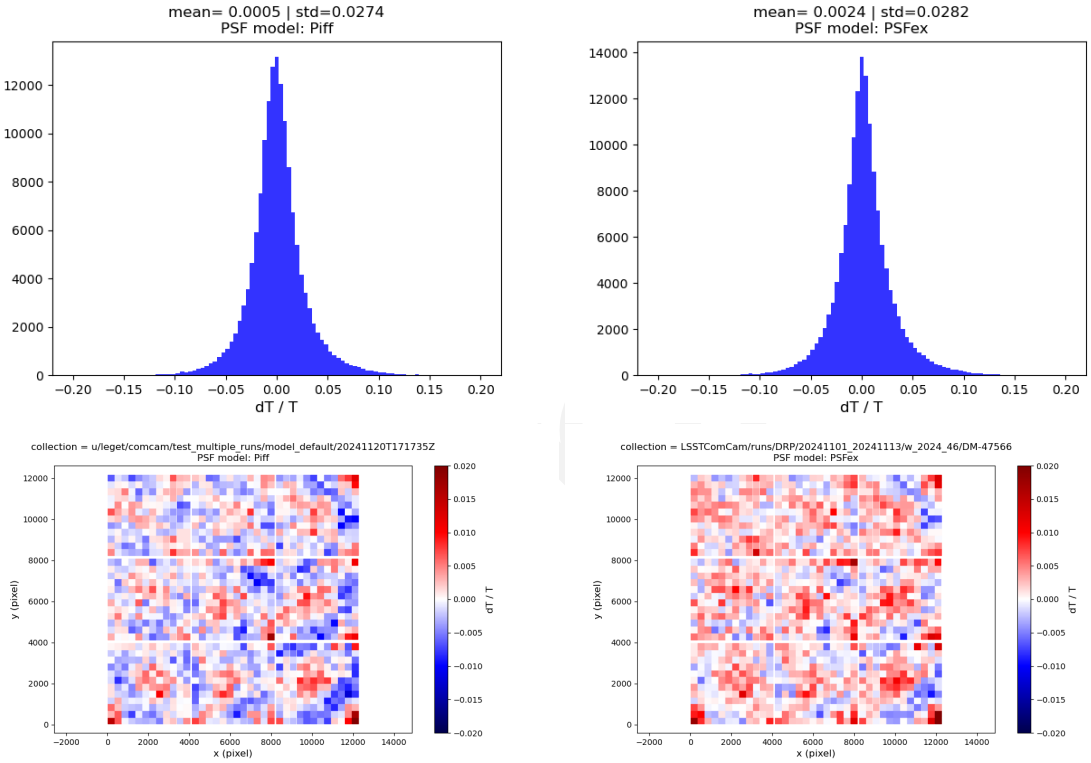

Figure 24: Size residuals for Piff and PSFex (1d distribution and 2d average across visits). Piff has no offset and smaller scatter. Both panels exhibit spatial structure across the focal plane, based on spatial averages across all science visits. The PSF is modeled per CCD in pixel coordinates using a second-order polynomial for interpolation. The observed structure is unlikely to result from atmospheric or dome effects, given that this plot represents an average across visits. Instead, it likely reflects spatial variations not captured by the second-order polynomial interpolation, such as optical aberrations or sensor anomalies.

5.2.6.1 Understanding PSF Physics

With LSSTCam, we aim to leverage wavefront sensor data to estimate the optical system's current state and model the optical contribution to the PSF, ultimately building a physical PSF model. During AOS testing with ComCam, the optical state was estimated using out-of-focus images to predict the optical contribution to PSF shape. A ray-tracing analysis showed that the optics fitted from these images could predict the PSF shape, providing strong evidence that a physical PSF model could be developed for LSSTCam (See Fig. 25)

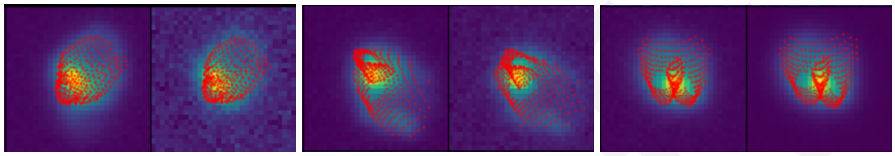

Figure 25: In-focus stars and prediction from the ray tracing on predicting PSF shape (red-dot). Optics parameters on the ray tracing side were derived from out of focus images by measuring optical aberration on "donuts" (out of focus star).

5.3 Differential Chromatic Refraction

Differential chromatic refraction (DCR) occurs when light passes through Earth's atmosphere, refracting more for shorter wavelengths, which causes blue light to appear shifted closer to the zenith. This wavelength-dependent effect results in the smearing of point sources along the zenith direction, specifically parallel to the parallactic angle. The DCR effect is observable in LSST ComCam data, particularly in the angular offset versus g-i band magnitude difference plots (Fig. 26). Fig. 26 contains all direct sources with SNR > 10 from 41 visits from 26 November 2024. When looking at data perpendicular to the parallactic angle, sources show no DCR effect (as expected), forming a clear vertical distribution on the hexbin plots. In contrast, sources parallel to the parallactic angle exhibit a tilted, linear distribution, clearly demonstrating the relationship between angular offset and the g-i band magnitude difference—a visual indication of the DCR effect.

6 Image Inspection

The prospects for human-based inspection of the vast number of images to be produced by the Rubin/LSST are unavoidably going to be limited to a fraction of the dataset produced (even nightly, let alone for the full 10-year survey). Yet, the potential value of getting human eyes

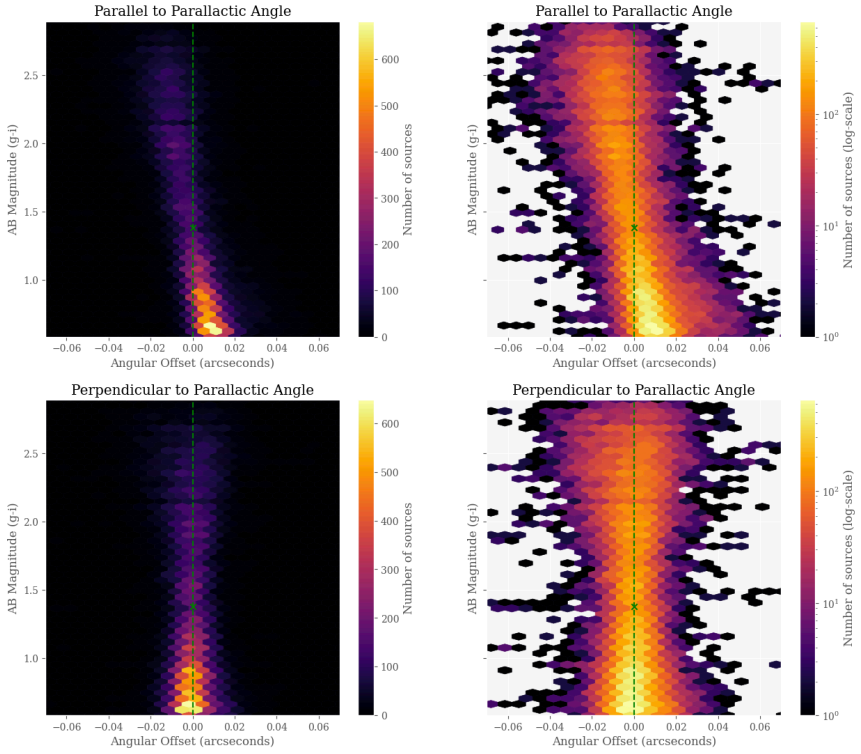

Figure 26: Visualization of Differential Chromatic Refraction (DCR) observed in the ComCam commissioning campaign. The g-i color is computed for every source in the reference catalog that is matched to a direct source in the science image, and the binned density for the full survey is plotted against the angular offset between the reference and detected positions. The angular offset is projected along coordinates parallel and perpendicular to the parallactic angle of the observation, and shows a characteristic correlation along the parallel axis with no correlation along the perpendicular axis. The green vertical dashed line indicates the expected g-i magnitude distribution at zero angular offset, while the green "x" marks the average g-i magnitude of the plotted sources.

on the images (including the raw, minimally processed, and final processed and calibrated stages), is immense, in particular for identifying patterns that are easily spotted by eye, yet tend to evade most modern automated image quality assessment protocols.

Every dataset from any given observation program comes with its own unique set of "features" stemming from the observatory structures, optics, camera, detectors, electronics, observation strategy, the night sky, calibration products, etc. This makes eyeball inspection particularly valuable in the early days of commissioning. Fortuitously, the energy and enthusiasm of internal project members are at extrememly high levels at this stage, so there is no shortage of voluntary effort for human visial inpsection for the commissioning phase of the ComCam. This effort to date has largely proceded via an informal see-something-say-something scheme, with many users posting their latest findings on the internal staff Slack channels (namely the #sciunit-image-inspection channel, but also prominently in other channels, #sciunit-lsb, #validation-team, #embargo-beautiful-images, #ops-satellites, #dm-calibraion-products to name a few).

Anomalies and peculiarities reported to date along with details of and/or pointers to further study and explanation (where applicable) include:

- **ghosts** See Sec. 10.
- **stray/scattered light**: prominent ring-shaped waffle/corduroy-like features seen early on were identified as originating from a blinking light on a crane that was left on. Large irregular ring-shaped "spots" were attributed to the laser tracker (an issue in access to turn it off was noted). ComCam is known to be less well baffled than LSSTCam, so scattered light from off-axis light sources is expected to be worse.
- **satellite streaks**: see Sec. 11.1
- **background subtraction issues**: see Sec. 10
- **repeated patchwork gradients**: a small number of images appear to have a bias gradient that appears in several amplifiers of detector 1 (R00_S01). This feature is currently under investigation, but it appears to be most prominent when a bright star resides close to the amplifier (right) edge of this detector. The bias shift appears in the prescan, active area, and overscan regions of the affected amplifiers. It seems likely that this is some type of crosstalk, but the origin and manifestation is unclear. It remains to be seen

whether similar features are seen in any other detectors. It is likely that this feature will be further studied in the context of Sec. 7.1.

- **trailed sources**: due to tracking errors. These are particularly difficult to identify with automated image quality metrics (there are some ideas about using AI to identify tracking error-based image degradation floating around, but we also hope to be able to confidently rely on data from the EDF to indicate tracking issues).

6.1 Future Endeavors

A major goal for future image inspection efforts is to develop a more systematic way to identify and report issues and, where possible, alert the relevant stakeholders for further investigations into mitigating problems.

There has been some effort to deploy the "Exposure Checker" that was developed for the Dark Energy Survey (Melchior et al., 2016)[4] and has been previously deployed by LSST DESC for the visual inspection of simulated DC2 data (LSST Dark Energy Science Collaboration (LSST DESC) et al., 2021).

Also recently implemented for visual inspection is a rendering of the 3-color coadd HIPS maps produced regularly during the nightly validation and DRP processing runs. Such images are invaluable for highlighting myriad issues at the coadd level (often indicating a need to drill-down to the visit-level for a full diagnosis, while providing significant clues on where to look first).

7 Calibration Data and ISR

7.1 Instrument Signature Removal

The quality of the instrument signal removal (ISR) has improved during commissioning, as we create and deploy updated calibration products that better represent the ComCam system. The following discussion summarizes our current understanding of a variety of features, both expected and newly seen on ComCam, and presents our expected prognosis of the behavior of the full LSSTCam.

[4] See demo `https://des-exp-checker.pmelchior.net/`

7.1.1 Phosphorescence

There are regions on some of the detectors (most visible in R22_S01, detector=1) which show bright emission, particularly at bluer wavelengths, as shown in Fig. 27. This is believed to be caused by a thin layer of remnant photo-resist from the manufacturing process that remained on the detector surface, and is now permanent due to the subsequent addition of the anti-reflective coating. In addition to the large areas, there are also discrete point-source-like or cosmic-ray-like defects caused by accumulations of this material. Adding to the difficulty of mitigating these defects is that this photo-resist is known to be phosphorescent, explaining why these regions are more noticeable in the bluer filters.

The initial studies of this show that these features can continue to emit light up to several minutes after they've been illuminated. Due to the long duration of these features, we decided to place manual defect masks over the worst regions. The first of these manual masks takes up about 3.5% of that detector, smaller than but consistent with estimates that this would create a pixel loss of approximately one amplifier per detector.

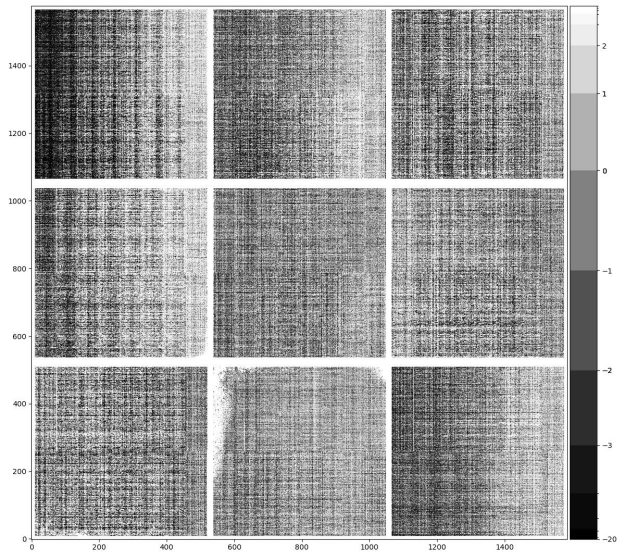

Figure 27: The phosphorescence seen in R22_S01, shown here in a dark exposure taken after a series of twilight flats (exposure=2024112000065). This material absorbs light at bluer wavelengths and re-emits that energy over a wide range of wavelengths.

The ITL detectors in LSSTCam are believed to have been cleaned better, so this should be less

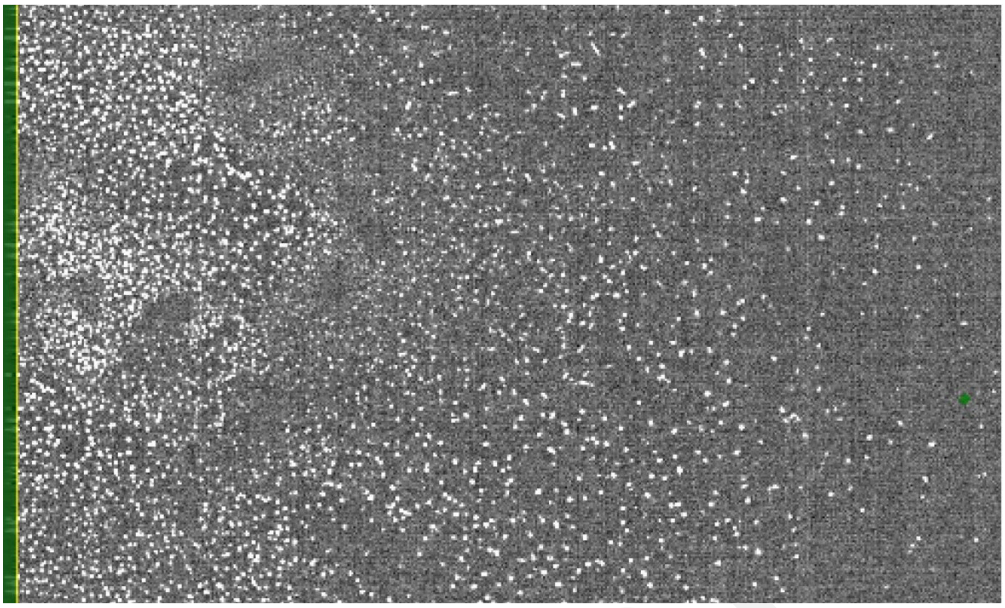

Figure 28: A full-resolution view of the edge of R22_S01. The features shown in this image are point-like sources caused by the trapped phosphorescence photo-resist.

of an issue on the full camera.

7.1.2 Vampire pixels

There are defects on ComCam that have been classified as “vampire” pixels, as they appear as a bright defect with a (generally) axisymmetric region surrounding the bright core, as if the defect is draining charge from its neighbors. The naming is at least broadly correct, as integrating to large radii shows that these regions do appear to conserve charge. There is an intensity dependence that makes these vampire pixels different than standard hot pixels, as these pixels do not show up on dark frames, only on flats and science exposures, where the detector surface is illuminated. After the initial discovery of the bright obvious vampires, we added new masking code that identifies the bright cores that are above 2.0 on the combined flat (pixels that are greater than 200% of the median flat level), and adds circular masks to the defect list. This appears to find the most problematic examples, but as we have improved flat quality during commissioning, we are finding that there is a sub-population that are not as severe, but likely have a similar physical mechanism. This population is still bright on the flat, with peaks around 1.2 (20% elevated relative to the flat), and may need to be masked as well. From an initial study in the lab, it appears that all ITL detectors on LSSTCam have a

few of these kinds of defects, with two detectors approaching similar contamination levels as R22_S10 on ComCam.

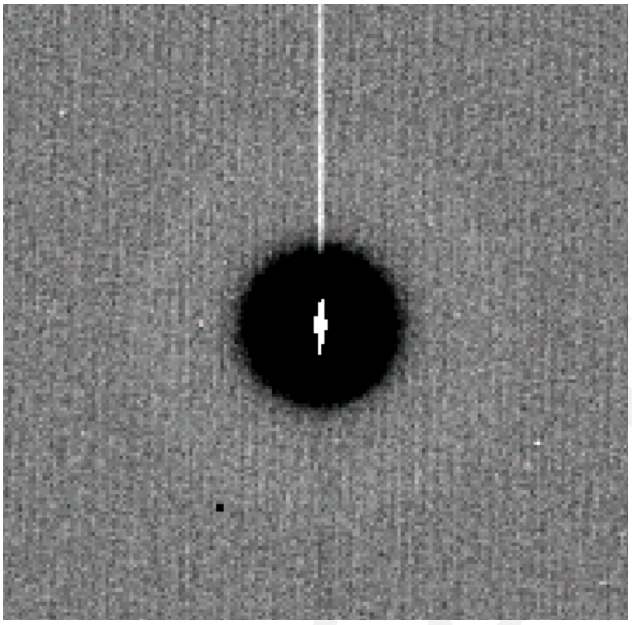

Figure 29: A close up of one of the largest vampire pixels. The bright core and region of depletion are clearly visible. Currently we only mask the core and depleted region, but will be extending this to mask the persistence-like trail that this feature leaves in the next few weeks.

7.1.3 Saturated star effects

Although we expected to find saturated star trails coming from bright sources, the observed behavior of these trails is unique. Saturation spikes on most cameras appear as streaks extending from the core of the bright source along the direction of the parallel transfers, and truncate as the charge bleeds run out of charge (and can no longer overcome the potentials defining the pixel). The trails seem with ComCam, however, extend the entire height of the detectors, crossing the midline break (as is to be expected in the ITL, but not the E2V, CCDs). These trails are also not at the expected high state, with the centers of these trails having flux levels lower than the average sky levels, creating dark trails (See Fig. 31), On the worst saturated objects, there is also evidence of charge pile-up near the serial register, which can then create fan-like bright features at the edge of the detector. Those bright features can also then crosstalk onto other amplifiers.

The underlying physics is not well understood. The leading theory is that photo-electrons

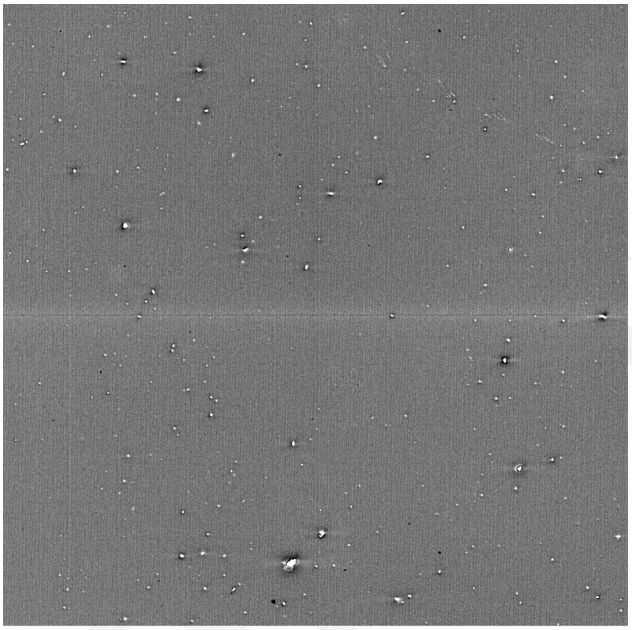

Figure 30: A view of detector R22_S10 in y-band, which has a large number of less significant vampire pixels.

Linked Figure

Figure 31: A portion of `day_obs 20241127 seq_num 488` showing the vertical bands which are apparently produced by very bright (saturated?) pixels.

entering the n-doped channel stops partially cancel the effects of the holes, leading to electric fields which produce an effect similar to a one-dimensional Brighter-Fatter effect, visible in the background level as well as in objects. Further study is needed to see if we can correct these trails outside of the regions of charge buildup. Until we have a correction, we plan to begin masking both the trail and the fan-spread near the serial register.

Although we haven't seen identical features on LATISS (possibly due to the much lower sky levels), the presence of these odd trails on all ComCam detectors suggests that this is a property of the ITL devices, and so will likely be seen on LSSTCam as well.

7.1.4 Gain ratios

ComCam has been the first large-scale application of the updated "IsrTaskLSST" task, which uses a model of how the various signals combine to form the raw images to inform how we correct those signals during the ISR process. One improvement of this new task is that we now apply per-amplifier gains before flat correction, removing the gain component that was previously included in the flat correction. This results in the flat containing mainly QE and illumination patterns, which is much "flatter" than flats that also include gain terms (which offset the amplifiers relative to each other).

If we have properly diagonalized the flats and the gains, we would expect that applying the gain correction would create images with consistent sky levels across different amplifiers. However, when we look at images taken on-sky, our initial gain values result in some amplifiers being significantly different than their neighbors (Fig. 32). The gains that we use are derived from the photon transfer curve (PTC), which uses flat pairs at different flux levels to monitor the properties of the noise. We have two of these sequences taken in the lab, and they disagree at the few percent level. This is similar in scale to the errors necessary to explain the on-sky differences. Further complicating this issue, the offsets seen in twilight data (used for flats) and that seen during the night also seem to differ (Fig. 33) These differences so far have not been found to correlate with any device temperature, time, or voltage values. The gain correction fix appears to be stable, as we've only needed to generate and apply it once.

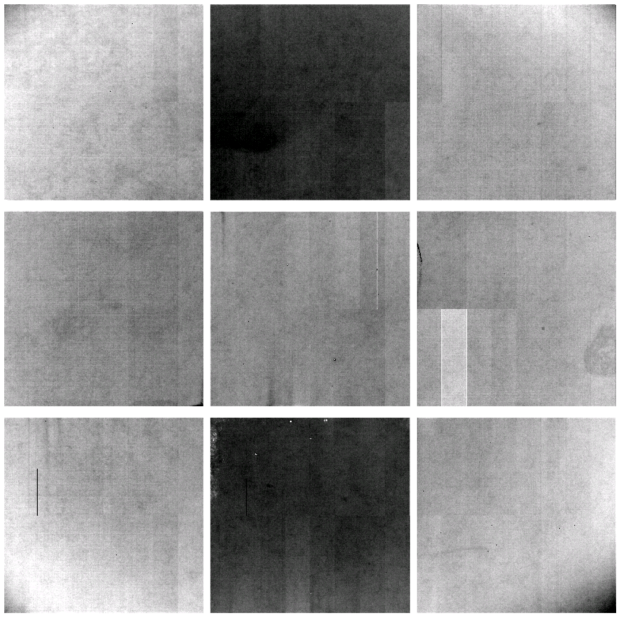

Figure 32: The ratio of the twilight-flat divided by a flat constructed from 94 r-band science frames. The scaling ranges from 0.9905 to 1.007. The visibility of amplifiers is caused by the unknown gain errors. The bottom right corner amplifier (C07) on R22_S21 is one of the indicator amplifiers, as it diverges from its neighbors. Although the C00-C03 amplifiers in R22_S12 also show significant offsets, these amplifiers also have an unrelated CTI issue, making them less reliable indicators.

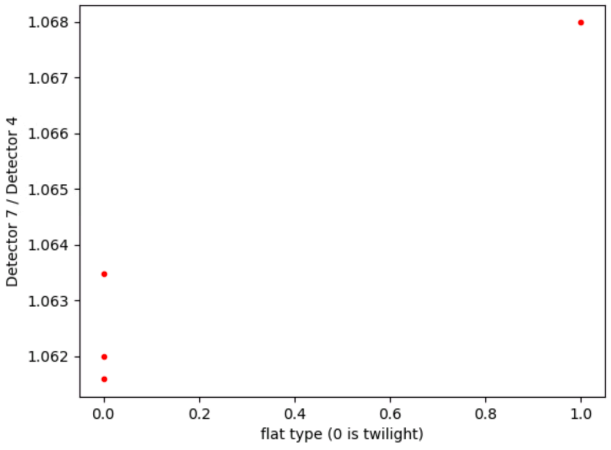

Figure 33: A comparison of the gain ratio between amplifiers in R22_S12. C07 is chosen as the indicator amplifier, and C04 is the reference. We have three twilight flat measurements taken at different rotator angles, and one from the 94 input sky flat.

7.1.5 Crosstalk

We are currently using crosstalk values that were constructed by averaging the lab-based ITL measurements taken on LSSTCam. These are working well, with residuals post correction being only a few electrons peak to peak. We plan to do a more complete crosstalk study using on-sky data, but the current results suggest that these lab measurements are sufficient for ComCam, and expect the same to be true for LSSTCam.

7.1.6 Twilight flats

Because the flat field screen and illuminator was not available while ComCam was on the telescope, we used dithered, tracked twilight flats to generate the combined flat calibration frames. The exposure time of the twilight flats were dynamically adjusted to hit a target count, generally in the range of 10-20k. The flats taken at a wide range of azimuth angles and rotator angles. See Fig. 34 for the counts per pixel per second as a function of sun elevation angle.

This reduction of non-sky signals is imperfect, and an early i-band flat showed a satellite trail as a result; this was remedied with a more recent flat built using a larger number of exposures.

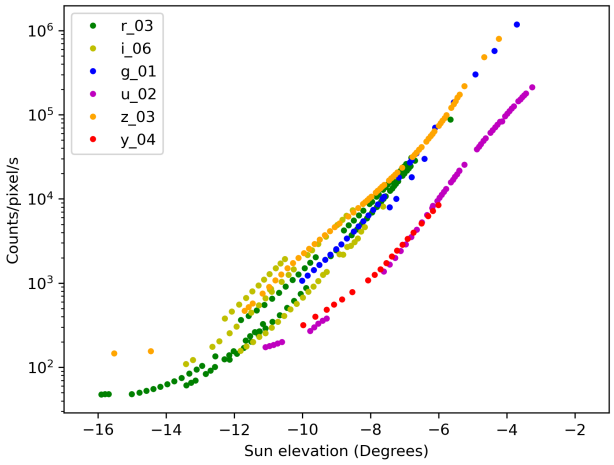

Figure 34: Twilight flat counts per pixel per second for each filter as a function of sun elevation angle.

7.1.7 Operations

The Telescope and Auxiliary Instrumentation Calibration Acceptance Board (TAXICAB) has been meeting previously to discuss LATISS calibrations, and has been helping manage calibrations for ComCam. This process has not prevented problematic calibrations from being deployed (like the i-band flat with the satellite trail), but it has ensured that multiple people have checked some set of results. We are generating calibration verification reports regularly as part of this process (available at `https://s3df.slac.stanford.edu/people/czw/cpv_reports/`), and plan to add new metrics and checks to these as we discover more features of these detectors.

7.2 Collimated Beam Projector Status

The Collimated Beam Projector (CBP) and Ekspla tunable laser were both installed on the dome during the week of November 18. See Fig. 35 They will both be connected to ethernet and a laser interlock system will be installed. First photon from the CBP was achieved on 2024-12-08 (Fig. 36).

8 Astrometry

This update on astrometry quality is based on data collected halfway through the ComCam observations. It is important to note that so far only single frame astrometric calibration is being done. Doing the additional global astrometric calibration with GBDES will further improve the results presented here.

For now, metrics like AM1 (the RMS of distances between star pairs separated by 5′ across all visits on a tract) appear to be satisfactory. On average, the median value across different filters is around 10 mas, as shown in Fig. 37.

When examining the average astrometric residuals projected across the focal plane, some structures appear to be present, as in the example below in Fig. 38. However, more data is needed to confirm whether these patterns are noise or systematic effects. It is likely that GBDES will help address these structures once it is activated.

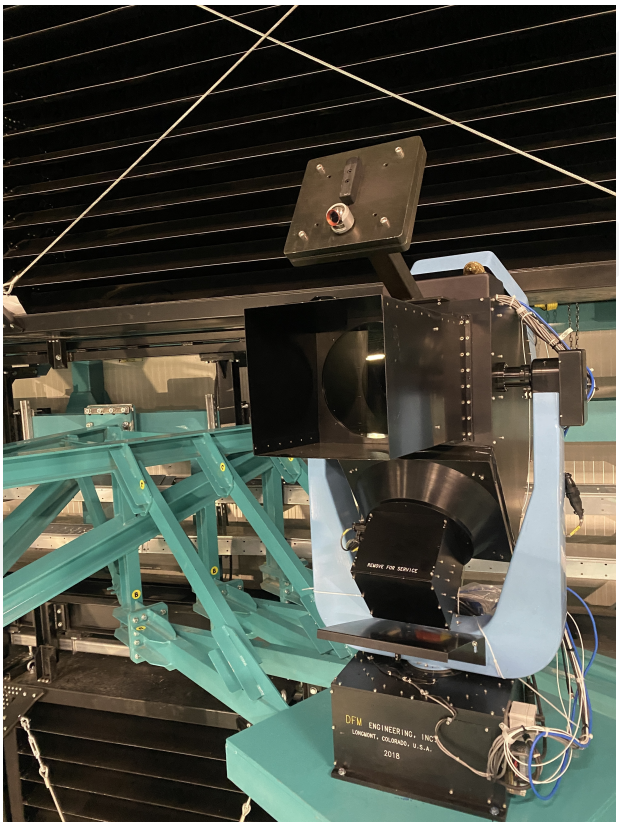

Figure 35: Image of the CBP, which was installed on the dome on November 22.

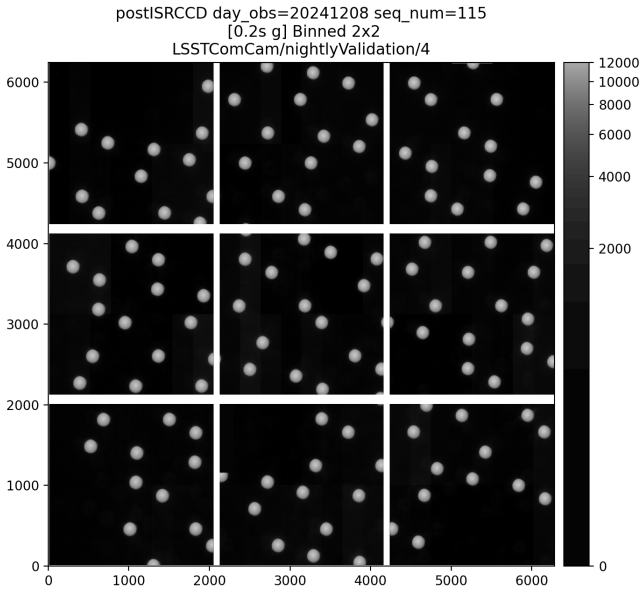

Figure 36: ComCam image of CBP spots.

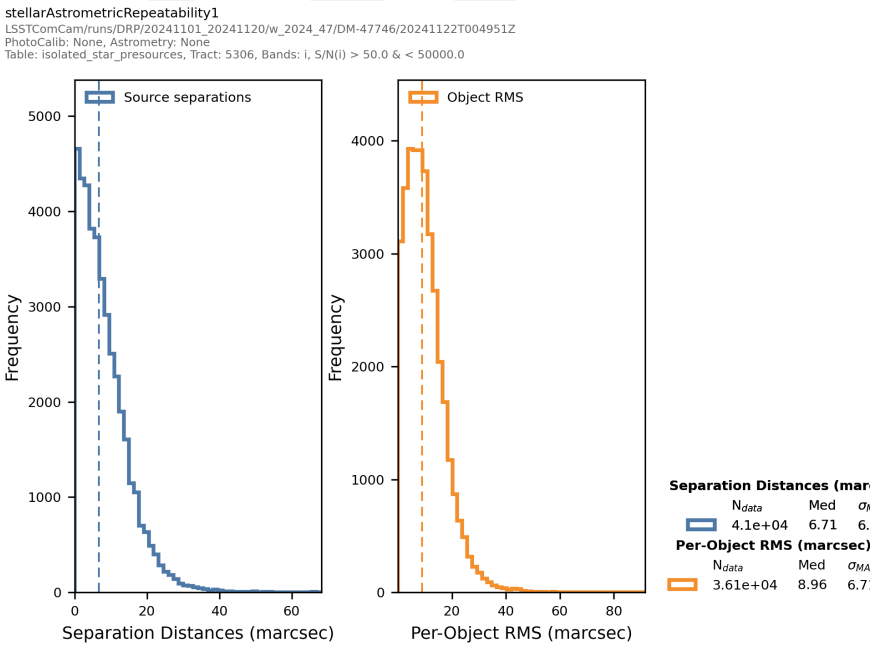

Figure 37: Stellar Astrometric repeatability in filter I in a given tract. AM1, which is the median of the orange histogram, is below 10 mas.

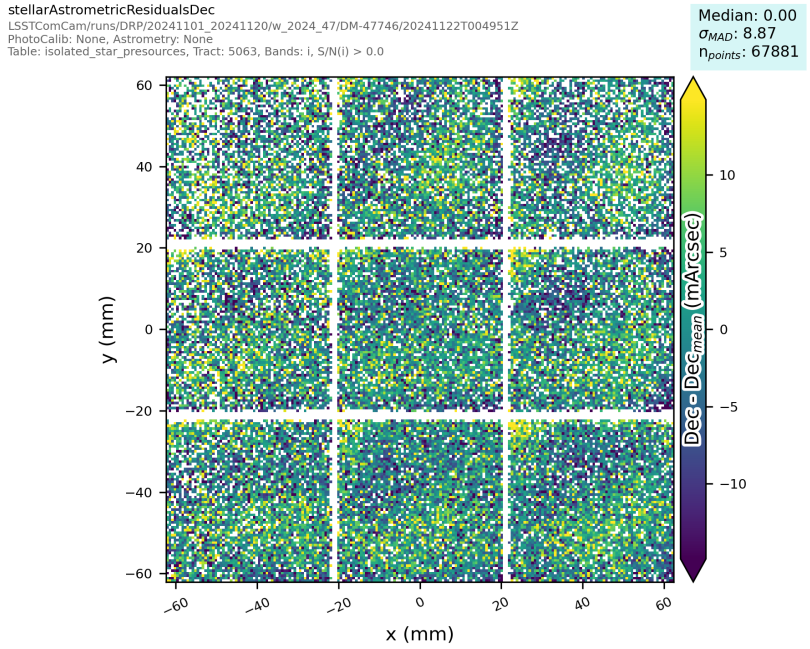

Figure 38: Declination residuals projected in Focal plane coordinate for a given tract. Some structure looks to be present in focal plane coordinates, which will be taken into account with GBDES.

9 Static-Sky Photometry

9.1 Photometric Calibration

We have started commissioning the full photometric calibration pipeline for Rubin Observatory, with great success so far. For testing photometric calibration we have obtained over 150 dithered science observations in ugriz over part of the Extended Chandra Deep Field-South (ECDFS) (one of the planned LSST deep fields), and tens more in rizy over part of the Euclid Deep Field South (EDFS). All of the science data has delivered seeing of ~ 0.8 to ~ 1.5 arcsecond seeing. The validation work in this document covers the ECDFS field with its more complete filter coverage.

The precision photometric calibration software used for Rubin is the Forward Global Calibration Method (Burke, Rykoff, *et al.* 2018) which was used successfully to achieve better than 2 mmag uniformity for the Dark Energy Survey. This software has been adapted for the LSST Science Pipelines and has been used on Hyper Suprime Cam Special Survey Program (HSC SSP) for data releases since DR2. The performance on HSC data has not been as good as that

on DES data due to a number of reasons, yielding repeatability and uniformity closer to the 5 mmag level for grizy data.

Early calibration of the ComCam data is in many ways easier than that of HSC. First of all, we have a smaller camera (9 detectors) and thus fewer variations to have to cross-calibrate. Second, the camera is situated in the center and easiest to calibrate part of the focal plane. Third, we only have one field to calibrate across a few nights of data so far over a limited range of airmass. Fourth, the survey strategy (multiple bands per night dithered and repeated with overlapping filters from night to night) is well suited to self-calibration. On the other hand, we do not yet have detailed filter or detector scans available for ComCam using the CBP (Sec. 7.2), and are therefore using the LSSTCam reference filter curves and average detector throughput for the LSSTCam ITL detectors. In addition, we do not have a flat field screen so we have had to rely on twilight flat observations for flat fielding.

9.1.1 Processing Overview

We start with the standard ISR as documented in Sec. 7.1. While there are a number of challenges that we have discovered with the ITL detectors, these are mostly near the sky level, while the testing of photometric calibration is focused on brighter stars that are less affected by these issues. We then apply twilight flats, which we are investigating how to make better. At the same time, we are going to have the flat field screen and laser and projector installed prior to the commissioning of LSSTCam, so we do not want to spend too much time worrying about specific challenges of twilight flats which are only necessary for ComCam.

After flat fielding we find an initial point-spread function (PSF), do a star selection based on source and psf moments that was developed for HSC single-frame processing, and perform an initial astrometric solution and photometric solution (with a single zero-point per detector). The initial astrometric solution is used to associate star observations together prior to global photometric calibration with FGCM. The initial photometric solution is used for rapid analysis and prompt processing, but is not used at all for FGCM which relies entirely on instrumental fluxes (in units of electrons) with a minor constraint from the reference catalog.

9.1.2 Global Photometric Calibration with FGCM

All associated stars with observations with signal-to-noise greater than 10 are input into the FGCM solution. In addition, reference stars from The Monster reference catalog are associated with the stars. Only a small fraction of the reference stars are used in the FGCM solution, sufficient to estimate an "absolute" calibration (trusting that The Monster is a good absolute reference catalog). There is additional ongoing work with absolute calibration with respect to the CalSpec star C26202 which is not saturated in LSST images and is fortunately contained in ECDFS that is described in Sec. 9.2.

The FGCM model constrains the atmospheric parameters per night, as well as the absolute throughput relative to the input scans. The standard atmosphere is given by MODTRAN, run at the elevation of Cerro Pachon at airmass 1.2 with an Angstrom aerosol model. The optics and filters are all taken from `lsst/throughputs` version 1.9, and the detector throughput is taken from the ITL average of the lab scans ingested into `obs_lsst_data`. Note that the detector QEs are normalized to 1.0 at 800 nm, which is certainly greater than the true QE at this wavelength.

9.1.3 FGCM Results on the ECDFS Field

The FGCM results presented here are based on the `LSSTComCam/runs/DRP/20241101_20241113/w_2024_46/DM-47566` DRP processing run, specifically the 157 visits overlapping tracts 4847, 4848, 4849, 5062, 5063, 5064 which are in the ECDFS field. Specifically there are 28, 18, 38, 45, 28 visits in ugriz respectively. All QA plots are available in the plot navigator at USDF in the collection `u/erykoff/LSSTComCam/DM-47303/test2/build2/run9`. In this section we focus on some of the highlights.

Note that FGCM defines a "photometric" observation as one that is consistent with the forward model, including normal variations in the atmosphere, airmass, known detector throughputs, filter curves, and additional accomodation for aperture corrections (discussed in Burke, Rykoff *et al.*). With this definition fully 92% of the observations were deemed to be photometric by the code.

9.1.3.1 Illumination Corrections

Part of the FGCM solution is generating illumination correction maps (Fig. 39) with a second-order 2D Chebyshev polynomial over each detector. Prior to LSSTCam commissioning this will be turned into a separate calibration product generated from dense dithered star field observations (Y1). We have not yet done dithered observations with ComCam over a dense field, only high latitude, which limits the precision. Nevertheless we are able to constrain reasonable illumination corrections. The offsets from detector to detector in the illumination correction are due to unexpected offsets in the twilight flats that we are investigating.

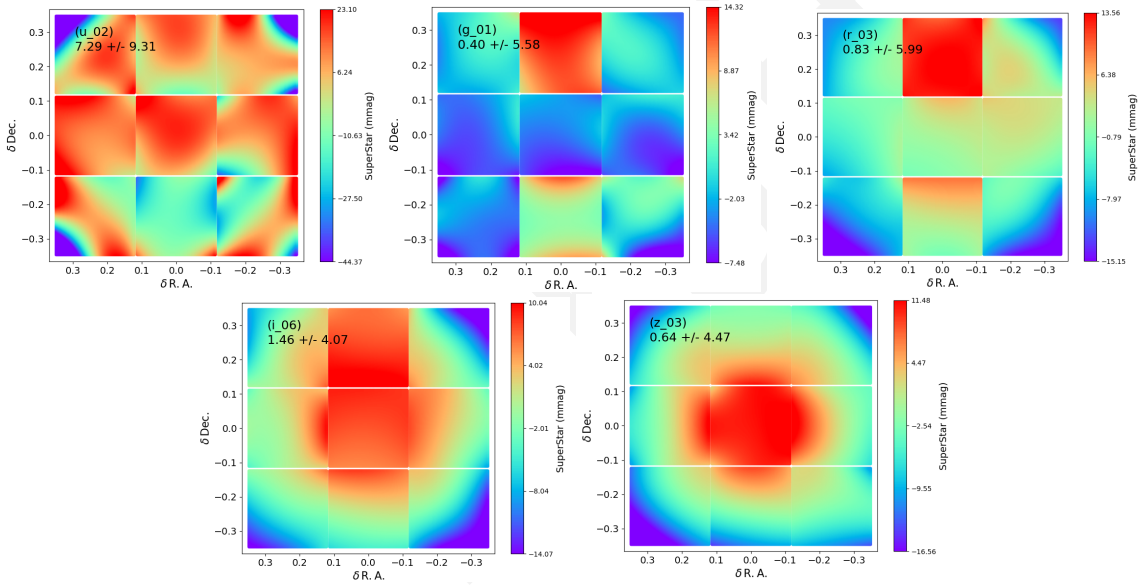

Figure 39: Illumination corrections derived from FGCM for the ugriz bands.

9.1.3.2 Photometric Repeatability

The photometric repeatability after the FGCM fits was excellent. We show here the repeatability histograms, after all chromatic corrections, for the stars used in the fit ("all stars"). Although 10% of the stars are reserved, the histograms do not yet have good statistics. These plots are all made with signal-to-noise greater than 100 stars (with better than 1% photometric errors). Therefore the scatter is often dominated by photometric error. The label "sigma_fgcm" is meant as an estimate of the intrinsic scatter after subtracting off the photometric error in

quadrature. The plots are split into four panels, showing all stars, the 25% bluest (from $g - i$ color), the 50% middle color, and the 25% reddest stars. Note that the reddest stars tend to be fainter and thus have larger photometric error. Furthermore, there are no red stars observed in the u-band. In all cases except the u-band the intrinsic repeatability is 1 mmag or better, and for the u-band it is better than 5 mmag, comfortably exceeding our requirements in all measured bands.

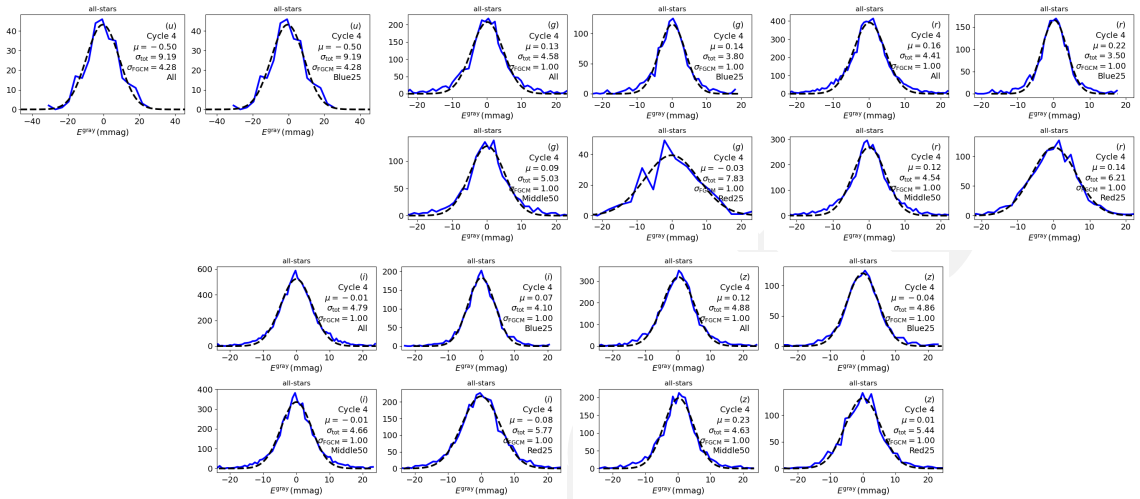

Figure 40: Photometric repeatability for stars in the ugriz bands.

9.1.3.3 Detector Chromaticity Fits

In the absence of full in-situ throughput scans, we additionally constrain the "chromaticity" of the detectors, which is a first-order adjustment to the slope of the peak of the throughput curve per-detector. By doing this adjustment in throughput space rather than color space we can preserve the forward model approach, and additionally apply these corrections to any SED. Note that this operation assumes that the filters are perfectly known, and it is only the detector throughput that is varying. This is, in general, a valid assumption in the g band where the AR coating varies from detector to detector causing chromatic differences in this band.

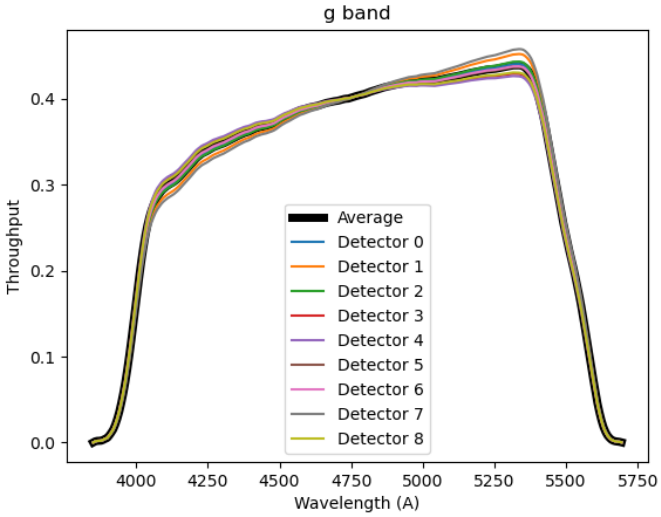

Figure 41: Variation in throughput in the g band for the 9 ComCam detectors as derived from star colors. These are all constrained relative to the average ITL throughput. The CBP will be used for making this measurement "correctly", but this serves as a prediction of what variations the CBP scans should observe when we have it running on ComCam.

9.1.3.4 Absolute Throughputs

The FGCM fit performs a "dead reckoning" of the expected absolute throughput given the telescope aperture, the effective gain, the standard atmosphere, and the various throughputs input. See above for the throughputs assumed. If we trust The Monster reference catalog for absolute calibration, Fig. 42 shows the comparison of the delivered throughput to the predicted throughput. In griz bands it is very close, given that (a) we know that the peak detector QE is not 100%; and (b) the ComCam front lens did not have an AR coat applied, thus reducing its throughput relative to nominal LSSTCam lenses. In u band we are getting more throughput than predicted. This may be an issue with the reference catalog, or our ComCam u-band QE is 20-30% larger than the baseline expectation. Given how fast the detector QE falls off in the u-band, it would not take much to increase the throughput by this factor.

We have additional ongoing studies of absolute throughputs using the CalSpec standard C26202 directly.

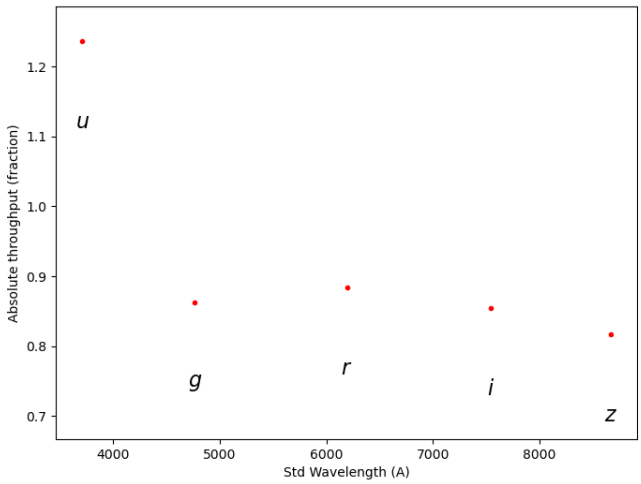

Figure 42: Absolute throughput derived per band, relative to naive expectations.

9.1.3.5 Comparison to The Monster

Given our calibrated stars from the FGCM fit we can compare the magnitudes as a function of color against The Monster reference catalog. The "lsst" fluxes in The Monster were derived by using stellar spectra to convert from The Monster native DES system to the standard throughputs in lsst/throughputs v1.9. These do not match ComCam, in particular it used a strange hybrid of ITL/E2V for the detector throughput, which is not correct for ComCam. Therefore, we do expect residual color terms. Studies are ongoing on whether these color terms are expected given the differences between the ComCam throughput and the predicted LSST throughput. Further validation will be possible if we get CBP scans prior to the removal of ComCam.

9.1.3.6 Background Oversubtraction

As a side-effect in the calibration, FGCM tests local background oversubtraction by looking at the statistical difference between two large aperture magnitudes. If the background were perfectly measured then the difference in magnitude will just be a measure of the wings of the PSF (a local portion of the growth curve) which should be self-similar for all star fluxes.

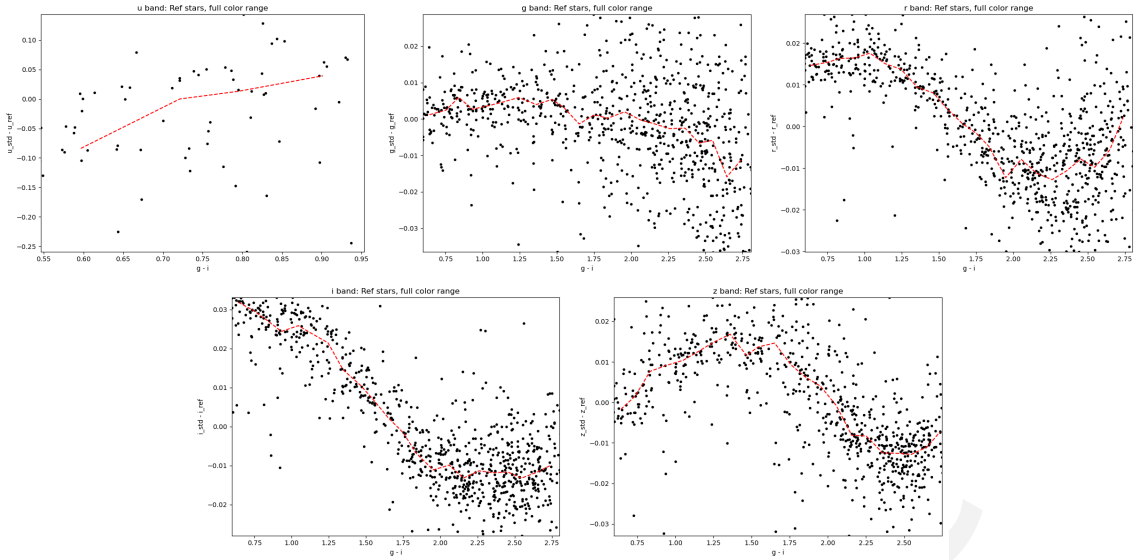

Figure 43: Residuals between FGCM standardized magnitudes and The Monster predicted LSST magnitudes for the ugriz bands as a function of $g - i$, assuming The Monster has the correct absolute throughput.

Instead, we generally see a downturn consistent with a constant background offset. This background oversubtraction has been seen in DES, HSC, and ComCamSim data at similar levels with different photometric pipelines. It is worse in the redder bands. It seems to be caused by the far wings of stars (in DES all stars and galaxies brighter than 17th magnitude in i contribute), as well as possibly due to faint undetected sources. This same background oversubtraction effect is seen in the ComCam images. Further investigations are being done by the low-surface-brightness science unit.

9.1.4 Next Steps

The following additional data will need be taken to advance from our current knowledge:

1. g band observations in the EDFS field, when the g filter is put back into ComCam for the upcoming dark time.
2. Dithered observations in as many bands as possible over a field with much larger stellar density for better illumination corrections.
3. More contiguous dithered survey data in (at least) gri.

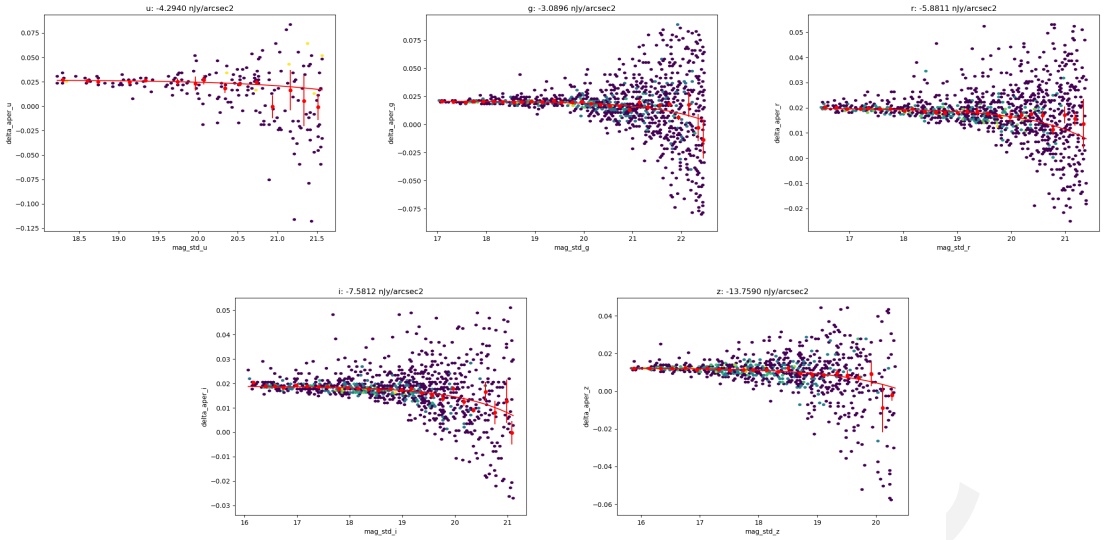

Figure 44: Estimate of the background oversubtraction using delta magnitudes from large apertures in the ugriz bands. The amount of curvature is a measure of the oversubtraction; this should be flat as a function of star magnitude if the background were measured correctly on average.

The particular emphasis on g band in these requests is that by default FGCM will use the $g - i$ color for internal QA, which is a very useful color to split on. There are no facilities in the code for doing quality calibrations on multiple disconnected fields with different band coverage, as this is not the normal case for survey observations. We could run different fields separately with different configs, but this is not preferred. Thus, gri coverage over the fields of interest for DRP processing is the "easiest" path that will yield the best results and be most consistent with the LSST survey.

9.2 A Comparison with the HST CalSpec Standard C26202

The CDFS field observed by ComCam during commissioning contains an HST CalSpec standard that is faint enough not to saturate the ComCam science images. This HST CalSpec standard[5], C26202, had previously been used to perform the absolute AB calibration of the Dark Energy Survey (DES) Data Release 2 (DR2) (Abbott et al., 2021).

For the ComCam data, two separate (but related) analyses were performed using the ComCam

[5] https://www.stsci.edu/hst/instrumentation/reference-data-for-calibration-and-tools/astronomical-catalogs/calspec

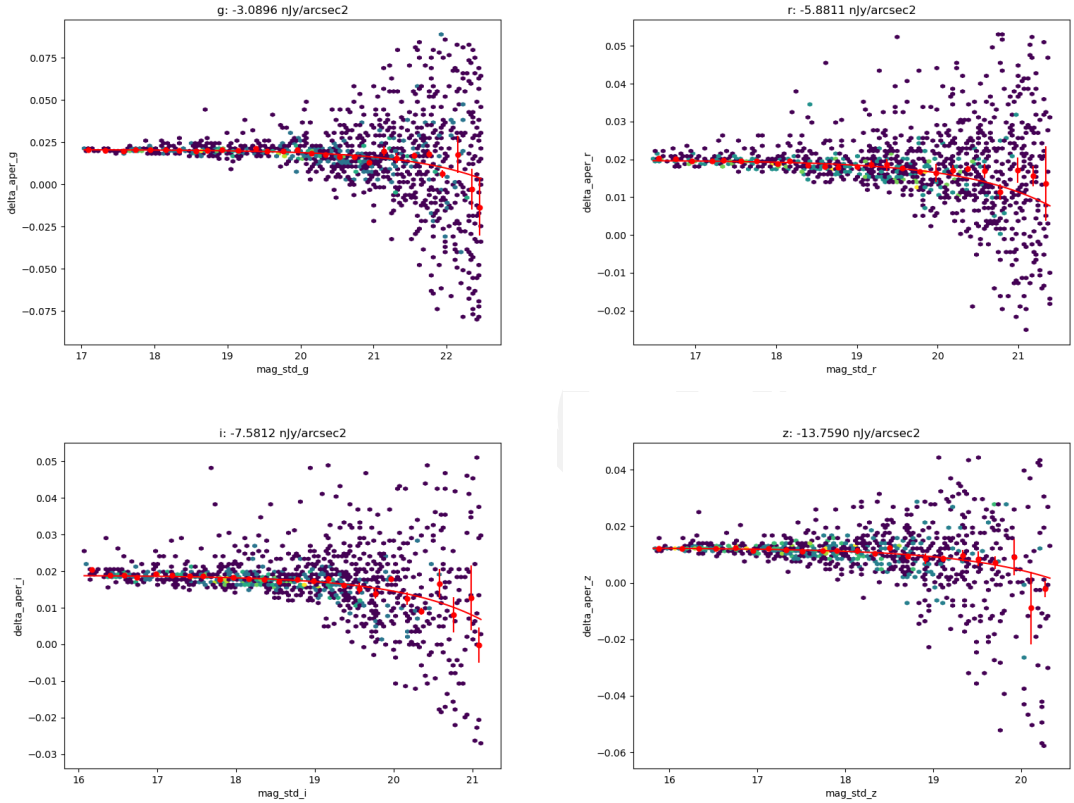

Figure 45: Estimate of the background oversubtraction using delta magnitudes from large apertures in the griz bands. The amount of curvature is a measure of the oversubtraction; this should be flat as a function of star magnitude if the background were measured correctly on average.

observations of C26202: (1) a measurement of the absolute system throughput of the ComCam $ugrizy$ bandpasses, and (2) a measurement of how far off the initial absolute photometric calibrations were from the AB magnitude system ("AB offsets") for these same bandpasses.

These two analyses are discussed below.

9.2.1 Absolute System Throughput Measurements

For the absolute system throughput analysis, the expected total counts (in electrons) for C26202 were calculated for each of the ComCam bandpasses for a 30-second exposure, assuming the engineering system throughputs for an average ITL CCD found in the `syseng_throughputs` repository (see `https://github.com/lsst-pst/syseng_throughputs`). Expected counts in each filter passband were calculated for a range of airmasses ($1.0 \leq X \leq 2.5$) in steps of 0.1 airmass to cover the full range of possible airmasses of the observed ComCam data. Throughout, the HST CalSpec spectral energy distribution (SED), `c26202_stiswfcnic_007.fits`, was used as the C26202 spectrophotometric reference spectrum.

Next, the post-ISR instrumental counts (in electrons) for C26202 were retrieved from the `icSrc` tables from the ComCam observations in the Butler at the USDF. The `base_PsfFlux_instFlux` was used, and an aperture correction from PSF to total flux was applied making use of the `base_CircularApertureFlux_70` as a proxy for total instrumental flux.

Finally, for each of the $ugrizy$ filter passbands, the ratio of the observed total flux to the expected (synthetic) total flux was calculated and plotted. The results can be found in Figure 46. Note that the measured and predicted counts from per-visit synthetic photometry is consistent for all bands at the ~5% level.

9.2.2 AB Offsets

The C26202 AB magnitude offsets are the difference between the calibrated observed ComCam AB magnitudes and the `rubin_sim.PhotUtils`-determined synthetic AB magnitudes for the ComCam $ugrizy$ filter passbands.

The calibrated ComCam AB magnitudes in each of the passbands are obtained by converting the `calibFlux` values in the USDF butler `sourceTable` from nano-Janskys to AB magnitudes via

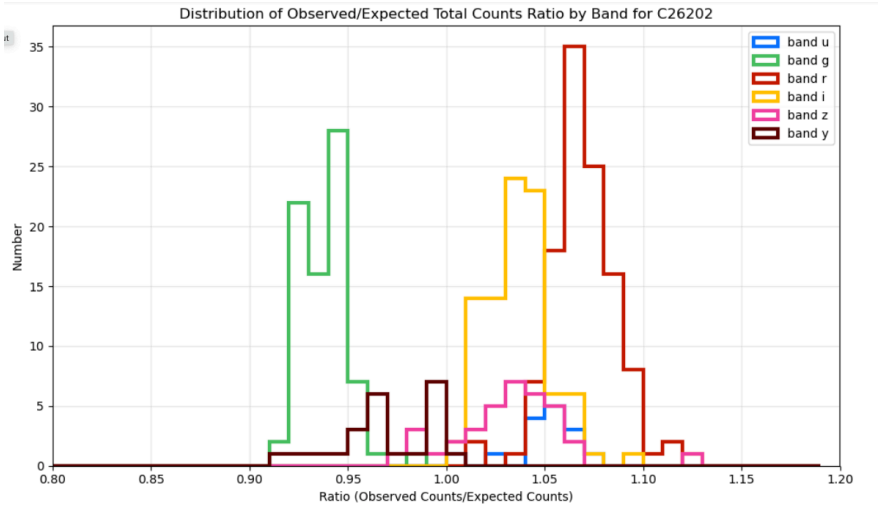

Figure 46: The histogram of the ratio of the observed counts to the expected counts for HST CalSpec spectrophotometric standard star C26202 from ComCam observations in `LSSTComCam/runs/DRP/20241101_20241204/w_2024_49/DM-47988`. Median values of the ratio for each passband are: 1.053 (u), 0.939 (g), 1.068 (r), 1.037 (i), 1.037 (z), and 0.967 (y).

the equation $mag_{\mathrm{ab}} = -2.5 \times log_{10}(calibFlux) + 31.4$.

As with the absolute system throughput measurements for the expected counts of C26202, the engineering system throughputs for an average ITL CCD found in the `syseng_throughputs repository` were used for calculating the expected AB magnitudes with the `rubin_sim PhotUtils` module for each filter bandpass. Also, as with the absolute system throughput measurements, the HST CalSpec spectral energy distribution (SED), `c26202_stiswfcnic_007.fits`, was used as the C26202 spectrophotometric reference spectrum.

The results are shown in 5.

These results are not unexpected, as performing absolute calibrations on reference catalog data is extremely difficult before real observed data are obtained in a new filter bandpass system. Updates are now being applied by the Rubin Calibration Scientist to address these offsets.

Band	No. of ComCam observations	median ComCam mag.	CalSpec synthetic mag.	offset
u	28	17.869	17.573	0.296
g	77	16.684	16.692	−0.008
r	121	16.269	16.362	−0.093
i	99	16.197	16.260	−0.063
z	42	16.589	16.244	0.346
y	24	16.269	16.239	0.031

Table 5: Comparison of ComCam observed magnitudes with synthetic magnitudes calculated from C26202_stiswfcnic_007 using ComCam passbands.

9.3 Galaxy Photometry

Galaxy photometry investigations so far have used the Extended Chandra Deep Field-South (ECDFS) due to the availability of public external reference data, including space-based imaging from the Hubble Space Telescope (HST). Broadly, we have done (or soon will be doing) comparisons to matches against external catalogs and from synthetic source injection (SSI) in coadds. Some preliminary investigations were done with visual inspection of external images.

9.3.1 Comparison to External Catalogs

DM-47234 (`https://rubinobs.atlassian.net/browse/DM-47234`) compared the tract 5063 20241120 DRP object table galaxy photometry with the latest HLF and Dark Energy Camera Legacy Survey DECaLS (DECaLS, `https://www.legacysurvey.org/decamls/`) catalogs.

Fig. 47 shows difference between i-band CModel magnitudes and the HLF HST F775W SourceExtractor magnitudes for both stars and galaxies, using the HST star-galaxy classification. The median difference in both stellar and galaxy photometry is fairly flat across 19<i<25, but also quite large at about 175 mmag for galaxies and 75 mmag for stars. Presuming that the difference in stellar photometry is mainly a calibration issue, the differential between galaxies and stars is still more than a factor of 2 (and still more in quadrature). This could be due to differences in methodology; the HST SourceExtractor-derived magnitudes are more like aperture photometry than a model fit.

Fig. 48 shows the difference between g-band CModel magnitudes and measurements from two Dark Energy Survey (DES) DECam (Dark Energy Camera)-based catalogs. The DECaLS (Dark Energy Camera Legacy Survey) DR10 processing is more recent and includes model photometry, selecting the least complicated model required to provide a good fit from a PSF

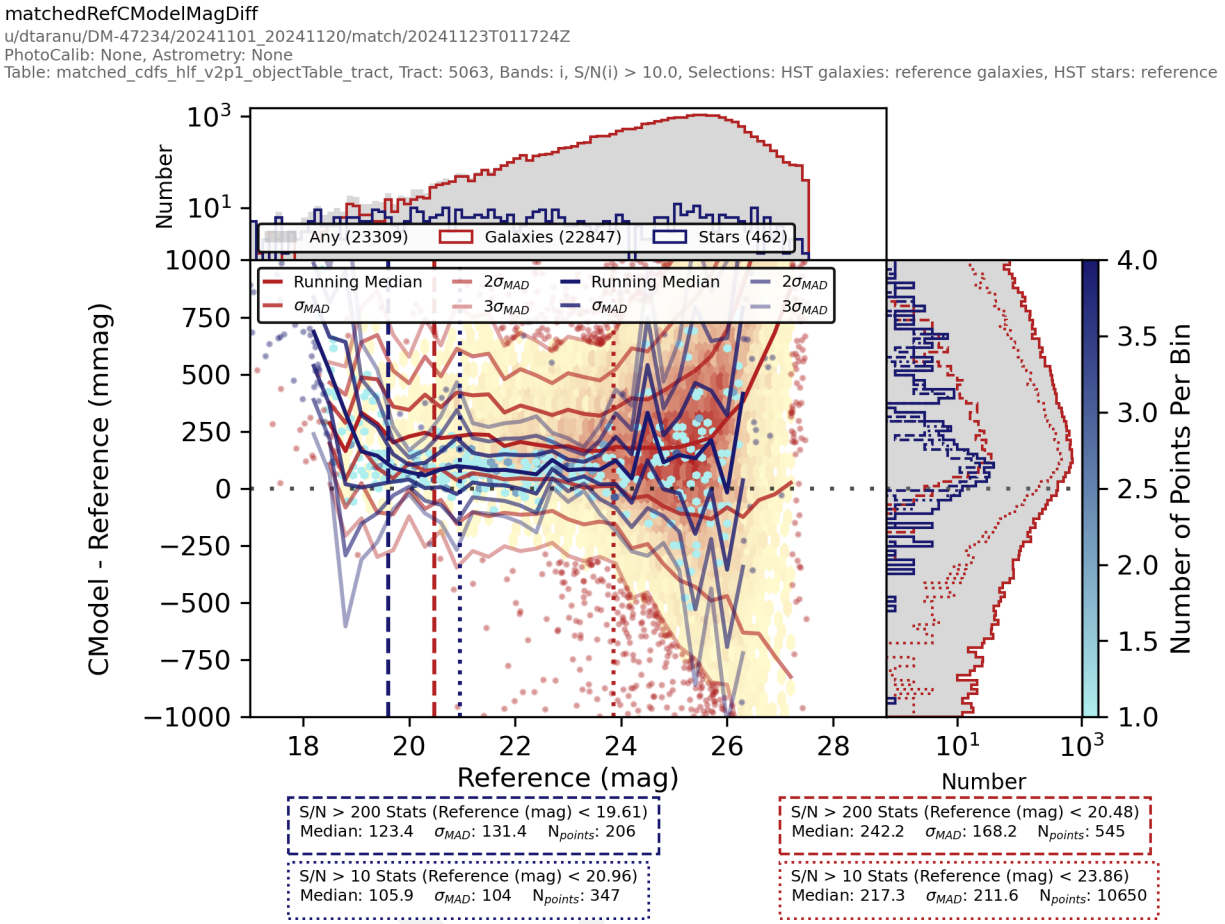

Figure 47: Difference between i-band CModel magnitudes and HST F775W magnitudes in ECDFS.

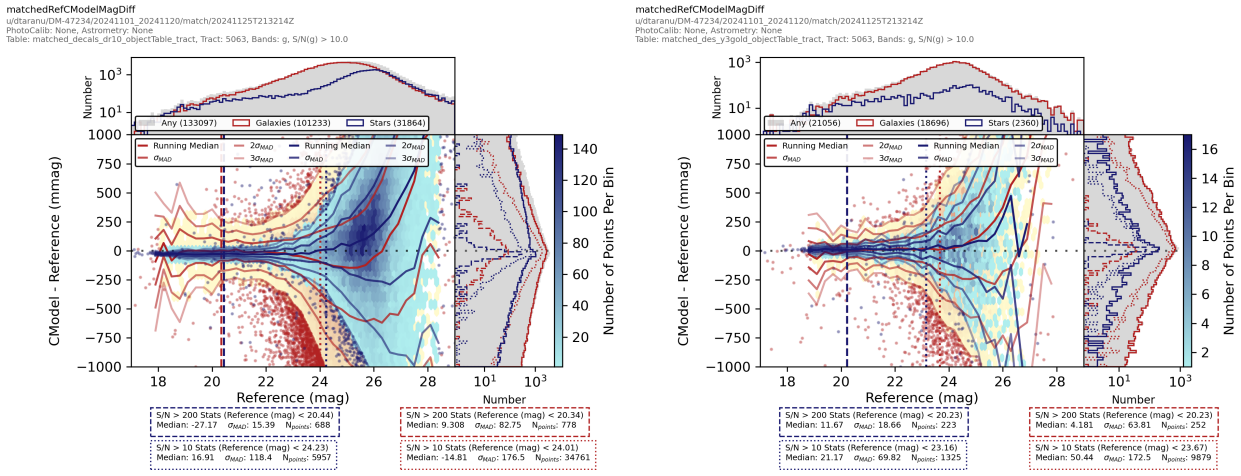

Figure 48: Difference between g-band CModel magnitudes and DECaLS/DES-Y3G catalog values in ECDFS.

to a single free Sersic fit. The Dark Energy Survey Year 3 Gold (DES-Y3G) sample is an older, shallower dataset, albeit using pipelines more similar to the ComCam/DRP pipelines. The median difference between stellar magnitudes is relatively small but varies with magnitude and between the two catalogs. However, given the difference between filters and that no color term corrections have been applied, both the medians offset and scatter of 10 to 30 mmag are acceptable. Bright ($g < 20.3$) galaxies have median offsets smaller than 10 mmag and scatter of 82 and 64 mmag in DECaLS and DES-Y3G, respectively.

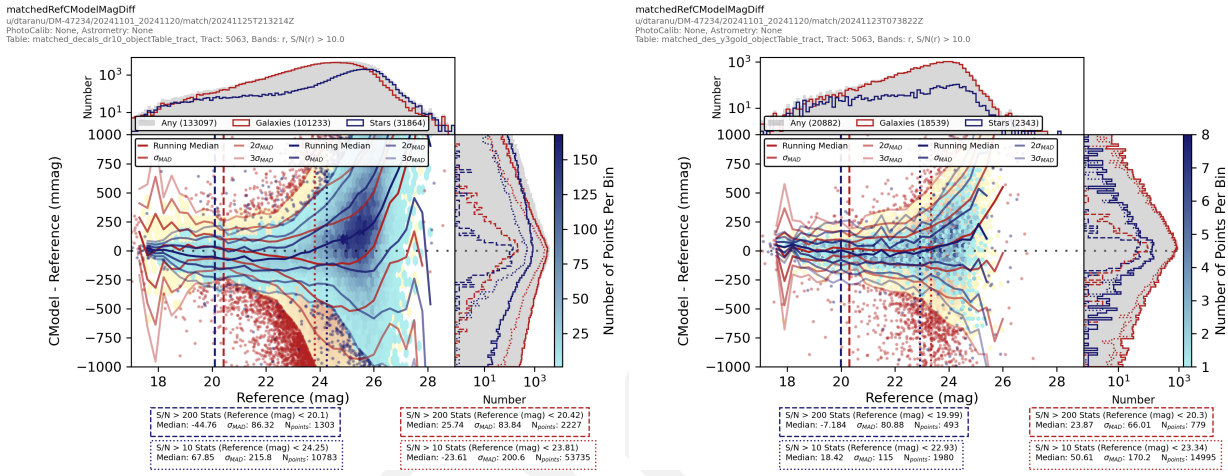

Figure 49: Difference between r-band CModel magnitudes and DECaLS/DES-Y3G catalog values in ECDFS.

Fig. 49 shows r-band magnitude difference plots. Here, the median difference for stars are magnitude-dependent in both catalogs, suggesting that color terms are more important. Similarly, the scatter is much larger, at about 80mmag for $r < 20$. However, the magnitude dependence in the median difference is stronger in DECaLS, both for stars and galaxies. Inspection of the $g - r$ versus $r - i$ stellar locus plot (not shown) reveals that DECaLS photometry has a substantial fraction (about 10%) of outliers, some even a full magnitude off the stellar locus. At any rate, the scatter in galaxy magnitudes is not much larger than that for stars (in fact, it is noticeably smaller in DES-Y3G). Additionally, in DES-Y3G, the median magnitude difference is fairly flat for $19 < r < 23$, so despite the numerous differences in hardware and software, the two catalogs are not inconsistent. The i-band photometry in DECaLS shows qualitatively similar but quantitatively worse pathologies and is omitted for brevity.

The $r - i$ color differences shown in Fig. 50 are similar between all three catalogs. The median differences are very small, albeit different in sign between the two pairs of catalogs. The scatter in star color differences is nearly constant to about 22nd magnitude, whereas for galaxies

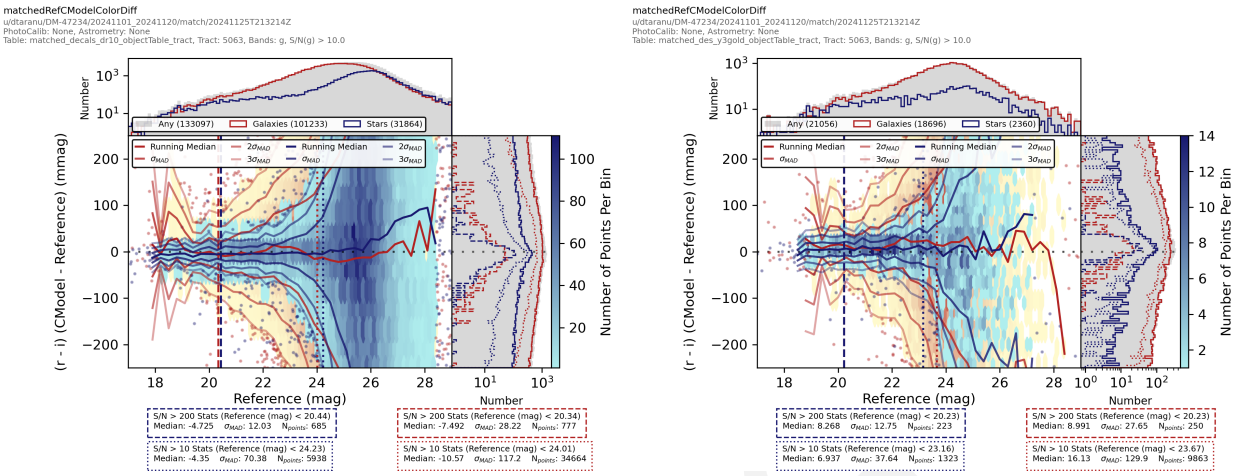

Figure 50: Difference between $r - i$ CModel colors and DECaLS/DES-Y3G catalog values in ECDFS.

it scales with signal-to-noise to a minimum of about 25mmag at 20th mag (photometry for brighter galaxies is limited by model inadequacy and irregular structure). In short, galaxy colors appear quite consistent between all three catalogs, although how the small differences impact derived quantities like photometric redshifts remains to be seen.

9.3.2 Additional Investigations

Analysis of the accuracy of magnitude and color errors await the implementation of synthetic galaxy injection in DM-47185 (`https://rubinobs.atlassian.net/browse/DM-47185`). Some analysis is possible with matching to reference catalogs; however, besides the problems with the DECaLS photometry, we are not yet taking into account reported errors on reference fluxes (which may themselves be underestimated).

Besides single-band/forced CModel photometry, MultiProFit multi-band (gri) single Sersic fits have been run on a single patch in tract 5063 on DM-47526 (`https://rubinobs.atlassian.net/browse/DM-47526`) but have yet to be analyzed. Other algorithms like aperture, GaAP and Kron magnitudes/colors have yet to be compared.

9.3.3 Conclusions

Galaxy photometry in ECDFS appears consistent with at least two different catalogs covering the same field (one space based) and the differences identified in a third (DECaLS) appear to

be peculiar to that catalog, not our own processing. This is not to say that the galaxy photometry is optimal, as hardware and software differences make it difficult to quantify expected differences. Comparisons to external data should be more illuminating once we have coadds in the COSMOS field and can compare to HSC imaging with the same pipeline versions.

10 Low Surface Brightness Sources and Scattered Light

The low-surface-brightness science team has been actively involved in investigating the ComCam imaging. Efforts in this area have largely broken down along two avenues.

10.1 Visual Inspection

Several members of the team have been actively engaged in image inspection with a specific eye on low-surface-brightness features. In addition to the features reported in Sec. 6 several items that have arisen during this inspection which are of especial interest in the context of low surface brightness science:

- **Ghosts:** Ghosting, internal reflections of the light from astronomical objects off of multiple reflecting surfaces within the camera (e.g., the detectors, lenses, and filter), is a well known contaminant for low-surface-brightness science. Ghost patterns were associated to stars both on, and slightly off, the ComCam field-of-view. Qualitatively, the presence and appearance of the ghosts are well predicted by Josh Meyers' `Batoid` ray trace code. The nature of most of the ghosts will be quite different for the full LSSTCam, with the exception of the ghost produced within the filter itself.
- **Sky over-subtraction:** Correct subtraction of the sky background around large, bright astronomical objects (e.g., nearby galaxies, nebulae, galaxy clusters, etc.) while making accurate measurements for faint objects in the frame is a challenging task. The LSB group has been tracking instances of astronomical objects that have been observed by ComCam and are likely to suffer from background subtraction issues.
- **Artificial Satellites:** The low-surface-brightness, out-of-focus tails of bright artificial satellites may contribute structured low-surface-brightness features in stacks and coadds. While the topic of artificial satellites is largely covered in Sec. 11.1, the LSB group is interested in tracking particularly prominent examples.

The group is tracking visually identified instances of many of these features in ComCam imaging.

10.2 Quantitative Ghost Investigation

A more quantitative evaluation between `Batoid` and the ComCam imaging is now being developed to assess the precision and accuracy of the `Batoid` model when it comes to predicting the location, morphology, and intensity of ghosts. Gaia is being used to identify bright stars that should contribute prominent ghosts. These stars are fed into `Batoid` and the output ghost patterns are scaled by the flux of each input star as measured by Gaia. Circular templates for the ghosts are being generated by running `Batoid` on each scattering surface individually and applying Canny edge detection and a circular Hough transform to determine to position and size of each ghost. These circular ghost templates will be compared to the observed data, and eventually fit to the intensity of the observed ghosts to verify/refine the reflectivity coefficients that `Batoid` uses for each camera surface. It is not clear that this analysis will be superior to the corresponding analysis using the CBP. While the ghosting in LSSTCam will be different from that in ComCam, the tools developed for this analysis should be generalizable.

10.3 Future Endeavors

The team hopes to have the chance to collect and investigated on- and off-axis dithered bright star exposures to further quantify ghosting and scattered light. The team is actively investigating metrics to characterize the variance in the sky background modeling. The team is investigating sky background fitting techniques developed on DECam. DECam calibrations have been acquired and testing of these algorithms on DECam data processed with the LSST Science Pipelines is being developed. We hope to apply the quantitative LSB tools being developed on precursor data to the ComCam data.

10.4 Crowded Stellar Fields

10.4.1 Observations taken to date

Linked Figure

Figure 51: An image of the globular cluster 47 Tuc (20241116, 136) taken during AOS testing

Five images were taken of the globular cluster 47 Tuc during early AOS testing (*e.g.* Fig. 51), but while this field is a good target for testing the crowded field pipeline, these observations are out of focus. Deblending failed on these images, and we are waiting on new data under better conditions to test deblending and image differencing.

Other fields observed so far have not exceeded $25\,000$ sources per square degree, which is insufficient for testing the crowded field pipelines.

11 The Variable Sky

11.1 Difference Image Analysis: Transience and Variable Objects

11.1.1 DIA Status

As we have started to obtain repeated science-quality images of some fields, we have begun to build coadded templates as part of the regular weekly cumulative Data Release Processings. These mini-DRPs also include difference image analysis (DIA) of their constituent exposures. Using the DRP-produced templates, we have also obtained near-real-time difference images in Prompt Processing for a few exposures. We have not yet had the opportunity to begin tuning template generation, difference imaging, or Real/Bogus characterization of these data, so the report below provides an initial rough characterization of DIA performance.

11.1.2 ML Reliability and Artifact Rates

We ran a convolutional neural network on 51×51 difference, science, and template cutouts for 912k DIASources identified in the `w_2024_47` data release processing. This processing primarily includes data from extragalactic deep fields. These DiaSources were obtained from 4252 detector-visit images, implying an average of 21 DIASources per detector or about four thousand per equivalent full LSST focal plane. This is somewhat less than the ten thousand DIASources expected per visit and may reflect lower sensitivity due to ongoing image quality refinement and early templates.

The CNN was trained on simulated DC2 images with additional point source injection, so caution is needed when interpreting the values returned by this classifier on ComCam data. Nev-

ertheless, Fig. 52 shows a clear separation in reliability scores and would imply roughly a 3:1 bogus:real ratio if taken at face value. These values will be confirmed with manual inspection. We plan to train a purpose-built classifier on larger samples of labeled ComCam data.

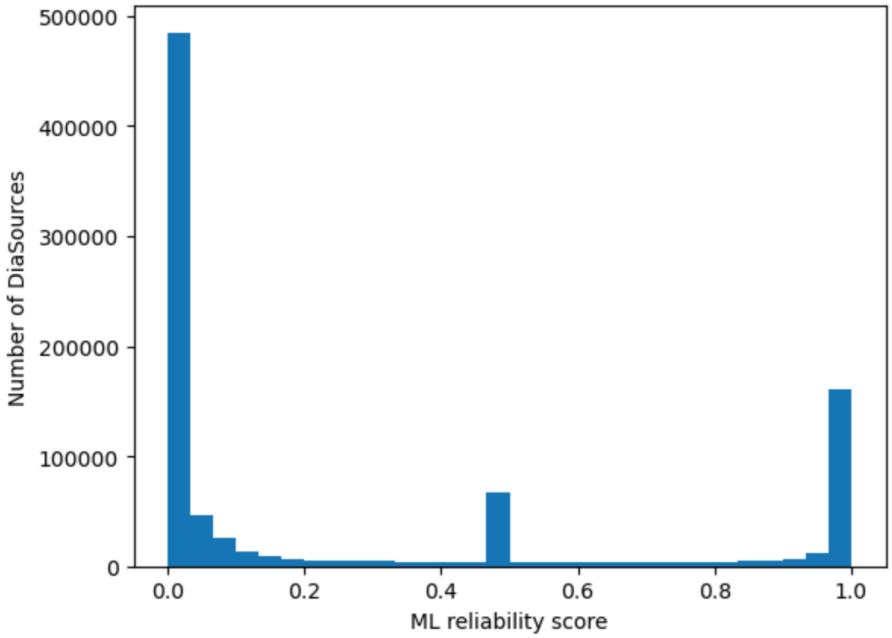

Figure 52: Histogram of machine-learned reliability scores computed on ComCam difference images.

11.2 Difference imaging QA

A difference imaging afterburner is run manually on Prompt Processing output to generate diagnostic plots, such as Fig. 53. From Fig. 53 we see the centroid of the PSF matching kernel sampled across one detector, which reveals a systematic offset between the science and template images. A similar offset is seen across the rest of the detectors for this visit, and in other visits. The images comprising the template used the same astrometric reference catalog as the science image in this case, but the template was constructed with the calibrate+characterizeImage pipeline while the science image was processed with calibrateImage. These are not included in the Prompt Processing payload to save critical time during observing.

The distribution of sources detected on the difference image reveals some detector-level effects that are not fully accounted for. Binning the locations of the diaSources in 1-D in Fig. 54

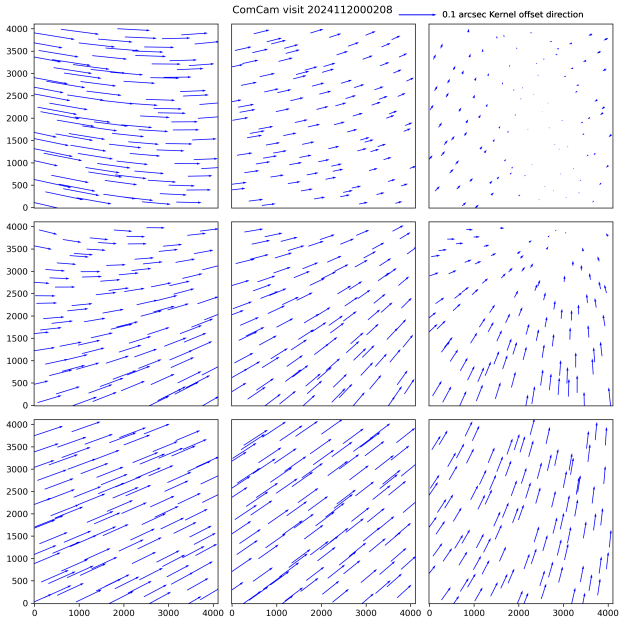

Figure 53: Quiver plot of the implied offset between the science and template images, calculated from the centroid of the PSF matching kernel. Note that the scale differs between the different panels, but that the overall pattern appears coherent over the focal plane, although each CCD was solved independently.

by their x- and y-values reveals systematic overdensities of detections at the amplifier boundaries in x (but not in y). Additional overdensities seen in y-band may be from the residual phosphorescent wax reported to be left on some chips beneath the AR coating.

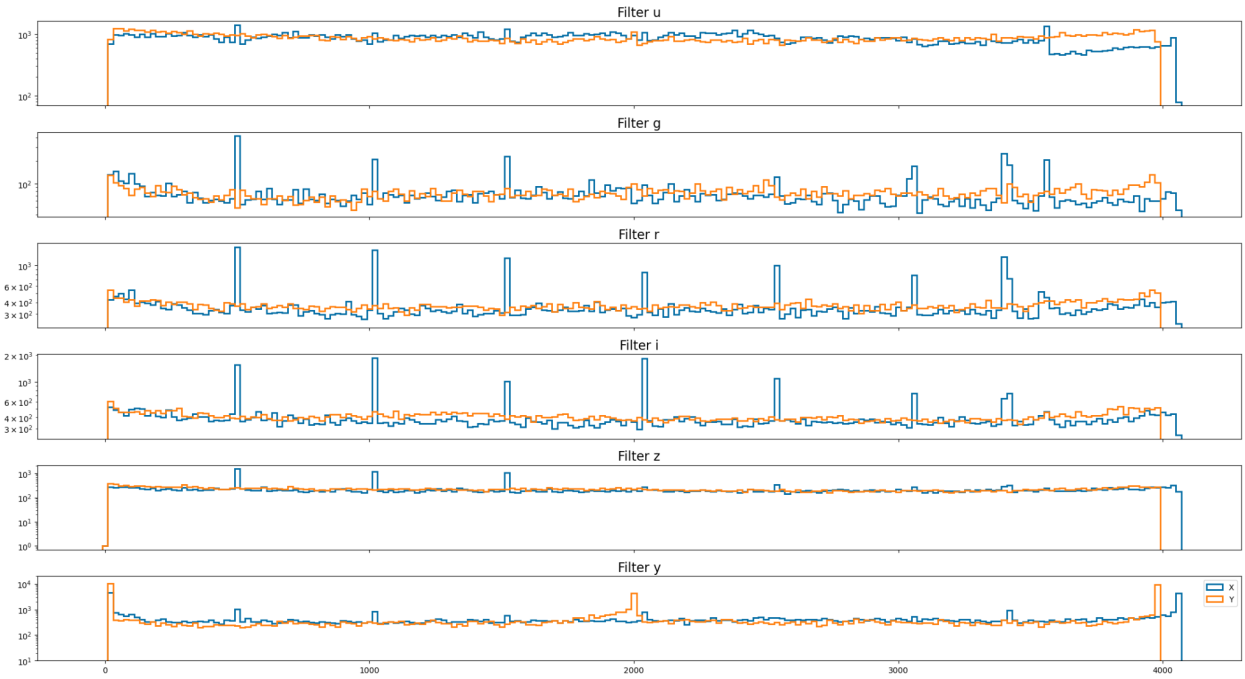

Figure 54: Binning the locations of the diaSources in 1-D by their x- and y-values reveals systematic overdensities of detections at the amplifier boundaries in x (but not in y).

We have analyzed the sources that we detected from the difference imaging campaign. Figure 55 shows the distribution of the diaSources as a function of the magnitude of each source when detected. We have separated the sources into six bands in which the observation was conducted. We show the growth of observed sources in each weekly processing (from week 48 to week 50).

The number of diaSources detected increases as each weekly processing run has more data available. Having said that, the details of the distributions also change. We have verified that this is not due to differences in the algorithm details of different processing runs. This verification was done by observing the data distribution done on different weekly processing runs but taking into account only the data sets already available for weekly-48 runs. In this way, all of the runs have the same underlying data, and the differences are not so stark.

We want to point out two features visible in the plots. First is the steep rise and significant number of diaSources at the bright end of the distribution. We believe this is primarily due

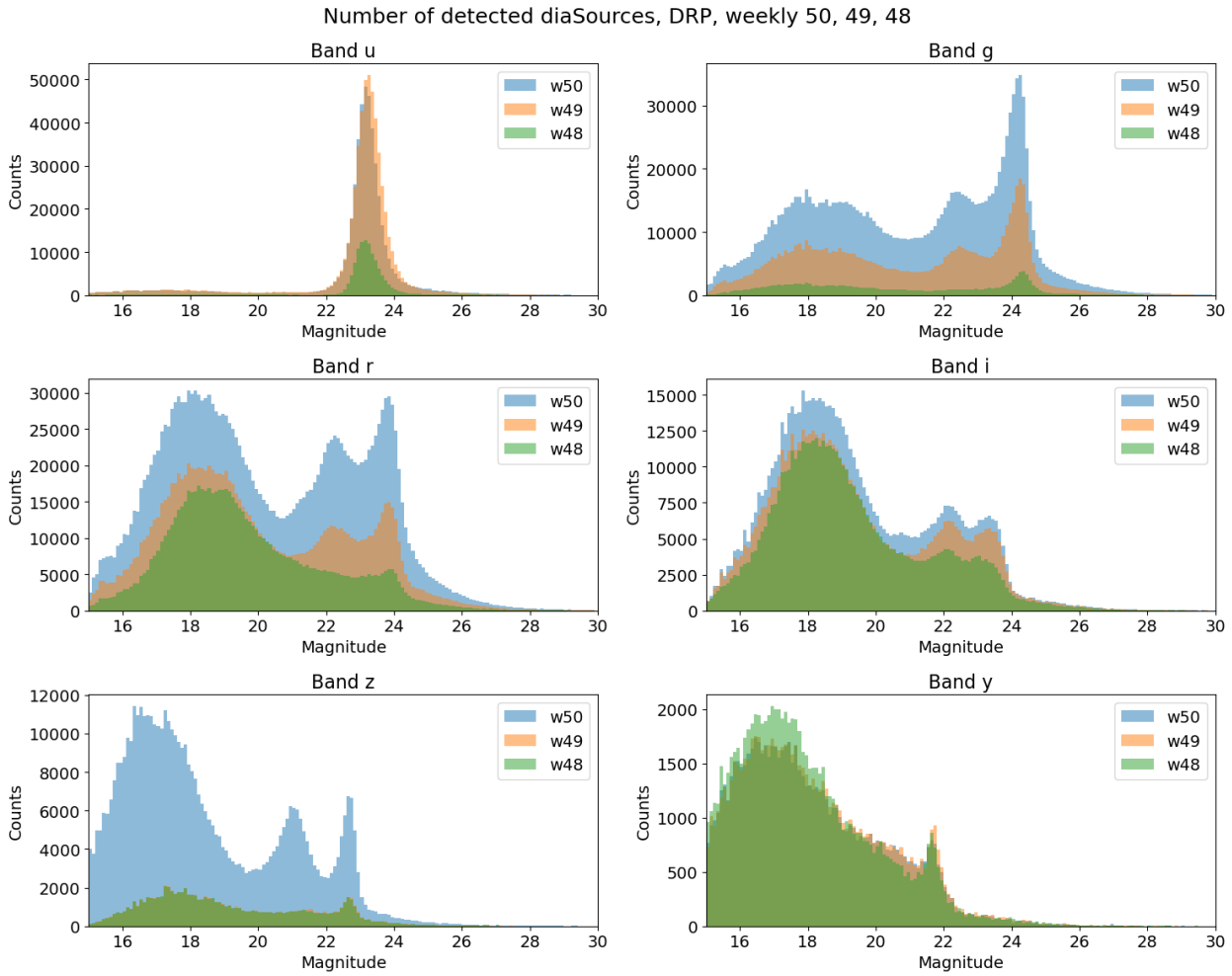

Figure 55: Number of diaSources detected during the campaign, separated in observing bands and weekly processing runs.

to inefficiencies in the subtraction of bright sources; bright point sources on the sky generate diaSources even if they are not variable. See an example of this behavior in the left panel of image here. The increase at the faint end is at least partly due to noise fluctuations being detected as diaSources. See an example of this behavior in the right panel of image here. We are still investigating other features seen in the distribution.

We have also investigated the differences between various fields that were observed. We did this investigation to ensure that the results are not dominated by particularly dense fields, such as 47-Tuc. The results are shown in Figure 56, and show that 47-Tuc is not dominating the results.

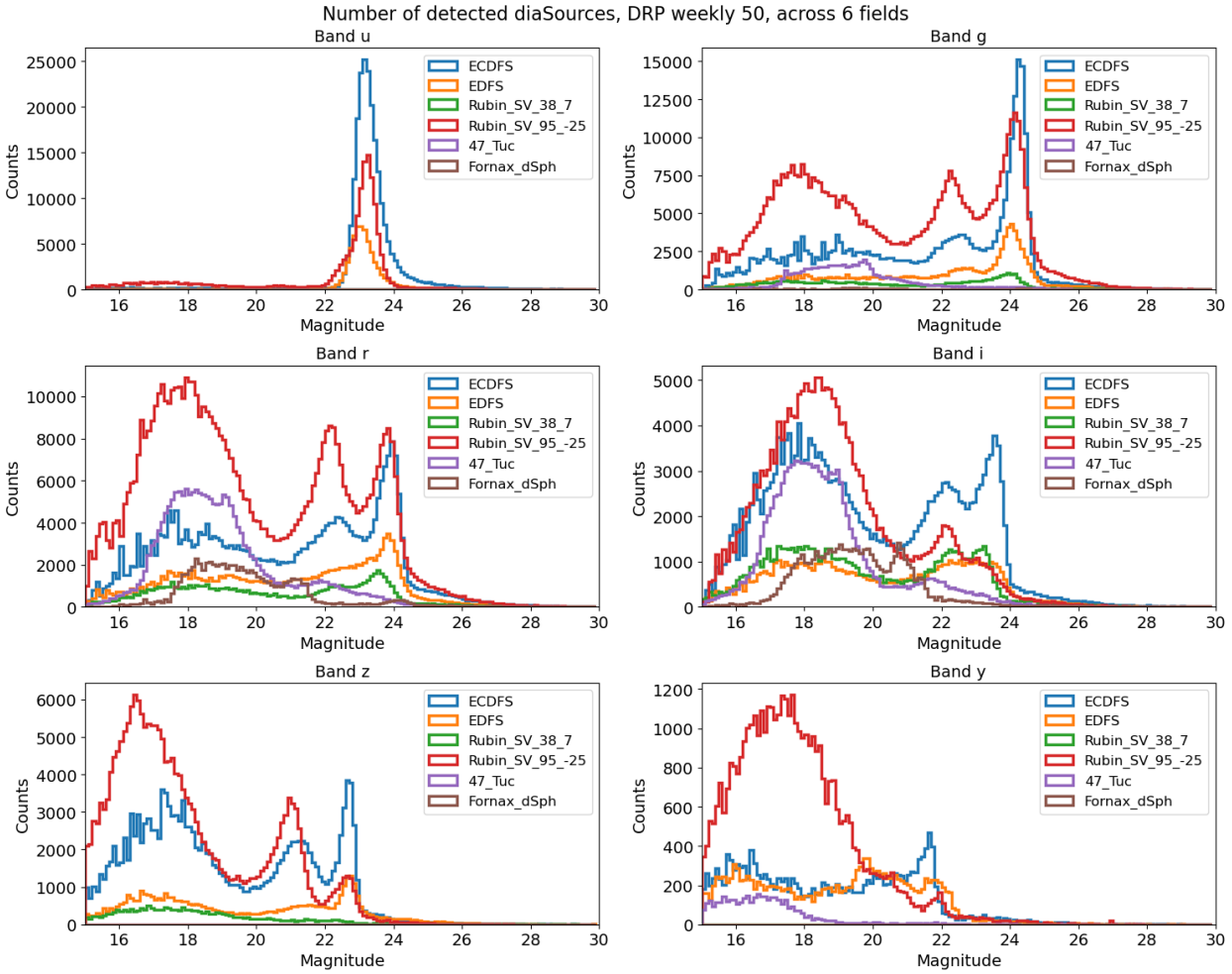

Figure 56: Number of diaSources detected during the campaign, separated across 6 different sky locations that were repeatedly observed.

We have also run the early implementation of the real-bogus classifier (as already discussed

and seen in 52) and present the results in Figure 57. Results are encouraging in the sense that many faint sources are flagged as likely false.

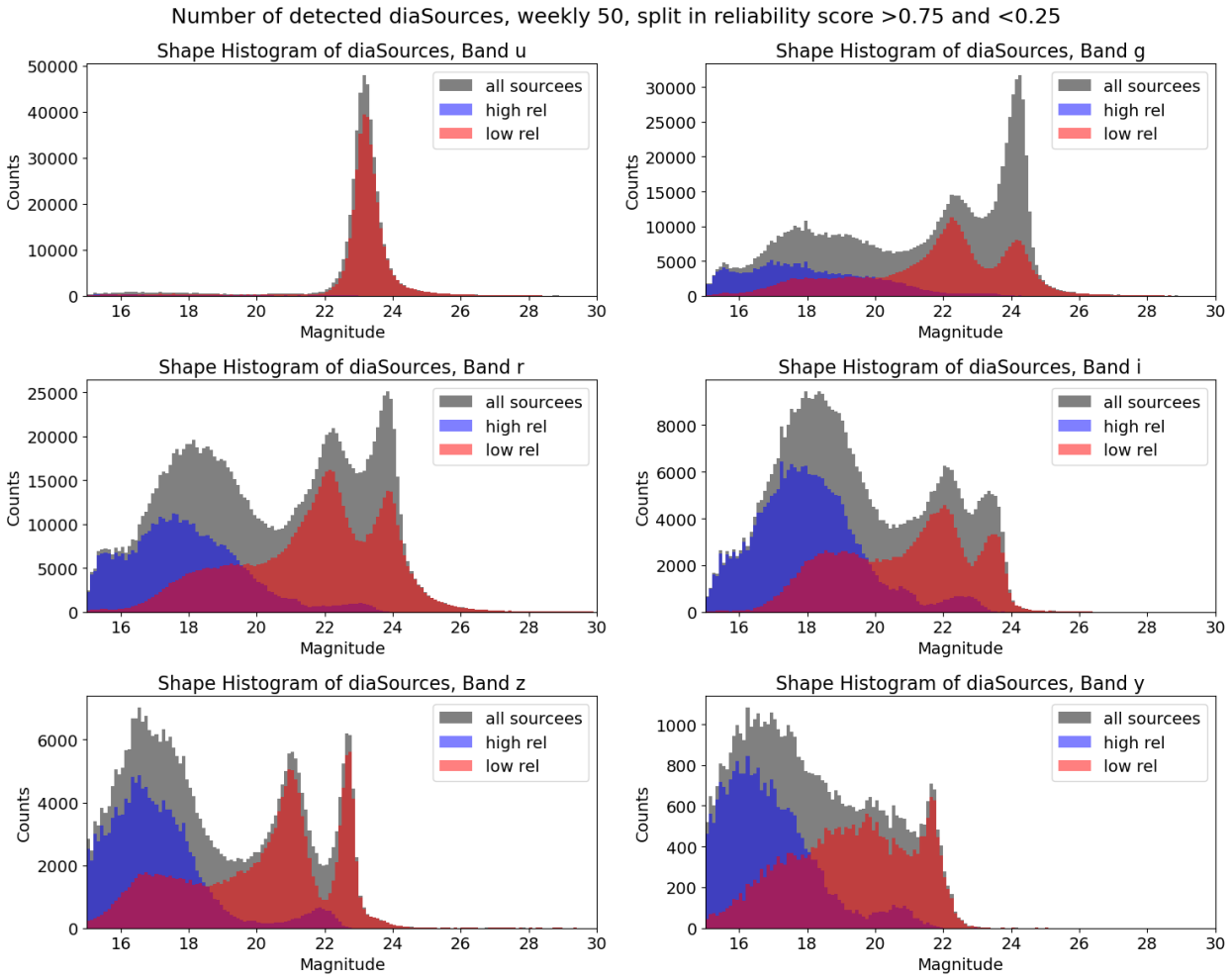

Figure 57: Number of diaSources detected during the campaign, separated in high reliability (determined to likely be real) and low reliability (likely to be bogus) sources.

11.3 Satellite Streaks

As orbital space becomes increasingly crowded, we expect to see many bright streaks, flares, and glints due to satellites and other reflective human-made objects orbiting the Earth, with the majority of the population is in low-Earth orbit (LEO).

As expected, many ComCam detector-visit images clearly show streaks. Visual inspection of nearly all ComCam images to date are being recorded on a best-effort basis in a Confluence

Database dubbed "ComCam Satellite Spotter," and as of 2024 Nov 25 there are over 500 rows.

- Straight bright linear feature, typically at least 20 pixels wide, that crosses one or more detectors and goes off the edge (typical of most LEO satellites, such as Starlink)
- Shorter version of the above, with clear start and/or endpoints, which usually indicates the object imaged is located at a higher-than-LEO orbital altitude (and/or the exposure integration time was unusually short)
- Intermittent linear feature, i.e., a dashed line, due to different parts of the satellite having different reflective properties
- A flare or glint brightening event that fades in and out along a linear trajectory, either isolated or as part of a longer streak
- Actually a bright star diffraction spike
- Actually a cosmic ray that was not repaired
- Variation of any of the above but in out-of-focus donut form (interestingly, depending on altitude, certain streaks may appear either in- or out-of-focus when stars appear as donuts)

Thanks to ComCam's relatively small field of view and the satellite population being as small as it ever will be during Rubin Commissioning and Operations, we have not yet seen an overwhelmingly bright satellite (e.g., BlueWalker 3 or one of the BlueBirds, all operated by AST SpaceMobile). Only a couple instances have streaks bright enough to induce visually-obvious crosstalk "secondary streaks;" the majority of streaks are relatively faint and the only portion of the image impacted are regions overlapping with the streak itself. Reliably determining streak width is an ongoing challenge, as they are wider than the PSF, and some of the brighter streaks have noticeably extended stray light wings.

11.4 Fake Source Injection for DIA

11.4.1 Selection of a data subset

We selected a subset of 24 visits chosen from observations processed by the DRP pipelines that included image subtraction, in order to learn about DIA performance, as well as that of the detection and measurement algorithms.

We chose visits with a zenith distance of less than 45 degrees, as well as some technical parameters, derived from the nominal DRP DIA performance (ratio of PSF between template and science, as well as Kernel basis condition number).

We create a catalog of fakes for these visits by injecting synthetic sources near true sources which are possibly extended, and with a flux within 1.5 magnitudes of the selected source host (Fig. 60)

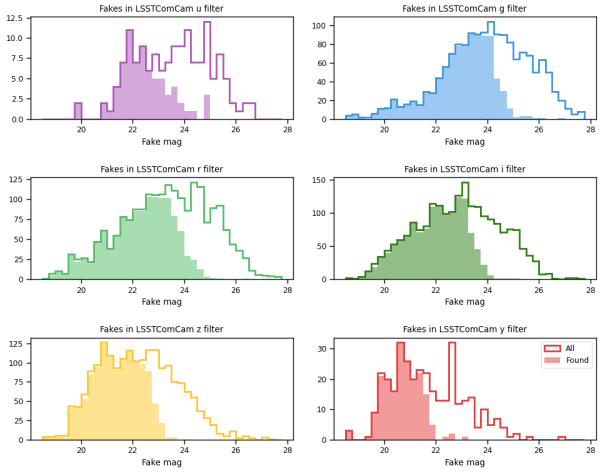

Figure 58: The distribution of magnitudes per bandpass for all the injected fakes (solid lines), and in shaded region the distribution of magnitudes of the fakes detected by the AP pipeline.

We run Alert Production pipeline with a set of additional tasks that handle fake injection on the `initial_pvi` images, and then the book-keeping tasks of fake catalog matching to diaSources as well as forced photometry for SNR estimation. We then cross-matched the position of our candidate detections, or *diaSources* with the positions of the synthetic sources, using a tolerance of $0.5''$ (roughly 2.5px).

Those fakes that found a match are called “found fake” and objects that had no match we refer as “lost” or “missed” fakes. The rate of found to existing fakes is our recovery rate, Recall or Efficiency of detection.

The detection efficiency is plotted in Fig. 59; the astrometric errors in the recovered synthetic sources is shown in Fig. 60, while the photometric errors appear in Fig. 61

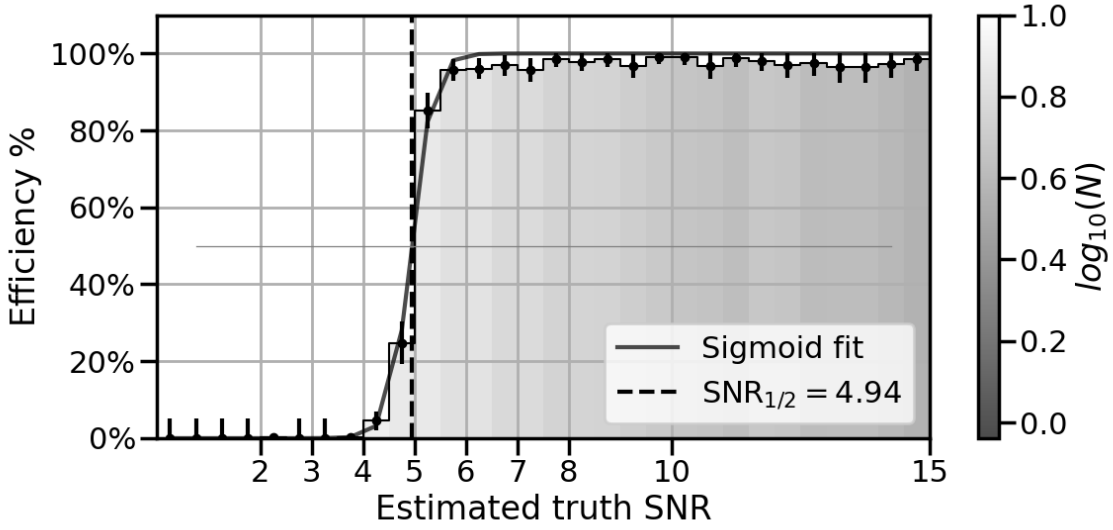

Figure 59: The detection efficiency as function of the PSF estimated S/N ratio of the fake sources. The SNR 1/2 parameter is also included in dashed lines, and represents the 50% efficiency S/N threshold value (lower is better).

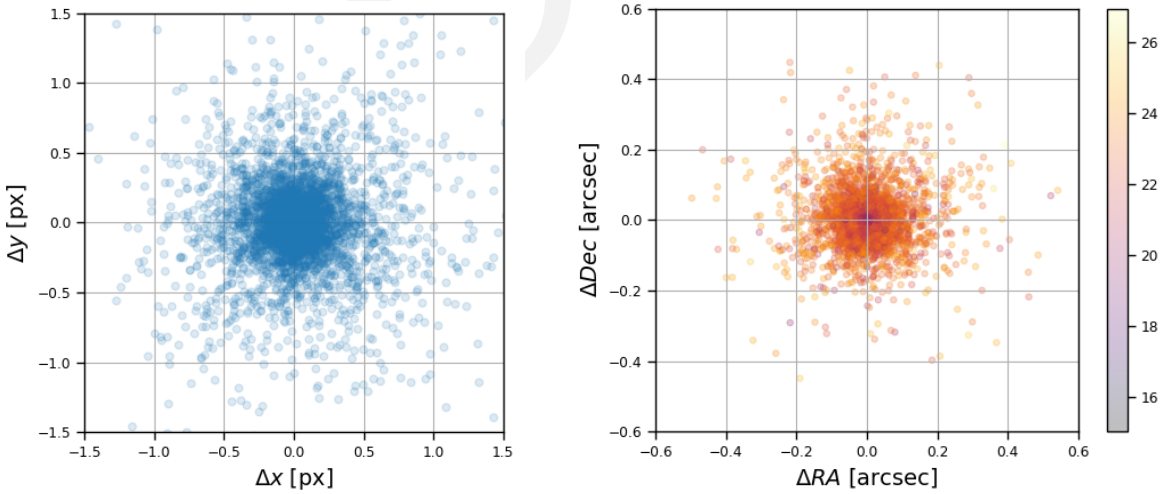

Figure 60: The scatter of the coordinate centroid recovery of the fakes. In the left we have the scatter around the true centroid in pixel coordinates, and in the right the scatter around the true center of fakes in sky coordinates (and in units of arc-seconds), wit the grid matching the pixel grid by means of the platescale. Also, we include the brightness in colormap.

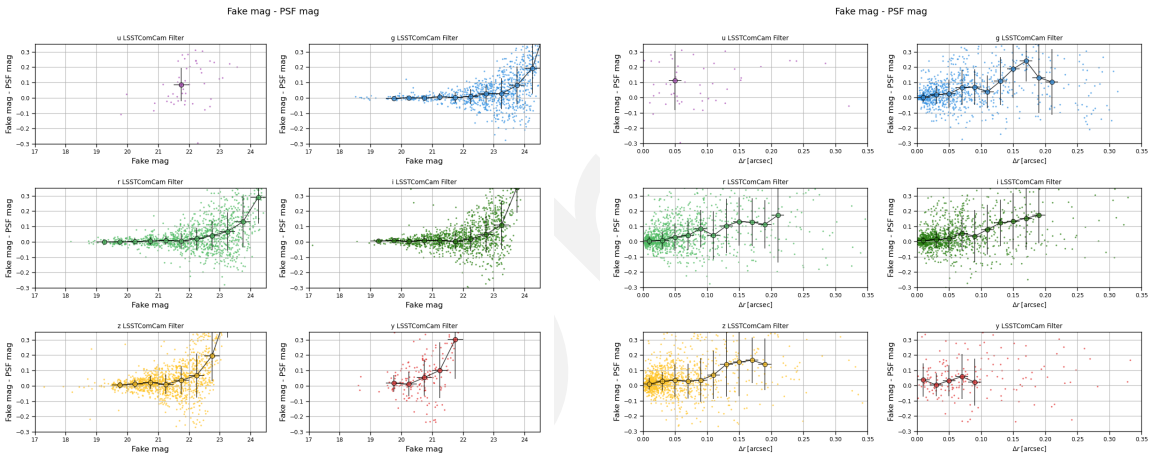

Figure 61: The residual of PSF magnitude measurement for found fakes, as function of their true magnitude (left) or matching distance in arcsec (right).

11.5 Solar System Object Association and Discovery

11.5.1 Known Object Association

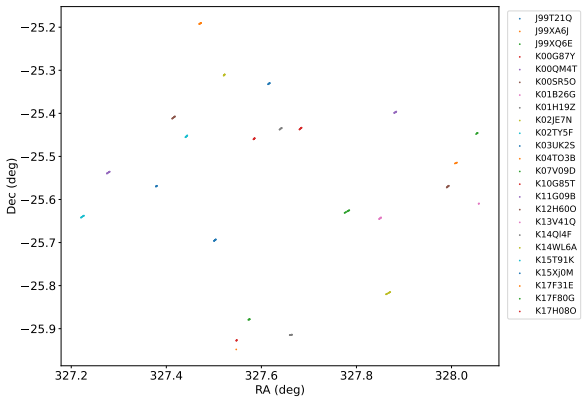

Figure 62: Positions of the 24 asteroids associated in images from 2024-11-06.

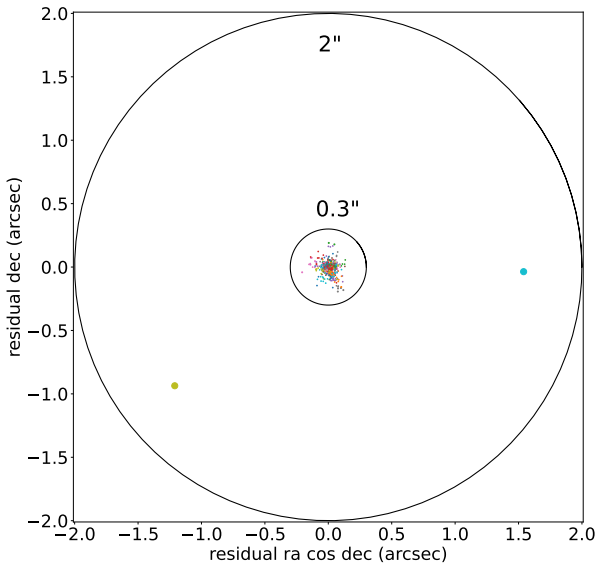

Figure 63: Astrometric residuals of the 633 sources associated to 104 asteroids on 2024-11-23. All but two sources have residuals under 0.3 arcseconds, while the two outliers have been identified by visual inspection as mis-associations of undetected asteroids.

During commissioning we perform asteroid association testing on direct exposures (science visits). In regular operation, once templates are readily available, asteroid association will only be performed on image differences.

Visit image tests: Ten images taken in one field on 2024-11-06 and ten each in four fields on 2024-11-23 were close enough to the ecliptic for possible asteroid association. Across the five fields, we associated 828 sources with known asteroids, including 128 unique objects. The 24 objects associated on 2024-11-06 are shown in Fig. 62. We compared the sources' astrometry to our ephemerides, as shown in Fig. 63. We find very low bias: the median unsigned error is 13 mas, indicating that there are no major errors in either timing or astrometry. We also find low variance, with standard deviationsin RA and Dec of 41 and 44 mas respectively, though in an especially bright and therefore low-variance sample of known objects. Evaluating the precision of asteroid association tests the whole software chain, including the astrometry pipeline, ephemerides computation, and image timing. In sum, the total error contributed by these different systems appears to be low enough for high-confidence association of known asteroids.

Difference image tests: Difference images have so far been made only of two fields very far from the ecliptic, where solar system objects are very rare. Known-object association ran, but (correctly) associated no difference image sources to known objects.

11.5.2 Tracklet construction on Visits

Similar to association, while templates and image differences are not widely available we use single-frame catalogs to test elements of the linking pipelines.

Visit image tests: We attempted to make tracklets in visit source catalogs including the fields in Sec. 11.5.1 relatively near the ecliptic. In contrast to the difference images averaging 430-840 sources per visit (discussed in subsequent sections), visit images contained 11,000-23,000 sources per visit, mostly stars. The first feasible sequence involved ten images taken on November 6. From an average of 16,000 sources per visit, `make_tracklets` found 3,068 tracklets with at least five points. While most of these were unquestionably spurious, nine of them were ten-point tracklets (i.e. detected in *every one* of the ten visits), showed excellent photometric consistency, and relatively low GCR: very likely real asteroids.

We selected the ten-point tracklet with the very lowest GCR (0.046 arcsec) and checked it against known asteroid ephemerides, obtaining a match to the main belt asteroid **(193300) 2000 SO275**, a 20th magnitude object with a very well-constrained orbit. **(193300) 2000 SO275** was the *very first asteroid confirmed to have been detected with the Simonyi Survey Telescope.* We evaluated LSST's astrometric precision by comparing these detections to predicted positions

from JPL. The RMS astrometric offset was found to be 29 milli-arcseconds (mas), with a systematic bias (the median observed-calculated residual) of only 14 mas in RA and 3 mas in Dec. These errors are statistically consistent with zero, as expected. We also probed for timing errors, which would produce a positional offset in the direction of motion. Dividing the along-track component of the astrometric offsets by the measured angular velocity, we found a median time offset of 0.3 seconds — consistent with zero at the 0.5σ level.

All of the other ten-point tracklets were found to correspond to known asteroids, as did 12 additional tracklets with 7–9 points, consistent photometry, and relatively low GCR. In total, 21 real asteroids were found by `make_tracklets` in this single field, demonstrating its ability to discover asteroids in LSST catalogs.

Difference image tests: We tested tracklet creation with `make_tracklets`, the first stage of *unknown* asteroid discovery for LSST, on the two available sets of difference images, though asteroids were unlikely to be found in these regions of the sky. The first field included 10 visits with on average 840 sources per visit, while the second had 12 visits with on average 430 sources. These numbers are encouragingly low, indicating that Rubin difference images are fairly clean. For this test case, we set `make_tracklets` to require a minimum of 5 sources per tracklet, but it produced only 9 total tracklets, all with fewer than 5 detections, inconsistent photometry, and relatively high Great Circle residual (GCR)[6]. Manual examination of image cutouts confirmed that the tracklets were entirely composed of spurious sources.

More interesting is the nature of the spurious sources that made up the tracklets. All were associated with bright stars, including diffraction rays, incompletely subtracted scattered light halos, and subtraction residuals near the PSF core. This is very good news, as all of these types of spurious detections can be eliminated through pre-screening of the source catalogs.

11.5.3 Summary of Solar System Processing Early Performance Tests

At this point, we have tested the association and trackled-building aspects of the Solar System Processing pipelines, focusing on the validation of algorithms, software components, and the initial validation of end-to-end measurement accuracy. All performed according to expectation, given the limited dataset. Importantly, these early tests demonstrate that Rubin already

[6]Defined only for tracklets with more than two points, the GCR is the RMS residual relative to the best-fit trajectory that follows a Great Circle on the sky at constant angular velocity. Real asteroids, unless they are very near the Earth, produce tracklets with very low intrinsic GCR: hence, elevated GCR usually indicates a spurious tracklet.

exceedes the minimum astrometric and timekeeping accuracy for data submitted to the Minor Planet Center (2 arc seconds and 1 second, respectivelly).

Early data suggests that LSST will produce fairly clean difference image source catalogs for the asteroid discovery pipeline and that pre-screening can make them even cleaner. This is important, because simulations indicate the LSST specifications for the minimum discoverable asteroid (six detections, making up three two-point tracklets, within a two-week time span) are on the edge of what is statistically possible without an unacceptable false positive rate. Hence, it is vitally important for the difference image source catalogs to be as clean as possible. There's a lot of work to do, but the early indications have us cautiously optimistic.

We have not yet tested the multi-night tracklet linking; the data have been taken, but the difference image analysis and linking are still being performed as of the deadline for completion of this note. These results will be reported on at a later date.

12 Survey Performance

Understanding and predicting survey performance includes modeling the likely input telemetry, the expected performance of the telescope and observatory, as well as understanding the survey strategy and its interaction with science outcomes. At this point in commissioning, the operations of the observatory are focused on obtaining specific observations, with very different strategies than will be employed during operations. However, we can begin to evaluate how our models may be validated or not by the currently acquired observations. The science observations acquired as part of BLOCK-320 and PP-SURVEY provide the most useful visits for evaluating survey performance.

In this section, information about zeropoints, sky background, and measured image quality (PSF size) is gathered from the ConsDb, where these values are populated by Rapid Anaysis running on the summit. These values are only populated for ACQ or OBJECT images where existing calibration data is available. We also use the bad visit list maintained by DM (the `excluded_visits` repo) to remove on the order of 100 visits which are marked as clearly bad – typically due to trails. This leaves us with 5008 visits from the ComCam commissioning period; 1670 of these are part of BLOCK-320 and 1848 belong to either BLOCK-320 or its precursor PP-SURVEY.

12.1 Predicted throughputs and zeropoints

The throughput curves available in `syseng_throughputs`, the repository that tracks current system engineering summaries of full-focal-plane throughputs, can be used to predict zeropoints for average ITL CCDs. See `https://github.com/lsst-pst/syseng_throughputs/blob/main/notebooks/InterpolateZeropoint.ipynb`, where a simple interpolation function for filter and airmass is defined for the current throughputs (v1.9). Looking at only the science program visits (BLOCK-320 and PP-SURVEY), where images could be expected to be in the best possible focus and obtained under more controlled sky conditions (and where all images have 30 second exposures), we can compare the predicted 30s zeropoints to the reported median visit zeropoints in the ConsDB (the column `visit1_quicklook.zero_point_median`), as shown in Fig. 64. It is worth noting that the u band is a significant outlier in this comparison of predicted versus measured zeropoint; we believe this is the same issue as discussed in Sec. 9.1.3.4, so is the result of either an issue in the synthetically-derived reference catalog generated for zeropoint calibration or a true underestimate of the system performance in u band. We find that the estimated zeropoints are fairly close to the achieved zeropoints, except in u band. The median offsets for the photometric nights (nights with scatter < 0.3 magnitudes; this is all science program nights except 20241126, 20241209 and 20241210) in the science survey visits are: u = -0.26, g = 0.14, r = 0.09, i = 0.10, z = 0.13, y = 0.18.

We applied these offsets as corrections to the zeropoints for all visits, and after also adjusting the measured zeropoints for the exposure time, can then compare 1 second predicted and adjusted zeropoints for all visits, as in Fig. 65. As an example of a non-photometric night, see also the visits from dayObs 20241210 shown in Fig. 66.

12.2 Predicted sky background

Likewise, the survey simulations use a sky background model as part of predicting five sigma visit depths and to choose observation pointings. The outputs available in the ConsDb include a `sky_bg_median` value, which is in counts per pixel. Together with an estimate of the plate scale (0.2”/pixel) and the zeropoint from the hardware-only (removing atmospheric extinction), we can convert this into magnitudes per square arcsecond, to compare to the predicted values from the rubin_scheduler sky brightness model. The results are shown in Fig. 67, using the measured zeropoints with offsets defined above, corrected for atmospheric extinction using coefficients determined from the `syseng_throughputs` curves. The measured values are very

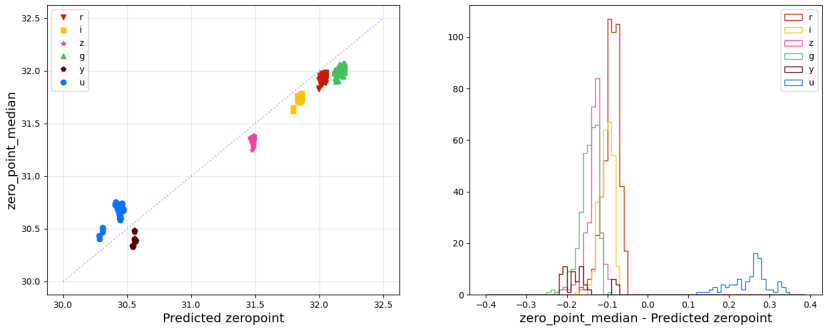

Figure 64: Predicted zeropoints from syseng_throughputs (accounting for airmass) compared to measured zeropoints from `cdb_lsst.comcam.visits1_quicklook`, for BLOCK-320 and PP-SURVEY visits, excluding dayObs 20241126, 20241209 and 20241210. The offsets between predicted and measured zeropoints seen here can be used as a quick approximation for an updated zeropoint and applied to all visits.

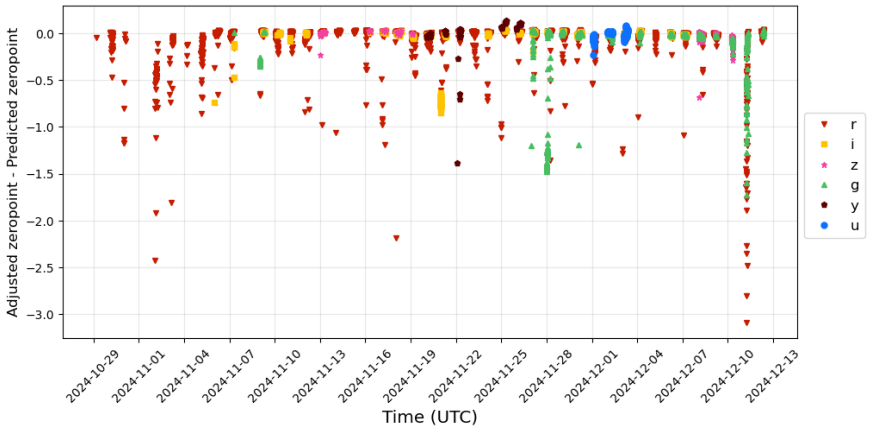

Figure 65: Measured zeropoints from `cdb_lsst.comcam.visits1_quicklook` adjusted for exposure time (`cdb_lsst.comcam.visits1.shut_time`) and our zeropoint offset, minus the predicted 1 second zeropoints from syseng_throughputs (accounting for airmass), for all visits where the zeropoint information was reported. The offsets here are may be indicative of transparency variations, but can also indicate other potential issues such as excessively out of focus images - many of the bad images on DM's list of excluded images were also identifiable as zeropoint outliers.

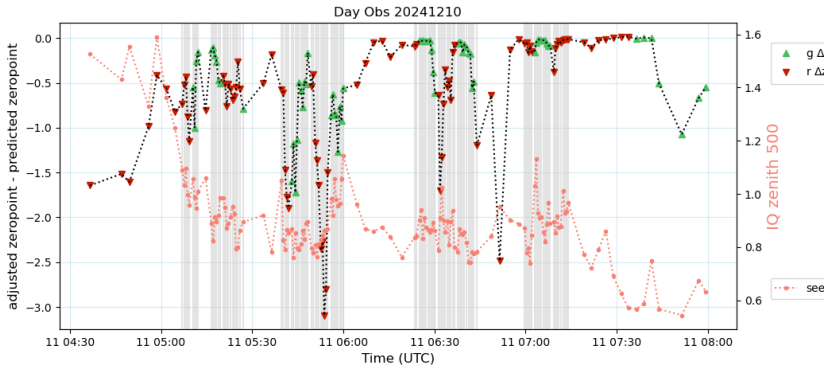

Figure 66: Measured zeropoints from `cdb_lsst.comcam.visits1_quicklook` adjusted for exposure time (`cdb_lsst.comcam.visits1.shut_time`) and our zeropoint offset, minus the predicted 1 second zeropoints from syseng_throughputs (accounting for airmass), for all ACQ and OBJECT visits on dayObs 20241210. The green upward triangles represent g band while the red downward traingles represent r band. The salmon dots indicate an extrapolated atmospheric seeing component, based on the `cdb_lsst.comcam.visits1_quicklook.psf_sigma_median` values adjusted to atmospheric seeing contribution at zenith, 500 nm. The gray lines indicate visits that were part of BLOCK-320.

consistent with the model values for the nights excluding 20241210, with a scatter of less than 0.25 magnitudes in all bands. This is within our expected errors in the sky background model, particularly in y band where the sky is quite variable and harder to model.

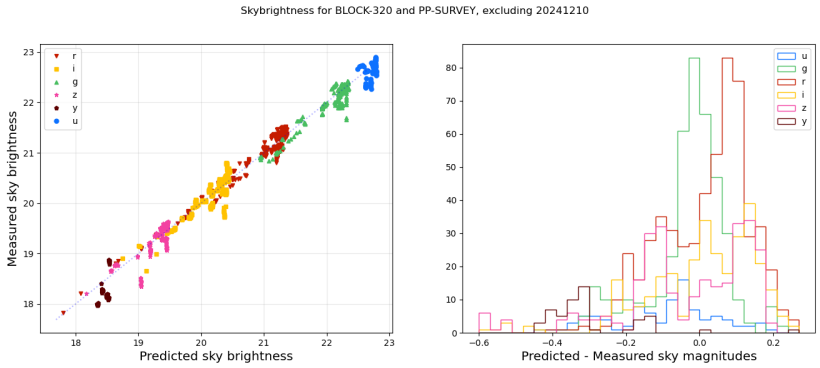

Figure 67: Predicted skybrightness values from `rubin_sim.skybrightness` compared to `sky_bg_median` converted to mags per sq arcsecond using the adjusted zeropoints based on the values in `visits1_quicklook.zero_point_median`.

12.3 Predicted seeing

We look forward to comparing seeing performance to survey predictions as more information is available about the system contribution and atmosphere state via a Rubin DIMM. Initial estimates indicate that the approximate equivalent of seeingFwhmGeom for the science program visits had a mean of around 1 arcsecond, which is very close to average long-term survey expectations, where the mean value is around 0.9 arcseconds. This is particularly impressive for this early phase of commissioning.

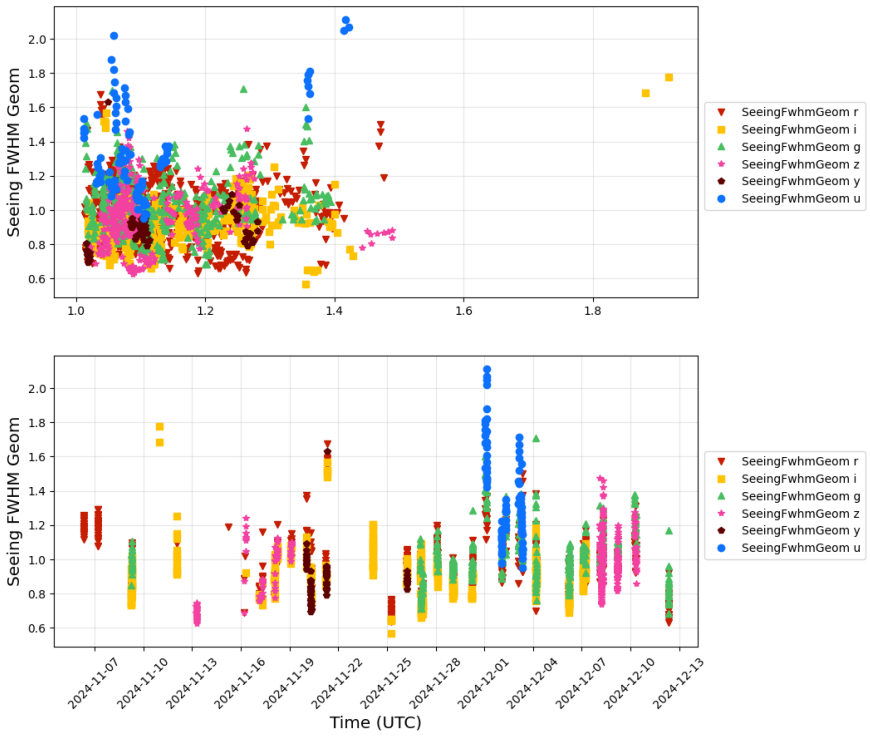

Figure 68: Values of `psf_sigma_median` are converted into `seeingFwhmGeom` as determined from OR4 simulations. The mean `seeingFwhmGeom` in simulations is around 0.9 arcseconds, close to the 1.0 arcsecond mean value in these visits.

12.4 Slew times

As part of the process of commissioning, the movement of the TMA was ramped up from an initial 1% of potential velocity/acceleration/jerk performance, with additional settle times built into various components, to 20% of TMA maximum velocity/acceleration/jerk and greatly reduced settle and wait times. In programs such as the AOS triplets, there are additional movements that must be performed with the telescope, such as moving the focal plane to

adjust focus and applying bending modes to the mirror, so here we look at the visits acquired as part of BLOCK-320. These visits included small dither offsets on the order of 0.2 degrees or so for all fields except Rubin_SV_095_-25 which had a slightly larger dither pattern.

The decrease in time between visits in BLOCK-320 (and corresponding increase in survey efficiency) is shown in Fig. 69. Within each night, the median time between observations is indicated, along with a breakdown of the time spent actively moving the TMA ("TMA slew") and the time spent in settle or waiting for ready reports from various components ("wait before TMA slew" and "wait after TMA slew"). As these are very small slews, the increase in TMA velocity from 1% to 20% did result in an improvement of about 1 second, however this was minor in comparison to the reduction in wait and settle times. Some of the wait after slew can be linked to filter changes, although typically the number of filter changes is few enough to be missed by the median. The bulk of the wait and settles before and after the TMA slew was slowly whittled away over the course of commissioning. In the last few days of comcam observing, the wait time after the shutter closed and before the TMA started moving was reduced to 1 second. The settle time after TMA movement was reduced to zero.

Survey simulations have assumed we would need a 3 second settle after TMA movement. If image quality indicates that this additional settle time is unnecessary, even as the TMA velocities are increased, this could provide a significant bonus to overall survey efficiency by reducing the time between visits from a typical 5 seconds to something potentially as small as 2.5 seconds.

Remaining questions relevant to survey strategy include the efficiency of observations, both sequential observations with standard slew offsets and sustained over many hours and days, and the likelihood of whether a single exposure per visit will be sufficient.

12.5 Synthetic Source Injection

We used synthetic source injection of stars and galaxies to measure catalog completness and reliability. Fig. 70 shows an example figure showing i-band completness and purity as a function of magnitude for ECDFS (tract=5603).

We also confirmed a strategy to use twilight observations to verify the system can accurately observe bright stars (1 mag brighter than 15 saturation lim).

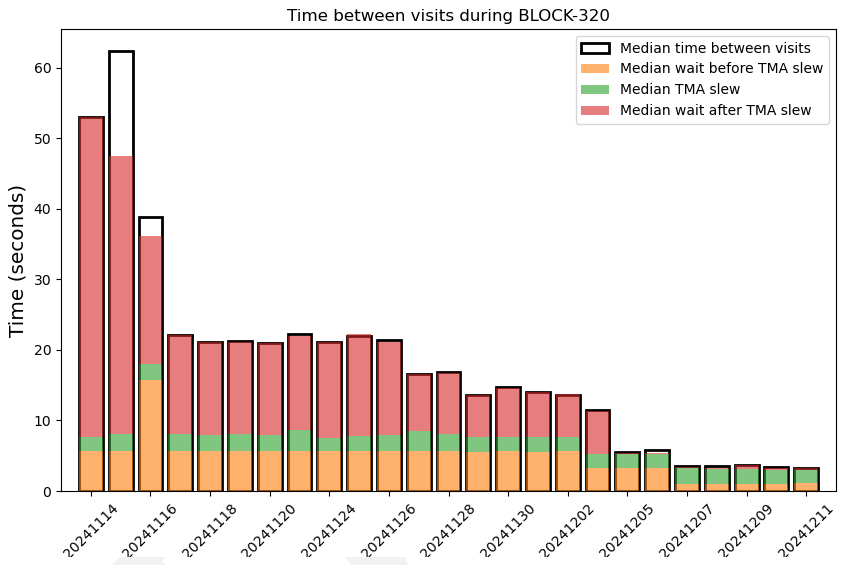

Figure 69: Time between successive visits for Science Pipelines commissioning observations in BLOCK-320. The median time between visits is outlined in black. The median time of active TMA slewing is indicated in green. These active TMA slews are typically sandwiched by a short settle or wait time before moving, and another wait or settle after movement. The wait before slew is indicated in orange, while the wait after the slew is indicated in red. Places where the median of these separate events is less than the total median time between slews generally corresponds to a sequence which contained a fault, usually combined with a number of other slightly longer-than-usual events such as filter changes. The filter changes increase the wait time after TMA movement, but not quite frequently enough to impact the median; the fault increases the total time between visits for a single slew, and this happens to push the median time between visits into one of the slightly longer than typical slews (and perhaps even into one of the filter change slews).

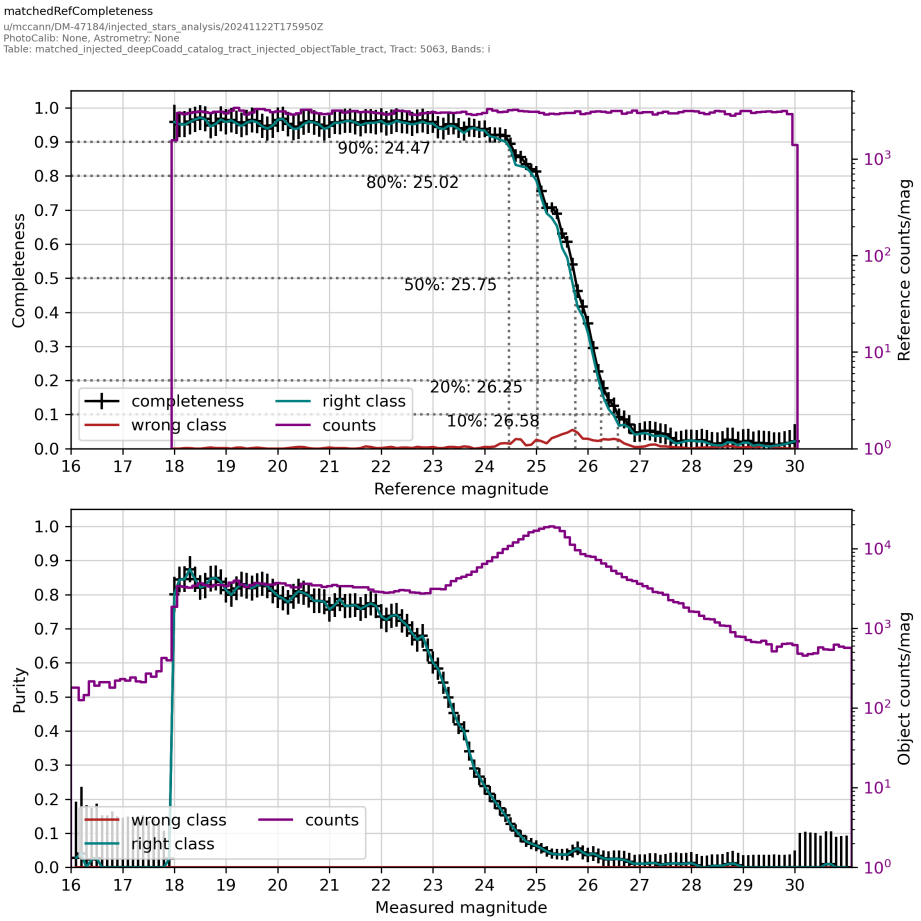

Figure 70: SSI based measurements of completeness and purity in the i-band.

A References

Abbott, T.M.C., Adamów, M., Aguena, M., et al., 2021, ApJS, 255, 20 (arXiv:2101.05765), doi:10.3847/1538-4365/ac00b3, ADS Link

[SITCOMTN-076], Bechtol, K., on behalf of the Rubin Observatory Project Science Team, S.R., 2024, Information Sharing during Commissioning, URL https://sitcomtn-076.lsst.io/, Vera C. Rubin Observatory Commissioning Technical Note SITCOMTN-076

[LSE-29], Claver, C.F., The LSST Systems Engineering Integrated Project Team, 2017, LSST System Requirements (LSR), URL https://ls.st/LSE-29, Vera C. Rubin Observatory LSE-29

[LSE-30], Claver, C.F., The LSST Systems Engineering Integrated Project Team, 2018, Observatory System Specifications (OSS), URL https://ls.st/LSE-30, Vera C. Rubin Observatory LSE-30

[RTN-011], Guy, L.P., Bechtol, K., Bellm, E., et al., 2024, Rubin Observatory Plans for an Early Science Program, URL https://rtn-011.lsst.io/, Vera C. Rubin Observatory Technical Note RTN-011

LSST Dark Energy Science Collaboration (LSST DESC), Abolfathi, B., Alonso, D., et al., 2021, ApJS, 253, 31 (arXiv:2010.05926), doi:10.3847/1538-4365/abd62c, ADS Link

Melchior, P., Sheldon, E., Drlica-Wagner, A., et al., 2016, Astronomy and Computing, 16, 99 (arXiv:1511.03391), doi:10.1016/j.ascom.2016.04.003, ADS Link

B Acronyms

Acronym	Description
2D	Two-dimensional
3D	Three-dimensional
AI	Artificial Intelligence
AOS	Active Optics System
CBP	Collimated Beam Projector

CCD	Charge-Coupled Device
CNN	Convolutional Neural Network
COSMOS	Cosmic Evolution Survey
CTI	Charge Transfer Inefficiency
DC2	Data Challenge 2 (DESC)
DCR	Differential Chromatic Refraction
DECaLS	The Dark Energy Camera Legacy Survey
DECam	Dark Energy Camera
DES	Dark Energy Survey
DESC	Dark Energy Science Collaboration
DIA	Difference Image Analysis
DIMM	Differential Image Motion Monitor
DM	Data Management
DR10	Data Release 10
DR2	Data Release 2
DRP	Data Release Production
ECDFS	Extended Chandra Deep Field-South Survey
EDFS	Euclid Deep Field South
FGCM	Forward Global Calibration Model
FWHM	Full Width at Half-Maximum
G6	Group/Gang of 6 SIT-Com leads
GBDES	Gary Bernstein Dark Energy Survey
GOODS	The Great Observatories Origins Deep Survey
HIPS	Hierarchical Progressive Survey (IVOA standard)
HSC	Hyper Suprime-Cam
HST	Hubble Space Telescope
ICRS	International Celestial Reference Frame
ISR	Instrument Signal Removal
ITL	Imaging Technology Laboratory (UA)
JPL	Jet Propulsion Laboratory (DE ephemerides)
LATISS	LSST Atmospheric Transmission Imager and Slitless Spectrograph
LSB	Low Surface Brightness
LSST	Legacy Survey of Space and Time (formerly Large Synoptic Survey Telescope)

LUT	Look-Up Table
M1M3	Primary Mirror Tertiary Mirror
M2	Secondary Mirror
ML	Machine Learning
MODTRAN	MODerate resolution TRANsmission model
MTAOS	Main Telescope Active Optics System
NGC	New General Catalogue
PSF	Point Spread Function
PTC	Photon Transfer Curve
QA	Quality Assurance
QE	quantum efficiency
RA	Risk Assessment
RMS	Root-Mean-Square
RTN	Rubin Technical Note
SDSS	Sloan Digital Sky Survey
SE	System Engineering
SED	Spectral Energy Distribution
SITCOM	System Integration, Test and Commissioning
SLAC	SLAC National Accelerator Laboratory
SNR	Signal to Noise Ratio
SOAR	Southern Astrophysical Research Telescope
SSI	Synthetic Source Injection
SSP	Solar System Processing
SV	Science Validation
TAXICAB	Telescope and Auxiliary Instrumentation Calibration Acceptance Board
TMA	Telescope Mount Assembly
US	United States
USDF	United States Data Facility
WFD	Wide Fast Deep
ZTF	Zwicky Transient Facility